THE DISCOVERY AND CHARACTERIZATION OF ASTROPHYSICAL TRANSIENTS WITH MEERKAT

Moses Mlangeni

June 2024

Thesis presented for the degree of Master of Science
in the Department of Astronomy.
UNIVERSITY OF CAPE TOWN

Supervisors: Prof Patrick Woudt and Dr Francesco Cavallaro

Abstract

I present the findings of our commensal search for radio transients in the LADUMA field using SARAO Science Data Processor (SDP) UHF-band images, covering ~ 1 year of observations. Employing the Transient Pipeline (TraP), I identified source candidates within the LADUMA field, and applied additional filtering methods to remove false positives. I validated the use of the SDP images for transient search by comparing the SPD images with the independently reduced continuum images of the same of the data set. I conducted a multi-wavelength analysis on the potential sources, assessing radio variability through light curve inspection and radio image post-stamps. Our search spanned DES, Pan-STARRS, MeerLICHT data and the VizieR and SIMBAD database. Eight potential radio transients were selected, showing clear radio variability. The radio variability in seven of the eight sources can be attributed to interstellar scintillation. Notably, SRC213653 exhibits intrinsic variability, displaying high variability at 0.816 GHz with 13 radio detections across 41 epochs, reaching a peak flux of 1.041 ± 0.043 mJy. SRC213653 is associated with the low-mass star LP 888-63, located at a distance of 23 pc from the Sun. LP 888-63 is a M-dwarf companion to a white dwarf binary system, WD 0326-273. Multiwavelength associations of LP 888-63 reveal active flaring behaviour across the electromagnetic spectrum. Optical photometry from TESS indicates a rotational period of 5.7793 ± 0.5067 days. Considering the estimated radius of the star, it suggests LP 888-63 is a slow rotator, consistent with expectations for a typical low-mass star. Archive spectra from European Southern Observatory (ESO ESO-VLT-U2) show Hα emission, indicative of magnetic activity. Through this study I have shown that the SARAO SDP images can be used to detect and characterise radio transients and variables. This opens up the possibility of transient searches in near-to real time.

Acknowledgements

I want to extend sincere gratitude to all individuals and organizations who have contributed to the completion of this thesis. I would like to express my appreciation to the staff and researchers at the University of Cape Town, whose support and guidance have been invaluable throughout this thesis. I am deeply thankful to my supervisors Prof Patrick Woudt and Dr Francesco Cavallaro for their mentorship, expertise, and unwavering encouragement. Their insights and guidance have been instrumental in shaping the direction of this thesis and fostering my growth as researcher. I would also like to acknowledge the contributions of my colleagues and collaborators, Alexander Anderson, Dr Zwido Khangale, Reika Diresete, Dr Ian Heywood, Prof Paul Groot, Sumari Faul, Nathan Peters, Orapeleng Mogawana and the ThunderKAT team at large, who have provided valuable feedback, assistance, and inspiration at various stages of this research endeavor. Furthermore, I extend my gratitude to the National Astrophysics and Space Science Programmer (NASSP) for their financial support, which enabled me to conduct this study and pursue my research goals. Finally, I am grateful to my family and loved ones, Ephraim Matau, Brutus Mogotlo, Nosipho Nene, Thabang Diago, Pholoso Diago, the office colleagues, Leyya Stockenstroom, Simon De Wet and Henco Arlow for their understanding, patience, and encouragement throughout this journey. Their collective support has been instrumental in the successful completion of this thesis, and I am deeply appreciative of their contributions. The journey continues.

Plagiarism Declaration

I, Moses Mlangeni, know the meaning of plagiarism and declare that all of the work in the document, save for that which is properly acknowledged, is my own.

Contents

List of Figures

List of Tables

Chapter 1

Introduction

1.1 Radio Variables and Radio Transients

Radio astronomy looks at space by studying radio waves from stars and galaxies (Tan et al. 2020). Radio emission allows us to understand different physical processes in astrophysical objects, for example stars changing over time and quick bursts of radio waves called transients (Fender & Bell 2011, Fender et al. 2016, Driessen et al. 2022). Telescopes like MeerKAT and the Very Large Array (VLA) are crucial in capturing these fleeting signals (Jonas et al. 2016, Thompson et al. 1980). Their ability to detect and analyze radio waves helps astronomers study these transients and variable phenomena in detail. Furthermore, initiatives like commensal transient searches, where telescopes search for transients while performing other observations, enhance the efficiency of radio astronomy, thus allowing astronomers use telescope time better (Bower et al. 2018).

1.1.1 Radio Variables

Radio variable sources are astronomical objects that exhibit fluctuations in their radio emission over time. These variations can occur on various timescales, ranging from milliseconds to as long as several years, and provide valuable insights into the underlying physical processes that are intrinsic to these sources, or around them. Studying radio variable sources contributes to our understanding of astrophysical events across a wide range of celestial objects. Radio variability can arise from a variety of mechanisms, such as changes in the emission processes, interactions between different components in a system, relativistic effects, and intrinsic instabilities. Such variability can be observed from compact objects like neutron stars and black holes, to extragalactic events like active galactic nuclei (AGN; Xue et al. 2019).

1.1.2 Radio Transients

Radio transients can be classified into two main categories: coherent and incoherent (Pietka et al. 2015b). This categorization is based on the nature of the observed signals. Coherent transients are characterized by their phase coherence, while incoherent transients lack this property. To study both types of transients, high-time resolution observations are required, typically on the scale of milliseconds or even shorter. Such observations allow the detection of rapid changes and variations in the transient signals over time. Additionally, and particular to this thesis, investigations of radio transients extend to the image plane, where observations are conducted with different integration timescales. By varying the integration timescales, images at different levels of sensitivity and resolution can be obtained. This approach provides a comprehensive view of the transients and thus enables the detection and analysis of both short-duration and longer-duration events. By combining high-time resolution observations in the time domain with image plane observations at varying integration timescales, one can gain more understanding into the behaviour, properties, and characteristics of both coherent and incoherent radio transients. The following two subsections focus much more on the two main categories of radio transients. Figure 1.1, reproduced from Hurley-Walker et al. (2022), shows different classes of transients, with their luminosities at different GHz frequencies. Figure 1.1 also shows the division between coherent and incoherent transients, seen by the brightness temperature limit of $T_B \sim 10^{12}$ K with incoherent emissions being below the temperature brightness limit and the coherent being above that brightness temperature limit. The brightness temperature limit is a useful tool for diagnosing emission mechanisms (Burgasser et al. 2005).

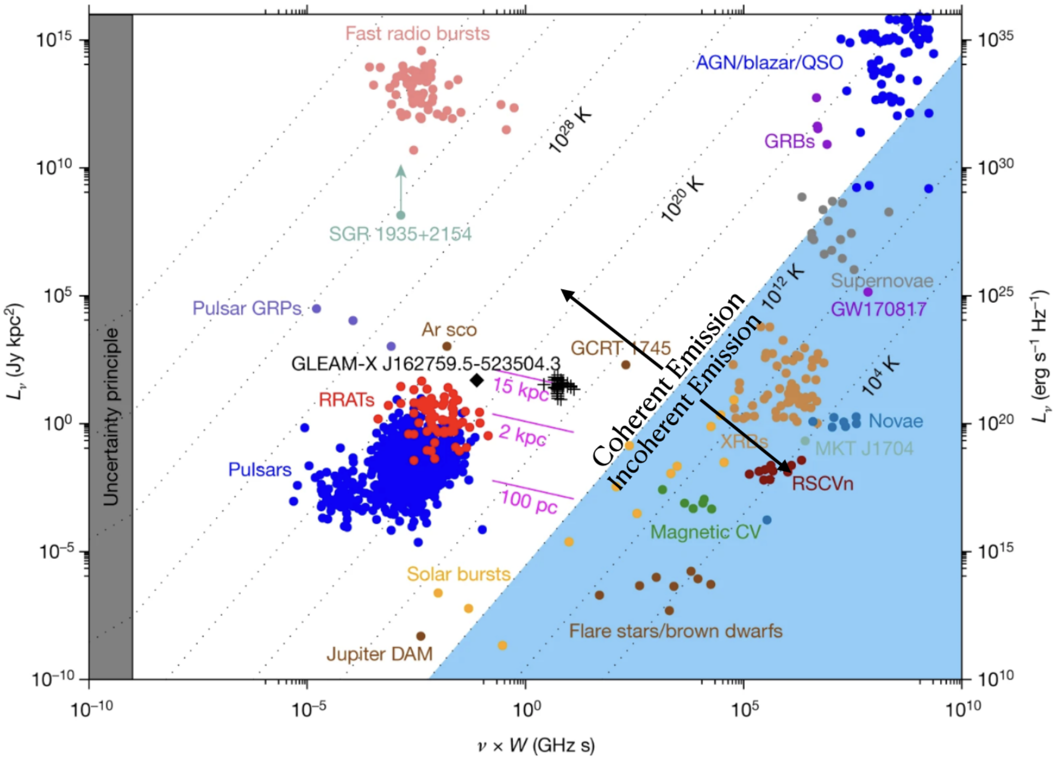

Figure 1.1: This figure shows all known radio transients with their luminosities at their respective GHz frequencies. The figure also shows the two main radio transient categories, where the black dashed diagonal lines shows the temperature brightness of the transients. This figure is reproduced from Pietka et al. (2015a) and Hurley-Walker et al. (2022).

1.1.2.1 Coherent Radio Transients

Coherent radio transients are events that are characterized by sudden and dramatic changes in their radio emission on timescales ranging from microseconds to seconds. There is a high degree of coherence in these transients, this is to say that the emitted radiation has a consistent phase relationship over a wide range of frequencies. The physical processes associated with coherent emission amongst others are electron-cyclotron maser emission (Treumann 2006), pulsar emission mechanisms (Melrose 1992) and coherent synchrotron emission (Bonnarel et al. 2000). Electron-cyclotron maser emission involves the amplification of electromagnetic waves through the interaction with an electron population gyrating around a magnetic field, resulting in the emission of radiation at the electron cyclotron frequency and its harmonics. The coherence of this process arises from the phase correlation of the emitting electrons, leading to a highly structured and organised emission. This mechanism is responsible for various astrophysical radio emissions, for instance, coherent curvature radiation in pulsars, electron cyclotron maser emissions in brown dwarfs, and similar processes in white dwarfs all contribute to their observed radio signals contribute to their respective observed radio signals. This mechanism is also responsible for the radio emission from the Sun (Melrose 1992, Hallinan et al. 2007, Willes et al. 2004, White et al. 2024). Pulsar emission mechanisms: Pulsars are rotating neutron stars that emit beams of radiation due to coherent curvature radiation, plasma instabilities, and other processes in their magnetospheres. The coherence in pulsar emission is related to the collective behavior of particles in the magnetosphere, leading to highly periodic and structured signals. Coherent synchrotron emission is also a key process, where synchrotron radiation, typically incoherent, becomes coherent when emitted by a bunch of electrons with similar energies and phases. This process is particularly relevant in environments like supernova remnants and active galactic nuclei, where dense electron populations can produce highly organised emission.

Known coherent radio transients include fast radio bursts (FRBs), pulsars and magnetars. FRBs are highly energetic, with millisecond-duration bursts of radio waves that usually originate from extragalactic sources (Petroff et al. 2019); pulsars are rapidly rotating neutron stars emitting beams of radio waves, and lastly magnetars are magnetised neutron stars that are associated with intense X-ray bursts and radio emission (Cordes & Chatterjee 2019, Lorimer et al. 2012). These transients all have high brightness temperatures and coherent emission across a range of radio frequencies. The study of such radio transients has benefited greatly from new radio telescopes and recent advancements in data analysis. Instruments such as the Very Large Array (VLA), Canadian Hydrogen Intensity Mapping Experiment (CHIME), the Australian Square Kilometre Array Pathfinder (ASKAP) and the MeerKAT radio telescope, have contributed towards the detection as well as characterisation of FRBs (CHIME/FRB Collaboration et al. 2018, Jankowski et al. 2022). With the aid of the Caltech-NRAO system at the VLA achieving high-time-resolution observations, this will to the understanding of pulsar emission properties (Mooley et al. 2016). Studying the properties of coherent radio transients can help further understand the physics of compact objects, plasma processes, and the interstellar medium. In addition, FRBs offer potential as cosmological probes, allowing measurements of the intergalactic medium and the cosmic web (Cordes et al. 2019, Lorimer et al. 2012, Macquart et al. 2020). Radio telescopes such as the Square Kilometer Array (SKA), with high sensitivity and survey capabilities, offer the potential for new discoveries in the study of coherent radio transients (Braun et al. 2019).

1.1.2.2 Incoherent Radio Transients

Incoherent radio transients are astrophysical events that we best know for their rapid and unpredictable changes in their radio emission. Unlike coherent radio transients, incoherent radio transients do not follow a consistent phase relationship over a wide range of frequencies. Sources that can be incoherent radio transients include flaring AGN, radio bursts that are associated with magnetospheric and atmospheric processes in planets, brown dwarfs and flare stars, radio emission from X-ray binaries tracing relativistic outflows, stellar explosions such as novae and supernovae (Fender & Bell 2011, Fender et al. 2015).

The detection and study of these kind of transients require very sensitive radio telescopes. Instruments such as the VLA, LOFAR and MeerKAT have significantly contributed to the detection and characterisation of incoherent radio transients (van den Eijnden et al. 2020, Starling et al. 2020, van den Eijnden et al. 2022). These telescopes, with their wide frequency coverage and high sensitivity, allow for the identification and study of a diverse range of incoherent events. The physical processes of incoherent radio transients can be understood better with the aid of multi-wavelength and multi-messenger observations. This is to say, the combination of radio observations and other wavelengths such as optical, X-ray and gamma-rays provide a more comprehensive understanding of the astrophysical events associated with these kind of transients (Fender et al. 2016). Incoherent radio transients provide opportunities to study the dynamics of AGN, the explosion mechanisms of supernovae, the magnetic activity of stars, and the atmospheric processes of planets.

The associated radio emission processes includes: Synchroton emission (Longair 2011), Gyrosynchrotron emission (Dulk 1985), Free-Free (Bremsstrahlung) emission (Nindos 2020) and Cyclotron emission (Melrose 1980).

Synchroton emissions, is a significant mechanism driving incoherent radio emissions. This occurs when relativistic charged particles, typically electrons, spiral along magnetic field lines, emitting radiation as they are accelerated. Synchrotron emission produces a characteristic power-law spectrum, with higher energy particles emitting higher frequency radiation. The emitted power per unit frequency $P(\nu)$ follows a power-law distribution:

$$P(\nu) \propto \nu^{-\alpha} \tag{1.1}$$

where α is the spectral index, typically ranging from 0.5 to 1. This spectrum is broad and continuous, with more intense radiation at higher frequencies. The critical frequency ν_c, where the emission is most intense, is given by:

$$\nu_c \approx \frac{3eB\gamma^2}{4\pi m_e c} \tag{1.2}$$

where: e is the electron charge, B is the magnetic field strength, γ is the Lorentz factor $\left(\gamma = \frac{1}{\sqrt{1-(v/c)^2}}\right)$, m_e is the electron mass and c is the speed of light. The resulting radiation is polarised and can cover a wide range of the electromagnetic spectrum, depending on the energy of the electrons and the strength of the magnetic field.

The Gyrosynchrotron emission, as described by Dulk (1985), is a variant of synchrotron emission observed in regions characterised by strong magnetic fields, such as solar flares. In this process, the electrons undergo acceleration and gyrate along magnetic field lines, emitting radiation across a broad spectrum that includes radio frequencies. Gyrosynchrotron emission plays a crucial role in the study of solar activity and magnetic re-connection processes within the solar corona (Dulk 1985). The electrons are still relativistic but experience stronger magnetic forces. The gyrofrequency ω_B of an electron is given by:

$$\omega_B = \frac{eB}{\gamma m_e} \tag{1.3}$$

emission spectrum is broader and more complex than that of synchrotron radiation, as it includes contributions from both high-energy and low-energy electrons. The resulting radiation spans a wide frequency range, including radio, microwave, and sometimes even X-ray bands, depending on the electron energies and magnetic field strengths. The complexity of the spectrum arises from the superposition of radiation from electrons gyrating at different energy levels, leading to a spectrum that does not follow a simple power-law but instead shows peaks and valleys corresponding to different energy contributions.

Cyclotron emission occurs when non-relativistic electrons spiral around magnetic field lines and emit radiation due to their acceleration in the magnetic field. The key difference from synchrotron and gyrosynchrotron emissions is that the electrons are not relativistic, and thus their speeds and the resulting radiation are much lower. The frequency of the emitted radiation corresponds to the electron cyclotron frequency, calculated as

$$\omega_c = \frac{eB}{m_e} \tag{1.4}$$

where e is the electron charge, B is the magnetic field strength, and m_e is the electron mass (Rybicki & Lightman 1986, Melrose 2017).

This emission is typically narrowband, with the radiation concentrated at the cyclotron frequency and its harmonics. The spectrum is not continuous but discrete, with sharp lines corresponding to the specific frequencies at which electrons radiate. Cyclotron emission is commonly observed in environments with magnetic fields, such as near stars or within accretion disks, and is a diagnostic tool for measuring magnetic field strengths in these environments. However, it is typically a form of non-thermal radiation rather than thermal radiation. (Longair 2011). Unlike synchrotron and gyrosynchrotron emissions, which can be broadly spread across the electromagnetic spectrum, cyclotron emission is confined to specific frequencies, leading to a much more predictable and easily identifiable spectral signature.

Key differences between these emissions is summarised below:

- Synchrotron emission is characterised by broad, continuous spectra resulting from relativistic electrons spiralling in moderate magnetic fields, following a power-law distribution.
- Gyrosynchrotron emission also involves relativistic electrons but occurs in stronger magnetic fields, producing a broader and more complex spectrum due to contributions from a wider range of electron energies.
- Cyclotron emission involves non-relativistic electrons in weaker magnetic fields, resulting in a narrowband spectrum concentrated at specific frequencies, directly tied to the magnetic field strength.

For a more comprehensive discussion on these mechanisms, including their applications in astrophysics, refer to (Irwin 2021).

1.2 Radio Emission from Low Mass stars

This subsection on M-dwarf stars is crucial as it sets the stage for the detailed analysis presented in Chapter 4, where their unique properties and their impact on stellar evolution and exoplanet studies are explored in depth.

M dwarfs, often referred to as red dwarfs, constitute a vital class of stars that significantly influence our comprehension of stellar astrophysics (Reid et al. 2002). These are core hydrogen burning stars and are characterized by their remarkably low mass, typically ranging from about 0.07 to 0.6 $M_\odot$ (Rajpurohit et al. 2013). This places them among the smallest stars in the universe and influencing their structural and evolutionary properties. Relative to other stellar types, M dwarfs exhibit lower surface temperatures. Their effective temperatures range from approximately 2500 to 3000 K (Rajpurohit et al. 2013). They stand as the most abundant type of star in the Milky Way and other galaxies, making up an estimate of 70 percent in the stellar population (Henry et al. 2006, Bochanski et al. 2010).

This abundance significantly contributes to the overall stellar mass in the universe, emphasising their wide-spread presence. Since these stars are known to host exoplanets (Trifonov et al. 2018), understanding their eruptive events such corona mass ejections and stellar flares would aid towards understating the habitability of orbiting exoplanets (Crosley & Osten 2018).

It is known that these stars show dynamic activity in their stellar atmospheres, especially for mid- to late-M dwarfs (West et al. 2008). The observed effects on these stars, such as chromospheric and coronal heating, as well as radio flares, are manifestations of complex interactions between magnetic fields and particles within the stellar environment (Bochanski et al. 2007). These interactions lead to the acceleration of particles, resulting in the production of photons across various wavelengths (Bochanski et al. 2007). The presence of hydrogen emission lines in the star's spectra further underscores the influence of magnetic fields (Cram & Mullan 1979). The emission mechanisms behind these events range from incoherent cyclotron and gyrosynchrotron emissions to coherent bursts from plasma- or electron cyclotron maser emission processes, provide valuable insights into the dynamics of the particles and magnetic fields involved (Dulk 1985).

In recent years, serendipitous discoveries have greatly expanded our understanding of magnetically active and flaring stars. Leading work by de Ruiter et al. (2021) and Driessen et al. (2022) has uncovered a wealth of previously unknown flaring stars through comprehensive surveys, highlighting the importance of systematic observations in identifying these elusive phenomena. Additional discovery by Andersson et al. (2022) have yielded serendipitous detection's of magnetically active stars, providing valuable insights into the prevalence and characteristics of flaring events across different stellar populations (Driessen et al. 2024).

1.3 Interstellar Scintillation

Interstellar scintillation (ISS) refers to the dynamic fluctuations observed in electromagnetic radiation as it travels through the interstellar medium (ISM). It is subdivided into two classes: refractive and diffractive scintillation (Rickett 1990). At its core, interstellar scintillation arises from the interaction between radio waves and small-scale electron density irregularities in the ISM (Rickett 1990). These irregularities cause the bending or refraction of radio waves, leading to observable variations in the apparent position and intensity of radio sources, this is known as refractive scintillation. On the other hand diffractive scintillation arises from the interference patterns caused by the diffraction of radio waves around ISM structures, such as density gradients and turbulence (Cordes & Lazio 2002). The combined effects of refractive and diffractive scintillation introduce observable variations in the apparent position and intensity of radio sources across different radio frequencies (Rickett 1990). Generally, refractive scintillation dominates at lower radio frequencies, where the wavelength of the radiation is larger compared to the size of ISM irregularities. In contrast, diffractive scintillation becomes more prominent at higher radio frequencies, where the smaller wavelength allows for finer resolution of ISM structures (Rickett 1990). The interplay between refractive and diffractive scintillation significantly impacts radio variables, including pulsars, AGN, and transient radio sources (Walker 1998). The intrinsic variability exhibited by these sources is influenced by both refractive and diffractive effects, leading to complex modulation patterns observed in radio signals (Hancock et al. 2019). Though both play a role on these radio variables, refractive scintillation is seen to be more prominent on pulsars and AGN variability. For example, the work by Driessen et al. (2022) provides valuable insights into the variability of AGN and the potential influence of refractive scintillation in modulating their observed properties over extended periods in the long-term monitoring using MeerKAT in the field of the X-ray binary GX 339-4.

1.4 Radio Interferometry

Radio interferometry is a powerful technique used in radio astronomy to combine signals from multiple antennas and combine them in a unique radio telescope, such as MeerKAT, with high angular resolution and sensitivity. In this section I provide an overview of what radio interferometry is, how radio interferometry works and the insights gained from its implementation.

The angular resolution θ can be represented mathematically as

$$\theta \sim \frac{\lambda}{D}, \tag{1.5}$$

where λ is the wavelength of the signal in meters and D being the diameter of the telescope. The angular resolution is measured in radians. In astronomy we are interested in a high angular resolution. The reason for this is that high angular resolution allows us to observe fine details and resolve structures in astrophysical objects. We can also further learn more about the physical processes and mechanisms that takes place in these objects (Thompson et al. 2017), particularly when resolving structures at different resolutions (Bright et al. 2020).

Using an interferometer, Equation 1.5 becomes

$$\theta \sim \frac{\lambda}{b}, \tag{1.6}$$

where b is the baseline length. A baseline is the distance between two antennas, we are interested in the maximum baseline, the distance between the two antennas that are the farthest away from each other. So the angular resolution of an interferometer is determined by the maximum baseline length. Longer baselines yield higher angular resolution, allowing for the detection of finer details in observed objects (Mauch et al. 2020a).

Next, we follow Thompson et al. (2017) to explore the mechanisms of radio interferometry, which involves several key steps: signal collection, correlation, calibration, and image reconstruction.

Signal Collection: Radio interferometry begins with an array of radio antennas strategically positioned to form baselines. These baselines determine the spatial resolution of the interferometer, with longer baselines providing higher resolution. Each antenna in the array collects incoming radio waves from celestial sources. Due to the weak nature of these signals, they are amplified using low-noise amplifiers situated near the antennas. The amplified radio waves are then converted into electrical signals via receivers attached to each antenna. These electrical signals are transmitted through cables or optical fibers to a central processing location.

Correlation: At the central processing location, the electrical signals from each antenna are fed into a correlator, a high-speed digital signal processing unit. Before correlation, the signals from different antennas are adjusted for the time delay caused by their separation in space. This time delay, often referred to as the geometric delay (τ_{ij}), between antennas i and j can be calculated as:

$$\tau_{ij} = \frac{\vec{b} \cdot \hat{\mathbf{s}}_{ij}}{c} \tag{1.7}$$

where $\hat{\mathbf{s}}$ is the unit vector pointing from antenna i to antenna j in the direction of the observed source, $\vec{b}$ is the baseline vector as seen in Figure 1.2 (showing a schematic of two antennas) and c is the speed of light.

By applying appropriate time delays to the signals, the correlator ensures that they are properly synchronized before comparison.

The correlator then performs pairwise comparisons of the synchronized signals from different antennas, computing the cross-correlation function, which measures the similarity between signals as a function of time delay and frequency difference. This process effectively combines the signals from various antenna pairs, accounting for their relative positions and orientations, to produce a set of correlated data known as visibilities.

Calibration: The raw visibilities undergo a Fourier transform to convert the data from the spatial frequency domain to the spatial domain, thereby creating an initial image of the sky. However, this initial image requires refinement through calibration to correct for instrumental and environmental effects such as antenna gains, atmospheric attenuation, and electronic noise. Calibration involves comparing the measured visibilities to those expected from a known reference source and applying the necessary corrections. Imaging algorithms, such as the CLEAN algorithm (a type of deconvolution technique), are then applied to the calibrated visibilities to mitigate the effects of incomplete Fourier sampling and data noise, enhancing image quality. The visibilities, $V(u, v, w)$, are complex quantities that represent the Fourier components of the sky's brightness distribution, and they are measured for specific baselines formed by pairs of antennas.

The coherence function, γ, defined by Equation (1.8), provides a measure of the correlation between the signals received by different baselines. This correlation is crucial because it directly impacts the reliability of the visibility data. Coherence is mathematically expressed as:

$$\gamma = \frac{\langle V(u_1, v_1, w_1) V^*(u_2, v_2, w_2) \rangle}{\sqrt{\langle |V(u_1, v_1, w_1)|^2 \rangle \langle |V^*(u_2, v_2, w_2)|^2 \rangle}} \tag{1.8}$$

Here, the visibility function $V(u_i, v_i, w_i)$ is a baseline-based quantity, and the angle brackets indicate averaging over time and frequency. The coherence function thus measures how well the visibilities, and hence the underlying signals, correlate across different baselines. Coherence is not just a theoretical construct but a practical consideration during calibration. High coherence indicates that the calibration has been successful, allowing the interferometer to achieve its full potential in resolving fine details of the sky. As the quality of the visibilities is directly tied to the degree of coherence, maintaining high coherence throughout the observation and calibration process is critical for producing high-fidelity astronomical images.

Image Reconstruction: The final step involves reconstructing the calibrated visibilities into a high-quality image of the sky. Advanced deconvolution techniques are employed to remove artifacts and improve the clarity of the final image. The refined image reveals the detailed distribution of radio emission from celestial sources. Conducting radio interferometry with instruments like the MeerKAT yields invaluable insights into a broad range of astrophysical phenomena, from the structure of galaxies to transient events. This process is governed by the Van Cittert-Zernike (VCZ) theorem, which establishes a direct relationship between the measured visibilities and the sky's brightness distribution. According to the VCZ theorem, the visibility function $V(u, v, w)$ is the Fourier transform of the sky brightness distribution $I(l, m)$. Mathematically, this relationship is expressed as:

$$V(u, v, w) = \iint \frac{I(l, m)}{\sqrt{1 - l^2 - m^2}} e^{-2\pi i(ul+vm+wn)} \, dl \, dm \tag{1.9}$$

where $V(u, v, w)$ is the complex visibility measured by the interferometer at a particular set of baseline coordinates (u, v, w). $I(l, m)$ is the brightness distribution of the source as a function of sky coordinates (l, m). Lastly the remaining parameters u, v, and w the components of the baseline vector (Thompson et al. 2017, Mauch et al. 2020a). To fully grasp this equation, it's essential to understand the coordinate system in which these quantities are defined. The coordinates u, v, and w represent the components of the baseline vector, which is the vector joining two antennas in the interferometer array.

- **Phase Center and Tangential Sky Plane:** The phase center is a reference point in the sky toward which the array is "phased." This means that the signals from all antennas are adjusted (phased) so that the waves from a source at the phase center arrive at the same phase at each antenna. The w axis is aligned with the direction of the phase center. The u and v axes lie in a plane tangential to the celestial sphere at the phase center, with the origin of the coordinate system at the phase center.
- **Baseline Vector:** The baseline vector, with components u, v, and w, represents the relative position of one antenna with respect to another in these coordinates. The components u and v correspond to the projection of the baseline onto the plane tangential to the sky at the phase center. The component w measures the distance of the baseline along the direction toward the phase center.

The VCZ theorem tells us that the visibilities measured at different baselines (u, v, w) correspond to samples of the Fourier transform of the sky's brightness distribution $I(l, m)$, where l and m are direction cosines that describe positions on the sky relative to the phase center. The inverse Fourier transform of the visibilities, therefore, reconstructs the brightness distribution of the sky. However, this reconstruction is not perfect due to the limited coverage of the u-v plane, where the visibilities are sampled. The incomplete sampling of the u-v plane by an interferometer introduces artifacts in the reconstructed image, known as the point spread function (PSF). The PSF is essentially the response of the interferometer to a point source. It reflects the "beam" pattern of the array, which is determined by the arrangement of the antennas and the sampling pattern in the u-v plane.

In the reconstructed image, the true sky brightness distribution is convolved with the PSF, which means that each point in the sky is spread out according to the PSF. This convolution can cause distortions in the image, such as sidelobes, which are spurious signals that appear around bright sources. To mitigate these effects, advanced deconvolution techniques, such as the CLEAN algorithm, are employed during image reconstruction. These techniques iteratively subtract the PSF from the image, enhancing the clarity and accuracy of the final image. By understanding the coordinate frames and the VCZ theorem, and by applying appropriate calibration and deconvolution techniques, astronomers can reconstruct highly detailed images of the radio sky. This process enables the study of various astrophysical phenomena with unprecedented precision, advancing our understanding of the universe.

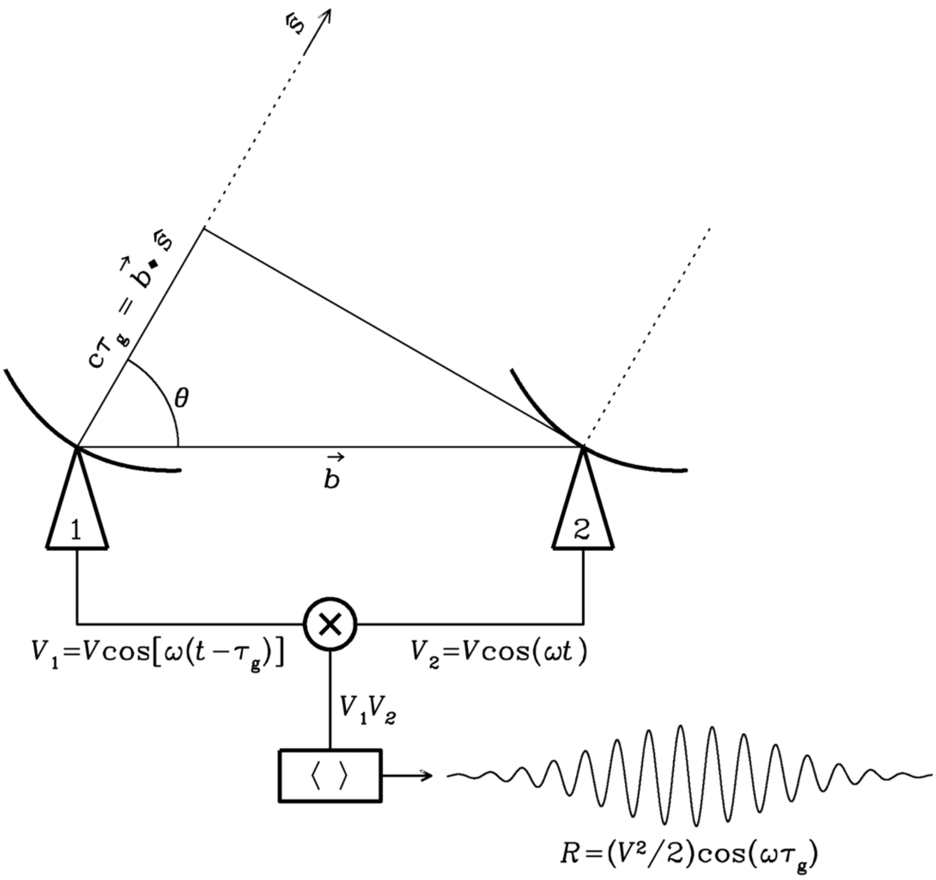

Figure 1.2: This diagram shows two antennas aligned in the same direction, receiving a signal from a point source within a narrow frequency band $v = \frac{\omega}{2\pi}$. $\tau_g = \vec{b} \cdot \hat{\mathbf{s}}$ represents the time delay between antenna 1 and antenna 2, where c is the speed of light. V_1 and V_2 denote the signals received by each antenna, respectively. Adapted from (Condon & Ransom 2016).

1.5 MeerKAT

MeerKAT is a world-class radio telescope located in the arid landscape of Carnarvon in the Northern Cape, South Africa. The telescope was built as a precursor for the mid-frequency component of the Square Kilometer Array (SKA-Mid), and will eventually be integrated into SKA (Swart et al. 2020). Initially known as the Karoo Array Telescope (KAT), its name was changed to MeerKAT when the South African government allocated additional funds for the construction of more receivers, reflecting the project's growth and ambition [1]. The telescope consists of 64 interlinked radio antennas that work together as a single, unified array.

Each antenna boasts a substantial 13.5-meter diameter dish (Camilo et al. 2018; Mauch et al. 2020b). The MeerKAT array spans a wide range of baselines, with the longest extending up to approximately 8 kilometers and a minimum baseline of 29 meters. The core of the array comprises 48 antennas within a 1-kilometer diameter, strategically arranged to enhance sensitivity for pulsar searches and to detect diffuse, large-scale structures in imaging. The remaining 16 antennas are positioned to the full baseline and improve overall imaging capabilities. All the antennas in the array are parabolic in shape and equipped with a Gregorian offset subreflector as seen in Figure 1.3. This subreflector is fixed near the receivers, enabling the antenna aperture to be fully utilized and ensuring the array's

---

[1] SARAO, MeerKAT Radio Telescope, 2021, accessed July 11, 2023, `https://www.sarao.ac.za/science/meerkat/about-meerkat/`

operational effectiveness. The design of this system is specifically optimized to reduce and redirect ground radiation, resulting in a low system temperature of around 20 Kelvin (Mauch et al. 2020b).

The MeerKAT system includes UHF-band, L-band and S-band receivers that span a frequency bands from 580 MHz to 3500 MHz. The UHF band covers the frequency range from 580 MHz to 1015 MHz, the L-band extends from 900 MHz to 1670 MHz and the S-band from 1750 MHz to 3500 MHz MeerKAT observations are primarily conducted in the L-band, which is centred at a frequency of 1284 MHz. These observations involve full polarization and typically employ a binning time of 8 seconds for the target throughout the duration of the observation. However, adjustments to the binning time can be made, with options for 4 seconds or 2 seconds, albeit at the cost of increased storage requirements (Mauch et al. 2020b, Healy et al. 2021).

Figure 1.3: The MeerKAT Radio Telescope: A visual representation of the MeerKAT radio telescope, one of the most powerful instrument for radio astronomy. Image Source: SARAO, `https://www.sarao.ac.za/gallery/meerkat/`

MeerKAT is renowned for its wide-field imaging capabilities, offering an expansive field of view of approximately 1 square degree at a frequency of 1.4 GHz, combined with high resolution and an optimal recovery of the large angular scale flux. This exceptional feature enables comprehensive coverage of the observed sky, making it an invaluable tool for astronomers exploring transient and variable celestial objects (Healy et al. 2021, Mauch et al. 2020b). Adding to its technical specifications, MeerKAT is instrumental in a wide range of scientific endeavors, including the study of pulsars, galaxies, and the cosmic microwave background. Some of the key properties of the MeerKAT telescope are summarised in Table 1.1.

1.5.1 ThunderKAT

ThunderKAT was an observational programme designed to study transient events within the image plane, utilising the capabilities of the MeerKAT radio telescope (Fender et al. 2016). This programme also served as the overarching project behind the MeerLICHT optical telescope, facilitating simultaneous optical observations during night-time MeerKAT sessions (Fender et al. 2016). While its original aim focused on targeted observations of X-ray binaries,

Property	Value
Number of Antennas	64
Antenna Diameter	13.5 metres
Total Collecting Area	13,000 square metres
Frequency Range (UHF)	580 - 1015 MHz [544 to 1088 MHz digitised]
Frequency Range (L-band)	900 - 1670 MHz [856 to 1712 MHz digitised]
Frequency Ranges (S-band)	S0: 1750 - 2625 MHz
	S1: 1968 - 2843 MHz
	S2: 2187 - 3062 MHz
	S3: 2406 - 3281 MHz
	S4: 2625 - 3500 MHz
Resolution	1 arcsecond at 1.4 GHz
Field-of-View	1 square degree at 1.4 GHz
Minimum Baseline	29 metres
Maximum Baseline	7700 metres
Array Phase Centre	30° 42' 39.8" South, 21° 26' 38.0" East, 1086.6 metres Elevation
Sensitivity	7 μJy/beam (in 8 hours, at 1.4 GHz)
Survey Speed	400 square degrees per hour (at 1.4 GHz)

Table 1.1: Technical specifications of the MeerKAT telescope, highlighting key properties relevant to its observational capabilities.

Cataclysmic variables, Gamma-ray bursts, and Type Ia supernovae, alongside wide-scale transient searches across a range of timescales, the project's actual contributions have far exceeded these initial goals.

ThunderKAT's transient searches, conducted from seconds to years, have successfully been executed in near real-time, often running alongside beam-formed transient searches by other MeerKAT large survey projects like TRAPUM and MeerTRAP (Jonas et al. 2016). A key achievement of ThunderKAT is its extensive "piggybacking" on other Large Survey Projects (LSPs), spanning various fields from wide to deep, allowing it to undertake one of the most comprehensive image-plane radio searches for transients. This approach has not only benefited core areas, such as supernovae (SNe), but has also provided a holistic view of radio sky variability across all timescales and flux levels, including the exploration of (inter)galactic HI absorption features in lower-frequency observations.

In its actual execution, ThunderKAT has contributed significantly to the study of transient populations in deep fields associated with other MeerKAT LSPs, such as LADUMA, MHONGOOSE, and Fornax (Blyth et al. 2016, de Blok et al. 2016, Serra et al. 2016). These contributions have deepened our understanding of radio transients, particularly through the determination of the flux and spectrum of gamma-ray bursts (GRBs) and supernovae (SNe) in the MeerKAT radio bands. The work by Driessen et al. (2022), for example, identified 21 new long-term variables within the field of GX 339-4, demonstrating the project's commitment to long-term observations and the detection of variable sources.

ThunderKAT's pioneering role in citizen science was marked by the publication of Andersson et al. (2023), which introduced MeerKAT's first citizen science project dedicated to commensal radio transients. This innovative approach has engaged the broader community in exploring the radio sky, further enhancing the project's scientific impact. Additionally, ThunderKAT's commitment to serendipitous discoveries is exemplified by the findings in Andersson et al. (2022), which reported the serendipitous discovery of radio flaring behaviour from a nearby M dwarf star with MeerKAT and Caleb et al. (2022) which reported the discovery of a radio emitting neutron star with MeerKAT. These unexpected findings underscore ThunderKAT's unique ability to uncover previously unknown radio transient events during its commensal observations.

1.5.2 LADUMA

LADUMA is short for Looking At the Distant Universe with the MeerKAT Array (Blyth et al. 2016). It uses the MeerKAT radio telescope to help astronomers learn more about how galaxies have evolved over an incredibly long time, around 9 billion years, which is more than two-thirds of the universe's age (Blyth et al. 2016). LADUMA has chosen a particular region of the sky called the Chandra Deep Field South (CDFS) at coordinates RA of $03^h32^m30.4^s$ and DEC of $-28°07^{'}57^{''}$ (J2000) (Blyth et al. (2016)). This region is perfect for their work because it has already been studied extensively by other telescopes, and there is a lot of multiwavelength information available. The CDFS is a great choice because it's in the southern part of the sky, making it easier to observe for longer periods. This is important for certain types of observations, and it helps to reduce interference from radio signals on Earth. LADUMA's primary goal is to use its observations of hydrogen gas to figure out how galaxies have changed over most of the universe's history (Blyth et al. 2016). It is believed that with MeerKAT, they will be able to address questions such as: How does the HI mass function depend on environmental density and redshift? How does the cosmic neutral gas density traced by HI emission evolve to high redshift? How do galaxies HI depend on their stellar masses? Lastly how does the baryonic Tully-Fisher relation evolve over cosmic time? The deep nature of LADUMA observations makes it an ideal field for commensal searches of radio transients and variables. In this thesis, I use the LADUMA data to conduct commensal transient searches.

1.6 IDIA and TraP

1.6.1 IDIA

The Inter-university Institute for Data Intensive Astronomy, also known as IDIA, is a collaboration involving three prominent South African universities: the Universities of Cape Town, Western Cape, and Pretoria [1]. The primary objective of IDIA is to nurture and enhance the capacity and expertise of the South African university research community in the field of data-intensive research. This empowers researchers to play a role in global projects, particularly on projects related to the MeerKAT large survey science and other SKA pathfinder telescopes, ultimately leading to leadership on SKA phase 1 Key Science programs. IDIA stands as the central platform serving five out of eight MeerKAT large survey projects, including ThunderKAT. IDIA allows scientists to apply the scientific methods effectively, including tasks such as data visualization, re-processing, hypothesis testing, without the frustrating delays that large datasets typically entail through a sub-branch Cube Analysis and Rendering Tool for Astronomy (CARTA) (Comrie et al. 2021). Furthermore, the cloud technology creates opportunities for real-time global collaboration, as analytical tools reside in the cloud and can be accessed and utilized by collaborators worldwide.

1.6.2 The Transient Pipeline (TraP)

The LOFAR Transient Pipeline, known as TraP (Swinbank et al. 2015, Rowlinson et al. 2019) is a software or data processing system designed to detect and analyze transient and variable astronomical sources that exhibit changes in their radio emissions over time, such as supernovae, pulsars and others observed using the LOFAR radio telescope as well as MeerKAT.

The TraP pipeline analyzes three-dimensional time-series data, primarily cube images with two spatial dimensions and one frequency dimension. The pipeline begins with quality checks to ensure data reliability, then automatically

---

[1] About IDIA, 2015, accessed November 03, 2023, `https://idia.ac.za/about-idia/`

evaluates parameters like signal-to-noise ratios and calibration stability to flag any unusable data. After data filtering, the pipeline generates sky images, identifying emission from sources against background noise, and extracts sources using algorithms such as background estimation, thresholding source detections, deblending and source characterisation lastly final parameter extraction. The first step in the pipeline involves understanding and modelling the background noise across the images. mages are divided into grids to model background noise. The grid size balances between avoiding influence from extended sources and tracking background variations. Background and noise levels are estimated via iterative clipping, which filters out source-contaminated pixels. This step is crucial for an accurate background model, particularly in crowded fields. Once this is done, the background model is subtracted from the image, leaving potential sources. A detection threshold, based on the noise profile, identifies pixels that form source candidates. The process is designed to minimise false positives while maintaining sensitivity to faint sources. Detected sources are deblended, separating overlapping sources into distinct components. Each source is then characterised by estimating its position, flux, and shape, often using elliptical Gaussian fitting to refine parameters and estimate uncertainties. The final step in the source extraction process involves extracting and storing the parameters of each source, including its position, flux density, and morphological characteristics. These parameters are critical for subsequent studies, such as identifying the nature of the sources or monitoring their variability over time. The careful calibration and fitting procedures ensure that the extracted parameters are as accurate as possible, providing a solid foundation for further scientific investigation. These sources are cross-referenced across observations, associating them with known celestial objects when possible. It also generates light curves showing source brightness over time. The result is a catalog of detected sources with quality flags indicating data reliability. The outputs provided by TraP show the transient and variable nature of celestial sources. These outputs includes the sources light curves and variability parameters. The variability parameters are used for quantifying the variability of transient sources. Astronomers can analyze how the brightness of these sources change over time, to understand their dynamic behaviour. The η_ν parameter is used to measure the normalized excess variance of a light curve, quantifying the amount of variability in the flux of a source compared to its average flux. It is heavily based on the reduced chi-squared statistic χ^2. A high η_ν value suggests substantial variability, while a low or negative η_ν value indicates a stable source. It compares the observed variations in flux to the expected variability due to measurement errors. This parameter is given by:

$$\eta_\nu = \chi^2_{N-1} = \frac{1}{N-1}\sum_{i=1}^{N}\frac{(F_{\nu,i}-\delta^2_\nu)^2}{\sigma^2_{\nu,i}} \tag{1.10}$$

where N denotes the number of data points in the light curve, $F_{\nu,i}$ and $\sigma_{\nu,i}$ being the flux and associated uncertainty at some observed frequency v and lastly δ_ν is the weighted mean flux density. The weights are given by $w_\nu = \frac{1}{\sigma^2_\nu}$. The V_ν parameter quantifies the variability of flux measurements by comparing the sample standard deviation to the mean of these measurements. This parameter is given by:

$$V_\nu = \frac{S_\nu}{\overline{F_\nu}} = \frac{1}{\overline{F_\nu}}\sqrt{\frac{N}{N-1}(\overline{F^2_\nu} - \overline{F_\nu}^2)} \tag{1.11}$$

where S_ν, $\overline{F_\nu}$ and N denotes the light curves standard deviation, mean and number of data points in a given light curve respectively. For a given source, we have that a low V_ν value depict a limited range of flux densities, while a substantial V_ν value suggests a wide dispersion in flux densities, reflecting heightened variability. The V_ν parameter does not account for uncertainties, which means that sources with low signal-to-noise ratios might erroneously appear variable, even if their flux densities remain stable (Driessen et al. 2022). Sources that exhibit high values in both η_ν and V_ν are often candidate sources (Andersson et al. 2022). For a more detailed description of the TraP see (Swinbank et al. 2015, Rowlinson et al. 2019). In this thesis, I have used TraP as implemented on the cloud-based, ilifu (which means cloud in isiXhosa) on IDIA.

1.7 MeerLICHT

MeerLICHT is a 0.65-m fully automated optical telescope located at the Sutherland station of the South African Astronomical Observatory. It aims to provide simultaneous, real-time observations of the radio-transient sky as observed by MeerKAT, covering a broad field of view of 2.7 square degrees (Bloemen et al. 2016). The MeerLICHT telescope follows a Dall-Kirkham optical design and has a 10560×10560 CCD , this enables the wide field of view coverage. The telescope uses a set of filters (u, q, r, i, z) and a wide-band (440 - 72) nm q-band filter to capture data across a range of wavelengths (Bloemen et al. 2016). Data from MeerLICHT are processed automatically through a pipeline developed by MeerLICHT and BlackGem projects called the BlackBox Pipeline (Vreeswijk et al. 2021). MeerLICHT's main goal is to study astrophysical transients across multiple electromagnetic spectrum windows. This is accomplished by investigating the transient radio Universe alongside MeerKAT's ThunderKAT large survey project. The commensal approach to MeerKAT science, combined with the wide fields of view of both MeerKAT and MeerLICHT, enables astronomers to search extensive areas of the southern skies for variable and transient objects (Driessen et al. 2022).

1.8 Research Goal

The main aim of this thesis is to leverage SARAO SDP images (These are the output products generated by the data processing pipelines of SARAO's radio telescopes, such as MeerKAT. These images result from the calibration, imaging, and analysis processes applied to the raw data collected by the telescopes. The primary aim of SDP images is to produce Quality Assessment (QA) metrics, enabling stakeholders to assess the quality of a particular observation. However, there is also an intention that these products become scientifically usable.) for commensal searches of radio variables and transients in the LADUMA field. This involves initially processing the images through a transient pipeline and subsequently utilising the obtained results for in-depth analysis. The focus of this thesis is on observations of the field at the lowest MeerKAT's frequencies, specifically in the UHF band at 0.816 GHz. The primary objective is to investigate whether the SDP images can serve as valuable data straight from the telescope, aiding in the efficient detection and characterization of transient and variable radio sources. The research further aims to contribute to the classification of any newly identified radio transients and variables in the LADUMA field.

Chapter 2

Observations and methodology

This chapter details the MeerKAT observations and our methodology for transient searches. We describe the MeerKAT observations of the LADUMA field in the UHF band, followed by a description of transient search methods, including validation of LADUMA L-band SDP images by comparing them with data from the same observations reduced by OxKAT (refer to Section 2.1.2). We then discuss the search for multi-wavelength counterparts of radio transients and variable candidates, covering cross-matching with VizieR catalogues, Aladin sky atlas usage, and the exploration of rand of optical synoptic surveys such as ASAS-SN, CRTS, MeerLICHT, and TESS.

2.1 MeerKAT Observations of the LADUMA field

The data used in this thesis were obtained from the ThunderKAT commensal transient searches program and are centred on the LADUMA field, a single pointing at a Right Ascension of 53.1267 deg and Declination of -28.1325 deg. Deep observations of the LADUMA field in the UHF band from 2 November 2021 to 12 November 2022, season 1 and 2 were used. The term 'season' refers to a specific period during which MeerKAT observes distinct regions of the sky within the LADUMA field. The frequency ranges from 580 - 1015 MHz, the lowest frequency band of the MeerKAT telescope. A total of 48 SDP images were obtained, with the observation time per epoch ranging from a minimum of $\sim$ 5 hours to $\sim$ 10 hours at a fixed frequency of 816 MHz across all epochs.

The data processing happens in an automated manner, where images are produced using the SARAO Science Data Processor (SDP) pipeline. The pipeline processes the data in three crucial steps : "SDPcal Pipeline", "Continuum Pipeline" and "Spectral Pipeline" [2] . The SDPcal Pipeline is initiated within 15 minutes of completion of the observations and thus takes charge of the real time data streaming from the MeerKAT telescope. The main objective here is to generate Radio Frequency Interference (RFI) flags and derive precise calibration solutions. In the 32k mode of the MeerKAT correlator, the pipeline efficiently divides the data into four frequency bands and processes them concurrently on separate servers. This division allows users the flexibility to choose specific categories of flags tailored to their data. The 32k mode mentioned above refers to an observational mode in which the telescope's correlator processes data using 32k frequency channels. This mode is particularly useful for observing narrow spectral lines, studying the fine details of radio signals, or searching for radio transients with high precision in frequency. The

---

[2] SKA Africa, "SDP Pipelines Overview," accessed January 16, 2023,https://skaafrica.atlassian.net/wiki/spaces/ESDKB/pages/338723406/SDP+pipelines+overview#Workflow-and-Products

result is a dataset cleaned of radio frequency interference, and ready for further analysis.

Next, the Continuum Pipeline takes charge of observations that exceed the initial 15 minutes. It takes $\sim$ 10 hours for an 8 hour observation window. The main function of the pipeline is to include the creation of a continuum image and the development of a model for continuum subtraction. This is essential as the continuum sky model is needed for the isolation of spectral line emission from the continuous, broad-spectrum radiation. The continuum images then go through primary beam correction. This correction involves dividing the image by the model primary beam, thus refining the accuracy of the final results. The Spectral Pipeline produces the final images including a single channel FITS image for each given channel up to 32k. In this thesis we use the SDP images for commensal transients searches. Since the SDP images are not optimized for science, we validate the use of these images in Section 2.1.2.

2.1.1 Image Filtering

We used a total of 48 images for our commensal transient search. Before inserting these images into the TraP, it was necessary to filter out those considered “bad”. Radio images can be deemed “bad” due to various factors, including interference from man-made sources (like electronics) or natural phenomena (such as lightning), which introduce noise. Poor calibration, especially in gain and phase, can distort images, while inadequate u-v coverage or short observing times result in missing information and artifacts. Imaging issues like side lobes and errors in deconvolution further degrade quality. Low signal-to-noise ratios, often due to thermal noise or adverse weather, add graininess, and dynamic range limitations obscure faint sources. Finally, systematic errors, including instrumental malfunctions or incorrect data processing, alongside inaccurate sky models, can all contribute to poor image quality. This step aimed to ensure that the images subjected to the TraP would pass quality control and yield reliable results. We identified “bad” images as those containing numerous artifacts or exhibiting a high level of noise. We employed two filtering methods: manual inspection and assessment of the noise levels. We visually inspected the images using CARTA software (Comrie et al. 2021), applying a 99.9% linear scale to enhance visibility. Any images showing visual irregularities, as demonstrated in Figure 2.3a, were flagged and categorized as “bad”.

During the inspection, we looked for signs of clear artifacts, such as those depicted in Figure 2.3a. Subsequently, we identified and removed two such images from the dataset intended for TraP, as indicated in the Table 2.1.

For the second method, we used a python script to calculate the noise levels for each image in our sample and determined the mean noise level and its standard deviation. We opted for a 3σ cutoff as can seen in Figure 2.2, indicating our interest in images with noise levels within three standard deviations. This limit was chosen to facilitate quality control and identify obvious outliers in the noise levels, ensuring that the images selected for the transient search were reliable. The mean RMS of our dataset is 13.96 ± 0.72 μJy. As a result, an additional five images were flagged as “bad” due to noise levels exceeding the established limit. Subsequently, we generated a plot illustrating the relationship between the images and their corresponding noise levels, as shown in Figure 2.2. This visualization provides a comprehensive overview of the noise distribution in the dataset, further aiding in the identification and exclusion of images with unreliably high noise levels. The refined set of images meeting the noise level criteria was then deemed suitable for the transient search, minimizing the likelihood of false positives in the results.

At this stage 43 images passed all our selection steps and were now ready to be processed with the TraP. It is however, worth mentioning in detail, the validation for the use of SDP images for transient searches before running TraP on the UHF band. SDP images are primarily intented for quality assessment purposes and its use for scientific purposes remains to be validated. In the next Section 2.1.2 we show how we validated the use of SDP images by

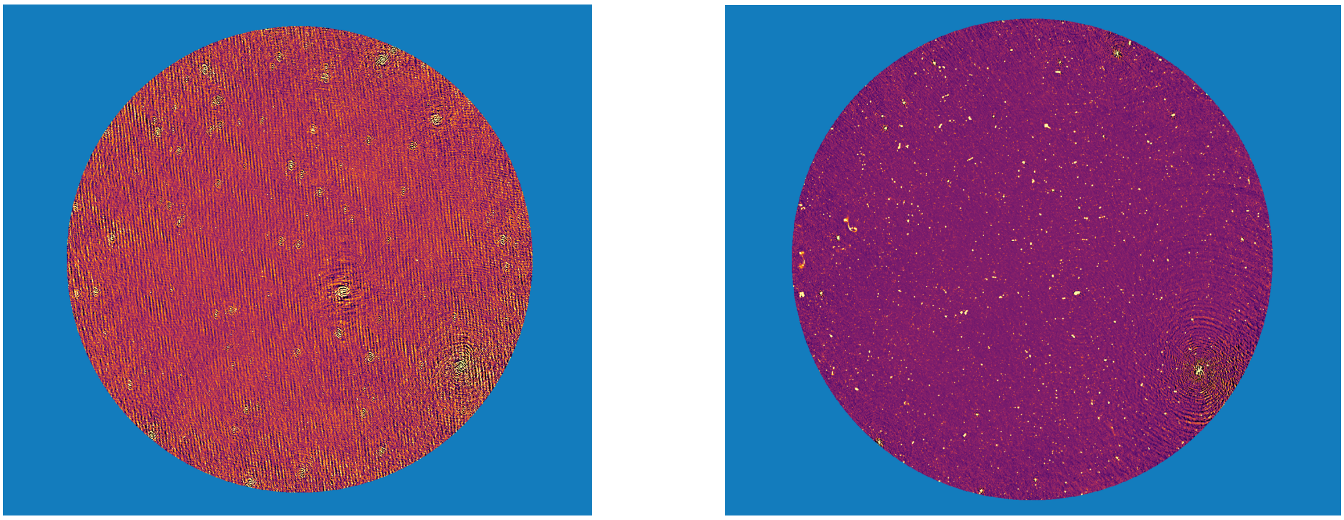

(a) Figure 1

(b) Figure 2

Figure 2.1: The image on the left (a) is an example of a visually “Bad” image. This is image ID 1661391366 from our sample (Table 2.1). While the image on the right (b) is image ID 1658966171, this is an image from the sample images that passed the visual phase of the filtering.

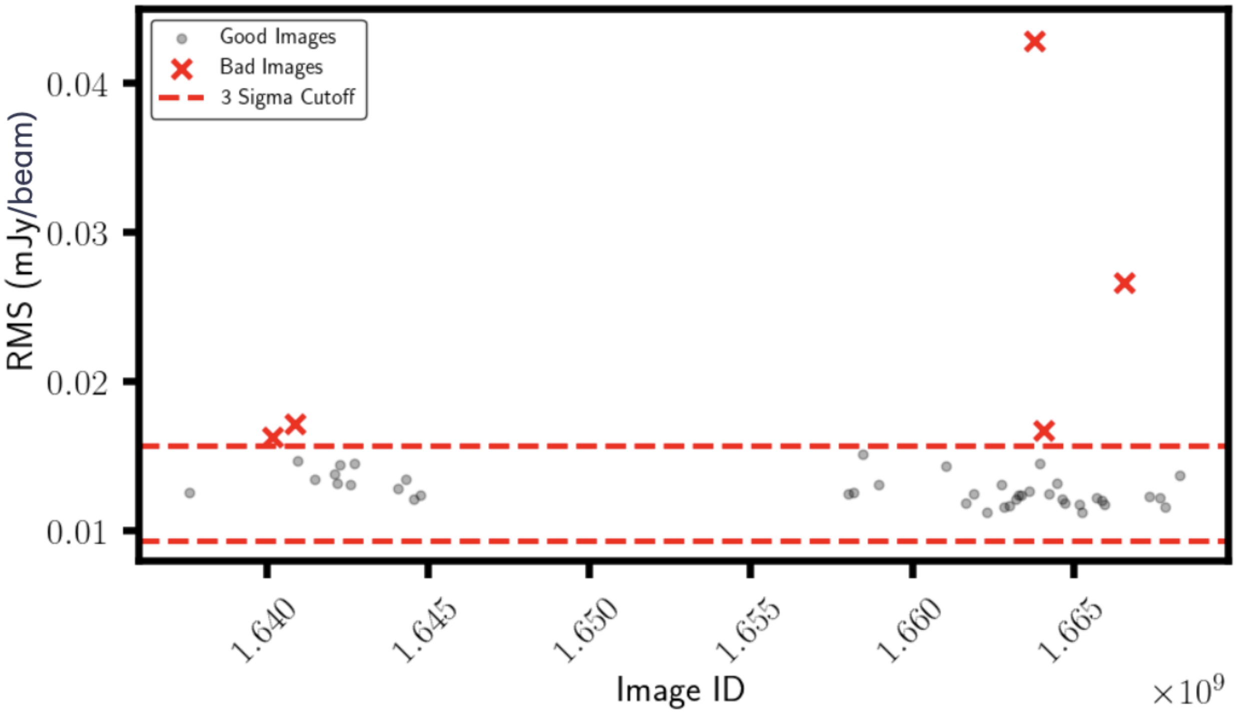

Figure 2.2: All 48 images (excluding epoch 11 and 21, see Table 2.1), good and bad, shown against their noise levels, along with a 3σ (“σ” in the context of this plot is the standard deviation of a list of noise measurements) cutoff limit.

comparing the SDP images with fully calibrated OxKAT reduced images of the LADUMA field in the L-band.

Epoch	Image ID	Date	UTC Start Time	UTC End Time	MJD	RMS (mJy/beam)	Status
1	1637602051	2021-11-22	17:29:13	00:44:22	59540.88	0.013	Good
2	1640194279	2021-12-22	17:33:54	00:14:58	59570.88	0.017	Bad
3	1640885597	2021-12-30	17:34:59	23:41:59	59579.37	0.018	Bad
4	1640972173	2021-12-31	17:38:09	23:45:09	59580.37	0.015	Good
5	1641490520	2022-01-06	17:38:12	23:44:24	59586.37	0.014	Good
6	1642093878	2022-01-13	17:13:09	23:22:38	59593.35	0.014	Good
7	1642181477	2022-01-14	17:33:12	23:05:27	59594.35	0.014	Good
8	1642267950	2022-01-15	17:34:21	23:06:21	59595.35	0.015	Good
9	1642613170	2022-01-19	17:27:42	22:25:36	59599.34	0.014	Good
10	1642700870	2022-01-20	17:48:15	22:40:54	59600.35	0.015	Good
11	1643715069	2022-02-01	11:32:45	21:31:28	59612.19	-	Visually Bad
12	1644059590	2022-02-05	11:14:50	21:15:15	59616.18	0.013	Good
13	1644318129	2022-02-08	11:03:53	21:04:02	59619.17	0.014	Good
14	1644752473	2022-02-13	11:42:54	21:38:51	59624.20	0.013	Good
15	1644576673	2022-02-11	10:52:46	20:53:04	59622.17	0.013	Good
16	1658030772	2022-07-17	04:04:49	10:35:12	59777.81	0.013	Good
17	1658192293	2022-07-19	00:59:52	08:37:23	59779.71	0.013	Good
18	1658449093	2022-07-22	00:19:29	06:03:43	59782.64	0.016	Good
19	1658966171	2022-07-27	23:56:44	07:28:12	59788.16	0.014	Good
20	1661046814	2022-08-21	01:54:56	09:27:11	59812.74	0.015	Good
21	1661391366	2022-08-25	01:37:31	08:42:48	59816.72	0.582	Visually Bad
22	1661637077	2022-08-27	21:52:37	07:05:40	59819.11	0.012	Good
23	1661895557	2022-08-30	21:40:38	05:12:37	59822.07	0.013	Good
24	1662326779	2022-09-04	21:27:39	06:57:33	59827.10	0.012	Good
25	1662843383	2022-09-10	20:57:37	06:28:50	59833.08	0.014	Good
26	1662767184	2022-09-09	23:47:47	07:26:21	59832.16	0.012	Good
27	1663015699	2022-09-12	20:49:42	06:20:39	59835.07	0.012	Good
28	1663188078	2022-09-14	20:42:38	06:13:43	59837.07	0.013	Good
29	1663274258	2022-09-15	20:38:57	06:08:50	59838.06	0.013	Good
30	1663368199	2022-09-16	22:44:38	07:12:33	59839.13	0.013	Good
31	1663619479	2022-09-19	20:32:44	06:04:04	59842.06	0.013	Good
32	1663791375	2022-09-21	20:17:36	05:48:41	59844.05	0.043	Bad
33	1663963575	2022-09-23	20:07:39	05:38:44	59846.04	0.015	Good
34	1664049680	2022-09-24	20:02:39	02:10:42	59846.97	0.017	Bad
35	1664228310	2022-09-26	21:39:48	07:11:17	59849.11	0.013	Good
36	1664480802	2022-09-29	19:48:04	05:17:58	59852.03	0.014	Good
37	1664653281	2022-10-01	19:42:41	05:12:34	59854.02	0.013	Good
38	1664739015	2022-10-02	19:31:33	05:01:27	59855.02	0.012	Good
39	1665175572	2022-10-07	20:47:41	06:20:05	59860.07	0.012	Good
40	1665255975	2022-10-08	19:07:39	04:37:25	59861.00	0.012	Good
41	1665688881	2022-10-13	19:22:43	04:58:24	59866.01	0.013	Good
42	1665864898	2022-10-15	20:16:16	03:53:16	59868.01	0.013	Good
43	1665948077	2022-10-16	19:22:32	04:58:13	59869.01	0.012	Good
44	1666553482	2022-10-23	19:32:47	05:04:39	59876.02	0.027	Bad
45	1667331070	2022-11-01	19:32:27	05:01:10	59885.02	0.013	Good
46	1667675546	2022-11-05	19:13:44	04:41:08	59889.00	0.013	Good
47	1667849352	2022-11-07	19:30:31	04:28:19	59891.00	0.012	Good
48	1668271473	2022-11-12	16:45:58	01:43:53	59895.89	0.014	Good

Table 2.1: All 48 images with their calculated noise levels, the time and date of observation. We also show whether the images were flagged as good or bad.

2.1.2 OxKAT Images

In this section we compared the OxKAT images with the SDP images, both in L-band. OxKAT images are images that have been produced using OxKAT (Heywood 2020). OxKAT automates full calibration and imaging of MeerKAT radio telescope data, handling raw visibilities in Measurement Set format. OxKAT covers flagging, reference calibration, imaging, self-calibration, and optionally, direction-dependent calibration. OxKAT scripts use python and integrate various radio astronomy software packages like CASA (McMullin et al. 2007) for gain and bandpass calibration, self-calibration, and flagging. WSClean (Offringa et al. 2014) is then used for imaging. CubiCal (Kenyon & Smirnov 2018), and DDfacet (Tasse et al. 2018) are also available for direction dependent effect calibrations and imaging procedures. DDFacet is particularly powerful for high-precision imaging, as it allows for adaptive faceting, dividing the sky into small facets to apply different calibration solutions based on varying observing conditions across the field of view. The OxKAT data for this analysis were provided by Dr Ian Heywood (University of Oxford).

On the other hand, the SDP pipeline uses Obit for imaging, which also involves faceting, but with a different approach. While the specifics of the algorithm used in Obit, including the robust weighting parameter, are not well-documented for the SDP images, it is clear that the faceting approach in Obit is more focused on operational efficiency and streamlining the real-time processing of large datasets. Obit's primary goal is not to achieve the highest possible scientific precision but rather to enable rapid data throughput and image creation for monitoring and commensal transient searches. The choice of algorithms underscores a major difference in how these two pipelines are optimised. DDFacet, used in OxKAT, is designed for detailed scientific analysis, enabling corrections for direction-dependent effects and fine-tuning through weighting schemes. In contrast, Obit is more generalised and does not provide the same level of control or sophistication, which may explain some of the observed differences between the two datasets. Unfortunately, the documentation does not specify the exact robust parameter used in the SDP's Obit processing, leaving some uncertainty about how image weighting influences the final products.

In terms of Radio Frequency Interference (RFI) mitigation, both pipelines flag and clean RFI, but their approaches differ. The SDP pipeline's real-time RFI flagging and calibration, performed during the SDPcal step, is tailored for efficiency. It operates in near-real-time, ensuring the data are ready for streaming or further processing shortly after observation. OxKAT, however, incorporates more advanced self-calibration techniques and allows users to manually configure additional RFI flagging options, potentially resulting in cleaner final products.

The SDP images are not optimised for scientific analysis. Therefore, comparing the SDP and OxKAT images in the L-band with the aim of assessing the number of sources detected using the TraP can provide valuable insights and justification for using SDP images in commensal transient searches, even in the UHF band where we do not have OxKAT images available. The primary difference between the two bands is the frequency range, but conducting this comparison in L-band, where calibration and RFI handling are more robust, allows us to assess the feasibility of using SDP images for real-time transient searches. This approach aligns with our broader objective of transitioning towards real-time transient searches. For this comparison, we utilised L-band images from the first season of the LADUMA survey observations. A further discussion on this comparison is given in Section 2.2.3.

2.2 Transient Searches

2.2.1 Setting up TraP

The setup process started with the establishment of a PostgreSQL database for hosting the TraP on IDIA. Alexander van der Horst (George Washington University) provided key assistance with customising access credentials, and configuring the database on the IDIA infrastructure using the ThunderTraP virtual machine. The TraP setup involved configuring environmental variables and executing various scripts. Adjustments were made to the `trapenvvar.bash` script to include necessary database credentials. Subsequently, the project initialisation was performed with the command: `trap-manage.py initproject myproject`. The project initialization resulted in the creation of a directory named `myproject`, containing a number of important scripts. The `pipeline.cfg` script within the `myproject` directory was modified by setting `copy_images` to `False` with the aim of disabling image duplication, optimising storage usage. Following the project initialisation, the PostgreSQL database was initialized using the command: `trap-manage.py initdb -y`. The job initialization was conducted using the command: `trap-manage.py initjob myjob`. This action created a directory named `myjob`, containing scripts for job execution. Further configuration details are elaborated in Section 2.2.2.

2.2.2 Running TraP

Before initiating the TraP run, we performed the following steps: We edited the `images_to_process.py` script to specify the locations of all the images we intended to process. Further, we adjusted the `job_params.cfg` script to define the TraP settings. Table 2.2 outlines the modified settings in the `job_params.cfg` script, while the remaining parameters were left at their default values. We set the `detection_threshold` to 8σ, aiming to identify both faint and bright sources. This choice was influenced by similar MeerKAT transient studies such as Driessen et al. (2022), Andersson et al. (2022), and Rowlinson et al. (2022). Despite increasing the likelihood of false positives, this threshold was selected. The `extraction_radius_pix` was set to 2303 pixels, slightly below half of the image size, to avoid unreliable flux measurements near the image edges. We configured `force_beam` to `True` to emphasise the detection of unresolved point sources and their variability. The `deblend_nthresh` parameter was adjusted to the value seen in Table 2.2 to address potential overlaps between nearby sources. The `beamwidths_limit` was configured to account for source associations. Following these preparations, we initiated the TraP run by editing the `trap_run.sbatch` script to match our job name. The `sbatch trap_run.sbatch` command was executed on a terminal, dispatching our TraP job to the cluster for processing.

Parameters	Set Value
`force_beam`	`True`
`extraction_radius_pix`	`2303 pixels`
`deblend_nthresh`	`10`
`beamwidths_limit`	`1.0`
`detection_threshold`	`8`

Table 2.2: This shows the parameters that were changed in the `job_params.cfg` script in preparation to run TraP on the UHF dataset.

2.2.3 Validation of the SDP images for transient searches

We selected 11 matching epochs from both the SDP and OxKAT L-band data to verfy the use of SDP images (see Section 2.1.2). These 11 images were then processed through the TraP following the methodology outlined in Section 2.2. The TraP parameters remained unchanged, except for adjusting the `extraction_radius_pix` to `2150 pixels` for the OxKAT reduced images and `2016 pixels` for the L band SDP images. This adjustment was necessary due to the differing angular pixel sizes between the OxKAT and SDP images, ensuring that we were examining the same region in both sets of images as shown in Figure 2.3. Both sets of images underwent TraP processing using this extraction radius. After the TraP processed the images and produced outputs for both datasets, we applied the same filtering process to both the SDP and OxKAT images. For a comprehensive analysis, we initially compared both the unfiltered datasets and then proceeded to analyze the filtered datasets quantitatively. The source coordinates from the OxKAT dataset were used and cross-matched with coordinates in the SDP dataset. The objective was to determine the number of sources detected in the SDP dataset that were also present in the OxKAT dataset. Sources present in the OxKAT images but absent in the SDP images were manually and visually inspected. This involved examining their light curves, as well as their η_ν and V_ν values, and vetting them to identify potential transients or variables. Additionally, we observed that the OxKAT images had lower RMS measures compared to the SDP images. The mean RMS in OxKAT images was 3.42 ± 0.03 μJy/beam, while in SDP images, it was 4.20 ± 0.06 μJy/beam also seen in Table 2.3, indicating better noise characteristics in the OxKAT data. This discrepancy in RMS measures warrants further discussion regarding the implications for source detection sensitivity and data quality assessment. Angular resolution differences also play a role. OxKAT may offer higher angular resolution, leading to better source separation and lower confusion noise, which reduces RMS. In contrast, SDP images have coarser resolution, contributing to higher RMS due to increased source blending. These differences impact the sensitivity of source detection, with OxKAT being potentially more sensitive to faint sources. Despite the higher RMS measures in the SDP images, the comparison of these images remains crucial for validating the use of SDP images for commensal transient searches, particularly as this thesis focuses on utilizing SDP images in the UHF band for detecting variable and transient sources. Results of this analysis are presented in Section 3.1.

Epoch	Image ID	MJD	OxKAT RMS (mJy/beam)	SDP RMS (mJy/beam)
1	1601325069	59119	0.0036	0.0039
2	1601409818	59120	0.0034	0.0043
3	1601756163	59124	0.0034	0.0044
4	1601928962	59126	0.0034	0.0039
5	1602098167	59128	0.0034	0.0041
6	1602183844	59129	0.0035	0.0042
7	1602270065	59130	0.0034	0.0040
8	1602704665	59135	0.0033	0.0046
9	1602792067	59136	0.0034	0.0042
10	1602873187	59137	0.0035	0.0043
11	1602964865	59138	0.0034	0.0043

Table 2.3: The 11 selected images in both SDP and OxKAT used for the comparison. The image ID is the same in both sets of images, the local RMS is also shown in the table, with the SDP images exhibiting slightly higher noise levels compared to the local OxKAT images.

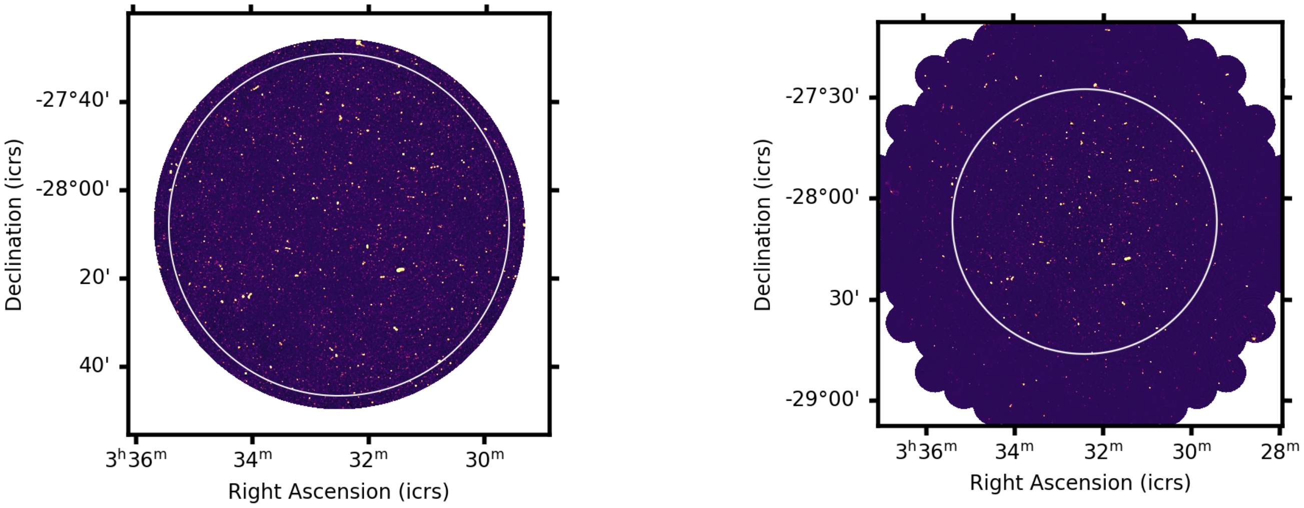

(a) Figure 1 (b) Figure 2

Figure 2.3: The image on the left (a) is an OxKAT reduced image. This is image ID 1601325069 from our sample (Table 2.3). The image on the right (b) is the matching epoch from the L band SDP images. The white circle in both images corresponds to a diameter of 1.314 degrees, a common area in the two data sets.

Images	Frequency (GHz)	Pixel size (degrees)	Pixel increment	Radius (degrees)	Mean RMS (μJy/beam)
SDP UHF band	0.816	5.128E-04	1.85"	1.23	13.96 ± 0.72
SDP L band	1.284	3.259E-04	1.17"	0.98	4.20 ± 0.06
OxKAT L band	1.284	3.055E-04	1.10"	0.70	3.42 ± 0.03

Table 2.4: Showing the LADUMA images in both L and UHF band with their respective observed frequencies. We also show the associated image size in degrees as well as the mean RMS of the images.

2.3 Analysing the output from TraP

The TraP output provided us with a catalog of **7299** detected transient candidates in the UHF dataset, as depicted in Figure 2.4. Notably, not all of these detections represent genuine variable or transient sources. Therefore, further filtering or vetting of each source was necessary to ascertain its authenticity. As noted in Gourdji et al. (2022), sources detected by the TraP can be categorized into several groups, including potential real variables or transients, image artifacts originating from side-lobes around very bright sources, noise, extended sources between epochs, and faint sources detected near the detection threshold in subsequent images but not in the first due to high local RMS. Because our primary interest is in potential astrophysical transients and variables, we applied a filtering process to eliminate non-point sources such as extended sources. These extended sources often exhibit spurious variability due to differences in fit parameters between epochs, rather than intrinsic variability. By focusing on unresolved point sources, we mitigate the risk of including artefacts related to calibration differences or noise variations, which are common in low signal-to-noise regions. This step also helps reduce the number of sources requiring manual inspection, as discussed in Driessen et al. (2022) and Andersson et al. (2022).

2.3.1 The η_ν and V_ν Filtering

Our focus was on identifying sources that stood out as outliers from the general distribution of points in the η_ν-V_ν plot (see Figure 2.4). Sources with high values in both η_ν and V_ν were deemed potential variables or transients, as detailed in Section 1.6.2. We defined stable sources as those whose histograms of η_ν and V_ν values exhibit a Gaussian distribution, with outliers representing potential variables and transients, as explained in Rowlinson et al. (2019). Subsequently, we applied a 2σ threshold from the mean values of both η_ν and V_ν, consistent with methods used in the literature. The choice of 2σ is standard in transient and variable source studies, ensuring we capture significant deviations while accounting for possible non-Gaussian distributions. This approach is slightly more strict than the 1.5σ threshold used by Rowlinson et al. (2022) and provides a practical balance between strictness and inclusivity. Moreover, we considered whether extreme outliers should be excluded from the mean and sigma calculations. Given that our dataset did not contain obvious extreme values, we opted to include all sources in these calculations. This approach ensures that potential outliers identified are genuine rather than statistical artefacts. Other filtering approaches, such as using only η_ν as in Chastain et al. (2023), would have been more conservative, but by using both η_ν and V_ν, we maximise the chances of capturing real transients while minimising false positives. For the MeerKAT observations of the LADUMA field at a frequency of 0.816 GHz, the 2σ thresholds for η_ν and V_ν were determined to be 0.30 and 334.12, respectively.

After setting up these limits, there were no obvious outliers, as seen in Figure 2.4. In principle, obvious outliers would reside on the upper right of the plot in the red region of Figure 2.4, but this was not the case in our dataset. However, this did not mean that there were no potential variables or transients in our dataset; rather, it meant that the η_ν and V_ν limits (vertical and horizontal purple dashed lines) we set were biased towards sources that are high in both η_ν and V_ν. We then decided to further filter the sources by examining those above the green region seen in Figure 2.4. The reason for this is that we noted these sources had reasonably high η_ν and V_ν values, making them viable candidates as potential variables or transients.

A closer look at the light curves revealed a correlated behaviour for sources in the catalog, similar to what was observed in (Driessen et al. 2022). In the next subsection, we demonstrate how we addressed this correlation in the light curves.

2.3.2 Systematics

We obtained all light curves from the TraP output using a python script to access the PostgreSQL database. We then we manually inspected the remaining light curves. Our analysis revealed correlated behaviour or similar trends in some light curves, consistent with findings reported by Driessen et al. (2022). This correlation is likely due to systematic errors, including resolved sources appearing variable and spatial or directional dependencies. To quantify this correlation, we calculated Pearson's correlation coefficient (r) between randomly selected pairs of sources. Positive r values indicate positive correlation, negative values indicate negative correlation, and 0 indicates no linear correlation. Comparison plots were generated for sources with matching r values, and Figure 2.5 illustrates an example. Additionally, highly correlated sources were visually represented.

2.3.2.1 Flux dependency

We observed that filtering out resolved sources and those with directional dependency only reduced our sample size without necessarily resolving the light curve correlation issue, as noted by Driessen et al. (2022). This left us with

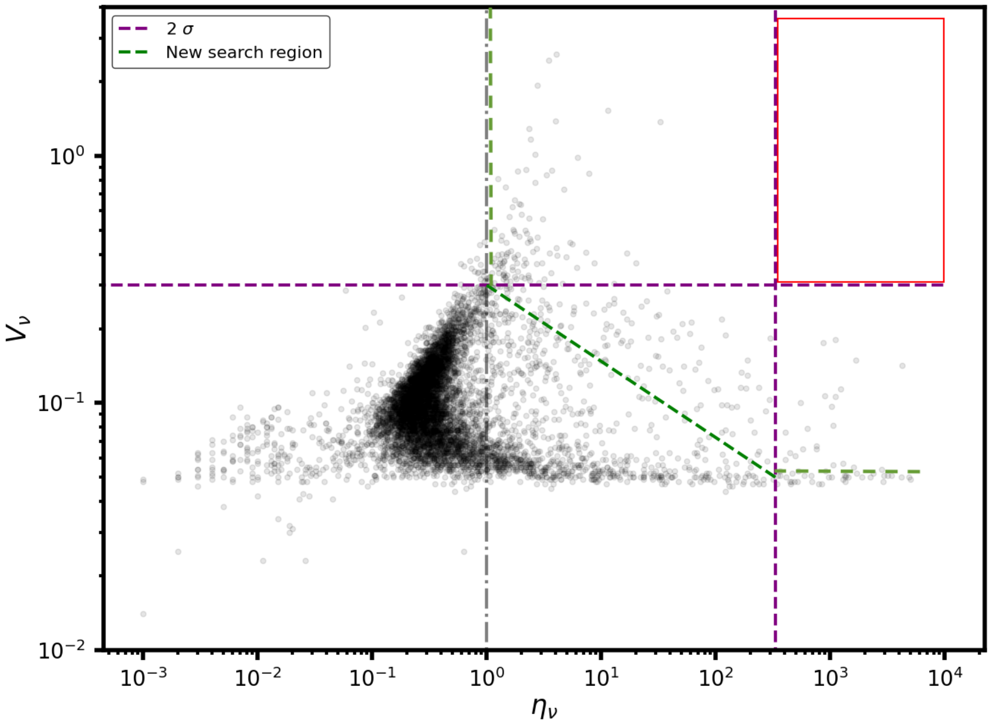

Figure 2.4: The η_ν-V_ν plot displaying all sources identified by the TraP. The search regions for transients are highlighted, with filtering limits set at 0.3 and 334.12 (2σ from the mean) for η_ν and V_ν, respectively. The red box indicates the classic region where outliers are typically found, while the green regions represent the newly selected areas for our transient and variable searches.

one remaining systematic to investigate: flux dependency. One key motivation for this investigation was to assess whether bright sources were affected by these systematics, as suggested by Driessen et al. (2022). The next step involved correcting our light curves, following the methodology outlined by Driessen et al. (2022). This entailed modeling an "ideal" light curve and dividing the original light curves by this modeled curve. We chose the last epoch of the images as the reference epoch to ensure that all detected sources had a measurement in this epoch. The division process was expressed mathematically as:

$$F_{i,j,scaled} = \frac{F_{i,j}}{F_{i,\text{ref epoch}}}, \tag{2.1}$$

where $F_{i,j}$ represents the flux density of source i in epoch j, and $F_{i,\text{ref epoch}}$ represents the flux density of the same source in the reference epoch. We found that using the median and the mean absolute deviation (MAD) model for correction was more robust than using the mean.

The equation for the standard deviation (σ_F) is given by:

$$\sigma_F = \sqrt{\frac{1}{n(n-1)} \sum_{i=0}^{n} (F_i - \bar{F})^2} \tag{2.2}$$

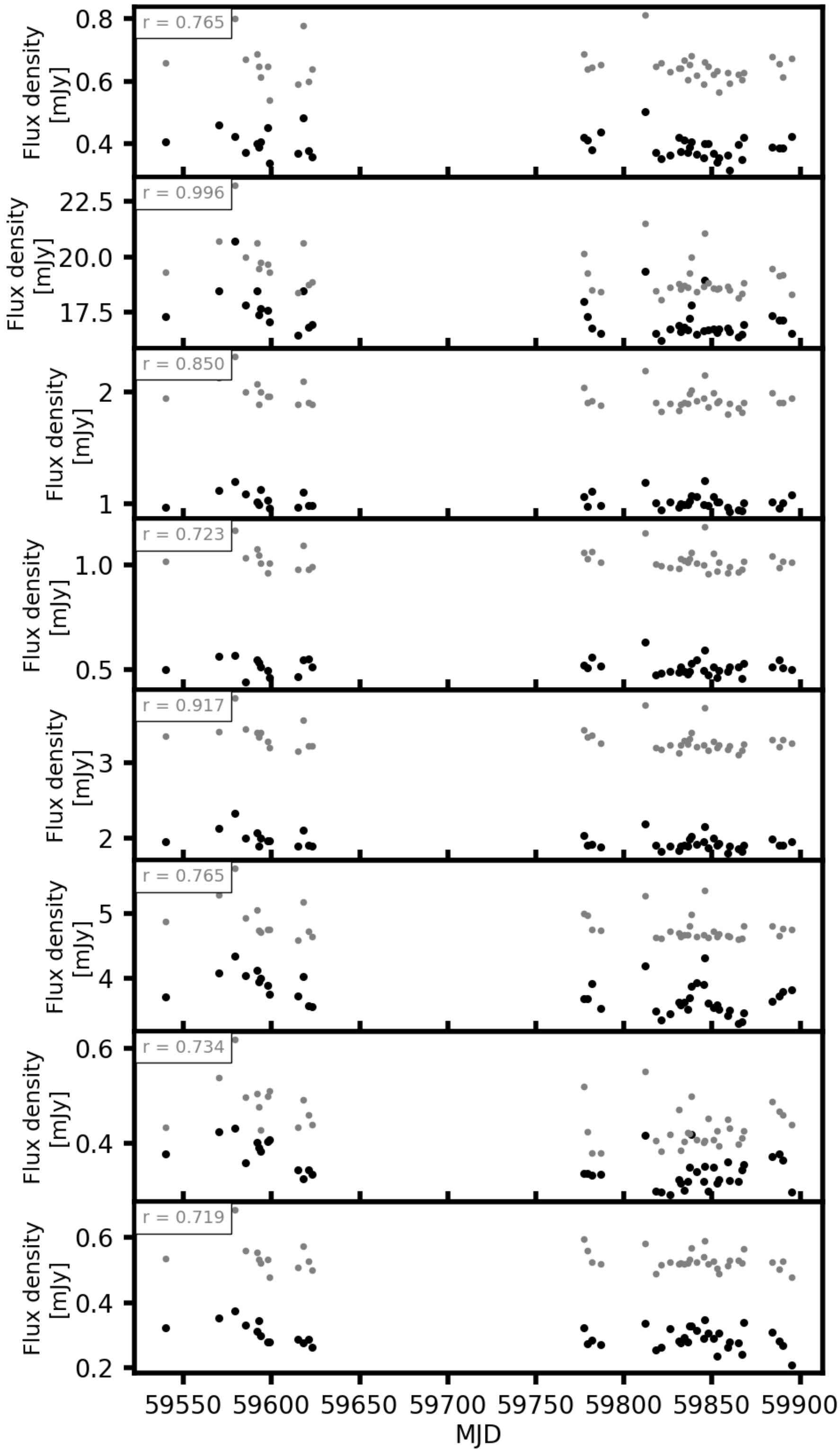

Figure 2.5: This figure shows examples of pairs pairs of highly correlated light curves, with each row displaying light curves from two distinct sources, one plotted in grey and the other in black. The light curves show flux density variations over time, measured in milliJanskys (mJy), against the Modified Julian Date (MJD). The Pearson's correlation coefficient (r), indicating the strength of the correlation between each pair of light curves, is annotated in the upper left corner of each panel.

where $\bar{F}$ denotes the median, n is the number of epochs, and F_i is the flux density of the source. The MAD is calculated as:

$$MAD = \text{median}(|F_i - \bar{F}|) \tag{2.3}$$

For more details, refer to Driessen et al. (2022). An example of corrected and uncorrected light curves is shown in Figure 3.6. After correcting the light curves, we computed new η_ν and V_ν values for comparison with the raw, uncorrected light curves from TraP

2.3.2.2 Spatial separation dependency

To address the spatial separation of the sources, we conducted a detailed analysis of their positional shifts across different epochs. Using the RA and Dec coordinates from the light curve data, we calculated the angular separation between each source's position at consecutive epochs. This was done by computing the positional shifts between each observation, measuring the angular separation in arcseconds using astrometric tools. For this analysis, the positional error for each source was determined using the method outlined in Fomalont et al. (1999). The positional uncertainty is governed by the beam size and the signal-to-noise ratio (SNR) of the observations, following the equation:

$$\sigma_{\text{pos}} \approx \frac{\theta_{\text{beam}}}{\text{SNR}} \tag{2.4}$$

where θ_{beam} represents the beam size, and SNR is the signal-to-noise ratio for each observation. This relation provides a robust estimate of positional accuracy, which we used to compare the observed positional shifts across epochs. By comparing the positional shifts with this theoretical positional error, we determined whether the observed shifts were within expected limits. The results showed that the majority of the sources had positional shifts well within the calculated error range, as indicated by the 'Within Positional Error' column. Minimal positional changes were observed, and the variability detected in the light curves of these sources is not significantly affected by positional discrepancies. This finding strengthens the conclusion that the variability is intrinsic to the sources themselves, rather than an artefact of positional errors. In addition to analysing positional shifts, we examined the variability of these sources across epochs. By comparing flux measurements, we found that the sources exhibit genuine variability. Since the positional changes are minimal and within the error range, we can confidently state that the observed variability is not correlated with spatial displacement but rather reflects true changes in the physical properties of the sources.

2.3.3 The η_ν and V_ν search

With a limited number of sources for investigation, our initial focus was on those positioned above the green line in Figure 2.4. Within this region, a meticulous manual inspection was conducted for all sources, involving a thorough examination of both light curves and radio image cut-outs, as exemplified in Andersson et al. (2022), where the detection of radio transients followed a similar procedure. To streamline this process, we developed a python script for plotting the light curve of each source within the designated area. Additionally, we utilised CARTA to load and visualize all images. During this visualisation, we employed the *RA* and *DEC* information of the sources to locate them in the radio images across different epochs. To enhance the efficiency of visualisation, we further refined our approach by creating a Python script that utilized source IDs to extract relevant information and plot image cut-outs for each source under investigation. The resulting plots were organised chronologically in a grid format, facilitating simultaneous inspection of both light curves and images. Our objective was to identify sources showing variability or flux changes over time, distinguishing them from those that remained constant. Simultaneously, we verified whether the sources, when viewed in images, behaved as point sources. This methodology aligns with approaches detailed in Andersson et al. (2023) and de Ruiter et al. (2021). Subsequently, sources that passed our selection criteria underwent further investigation to gather information about their known characteristics.

2.4 Multi-wavelength counterparts

Following the identification of potential variable and transient sources, we proceed with a comprehensive analysis to validate and characterise these candidates. This section outlines our approach to associating our identified sources through various astronomical catalogues for cross-matching, and investigating potential effects of interstellar scintillation (ISS) on observed variability.

Applying the light curve analysis and source filtering as outlined in Section 2.3.3, we were left with ~ 290 sources in UHF data. The Next step involved examining the candidate sources we had chosen as potential variables or transients, matching them with their potential counterparts. We used the radio positions of the candidates and cross-referenced them with the VizieR catalogues (Ochsenbein et al. 2000). Additionally, we used the Aladin sky atlas (Bonnarel et al. 2000) Dark Energy Survey (DES) images within Aladin and overlaying databases such as SIMBAD (Wenger et al. 2000) and GAIA database (DR3) (Gaia Collaboration et al. 2021). This approach facilitated the differentiation between stars and galaxies.

Sources identified near the radio positions were further investigated to establish a full association with our radio images. This was accomplished by considering proper motion, performing astrometry, and associating any sources falling within a 2σ positional error margin with our radio images, as demonstrated in previous work (e.g., Andersson et al. 2022). It is important to note, as discussed in Driessen et al. (2022), that there are that there are inherent challenges in performing source association between radio and optical datasets, particularly due to differences in resolution and proper motion effects. To ensure accurate source associations, we adopted a systematic approach that involved: Astrometric Corrections: We applied corrections to account for any positional discrepancies between the radio and optical data, using reference catalogues like GAIA for high-precision astrometry. Multi-Catalogue Cross-Referencing: Sources were cross-referenced against multiple catalogues (e.g., SIMBAD, VizieR) to confirm their identities and reduce the likelihood of false associations. Proper Motion Consideration: For sources with significant proper motion, we calculated the expected positional shifts and adjusted our matching criteria accordingly. Positional Uncertainty Analysis: We considered the positional uncertainties in both radio and optical datasets, ensuring that only those sources falling within a 2σ positional error margin were considered reliable matches. Our methods aimed to minimise the impact of these issues by using robust astrometric corrections and validating associations with multiple catalogues, enhancing the reliability of our source identifications.

Candidate sources with optical counterparts were further looked at in the All-Sky Automated Survey for Supernovae (ASAS-SN) (Kochanek et al. 2017), Catalina Survey (CRTS) (Drake et al. 2009), and the MeerLICHT full source catalogue via MeerZICHT (Bloemen et al. 2016). Additionally, we searched in the Transiting Exoplanet Survey Satellite (TESS) (Ricker et al. 2015), extracting the light curves of the corresponding sources for detailed analysis. Our investigation of the candidate sources extended beyond these methods of source association. Considering the concept of interstellar scintillation and its potential impact on sources identified as extragalactic radio sources, we proceeded to calculate the scintillation modulation index and timescales for our field, following the model developed by Hancock et al. (2019). This model, which essentially simulates reflective scintillation using Hα maps (RISS), was important for our study, particularly given the low frequencies involved, where sources like AGN and quasars could appear variable due to refractive scintillation, as evidenced by previous studies (e.g., Angelakis et al. 2019; de Ruiter et al. 2021; Driessen et al. 2022). We compared the predicted refractive interstellar scintillation (RISS) V_{RISS} and timescales in years as also seen in (Driessen et al. 2022) with our observed V_{ν} to further discern whether the variability observed in our interesting sources was from intrinsic factors or was influenced by RISS.

Chapter 3

Results and Analysis

In this chapter, we present the results of our analysis. We begin with the findings from the validation of the SDP images in Section 3.1 Next, we discuss the outcomes of the transient search conducted using TraP with the LADUMA SDP UHF band images in Section 3.2.1. Finally, Section 3.2.2 shows the results obtained from searching for multiwavelength counterparts, detailing the number of candidates identified along with their characteristics and properties.

3.1 LADUMA L-band data: Validation of SDP images for science

We made use of the LADUMA L-band images for the validation of the SDP images. The decision to use L-band images, despite conducting the analysis on UHF SDP images, was informed by the availability and quality of data. Specifically, we had both OxKAT and SDP images at L-band, which allowed for a robust cross-validation of the SDP imaging process. This dual dataset provided a reliable means to assess the accuracy of the SDP images by comparing them with the well-established OxKAT images.

While it is acknowledged that UHF frequencies present additional challenges, such as more pronounced direction-dependent effects due to the wider field of view, generally stronger source brightnesses, and an increased likelihood of encountering ionospheric effects, the L-band images offer a stable benchmark. The L-band, operating at a higher frequency, typically experiences less ionospheric distortion and fewer direction-dependent calibration errors. Therefore, the L-band validation provides confidence in the overall fidelity of the SDP imaging pipeline. However, we remain aware that these differences necessitate cautious interpretation, and that analysis at UHF frequencies ideally requires corresponding OxKAT data to fully account for the unique challenges presented by this band. Until UHF OxKAT data becomes available, using L-band images for validation remains the most appropriate approach under the current circumstances.

For the LADUMA L-band data, TraP identified a total of 6780 candidate sources in the OxKAT images and 5013 candidate sources in the SDP images. To compare the results meaningfully, we first matched the search radii of both TraP runs, as the OxKAT images have a different radius than the SDP images (see Section 2.2.3 and Figure 2.3). We plotted the two datasets in the η_ν and V_ν space as shown in Figure 3.1. After cross-matching the two datasets, we found that 4529 of the 6780 OxKAT candidate sources were also detected in the SDP dataset from

TraP, representing approximately 67% of the total OxKAT source candidates. This left 2251 candidates detected only in the OxKAT images. Conversely, there were 484 candidates detected only in the SDP images, not found in OxKAT, representing 9.7% of the total SDP detections.

To understand the nature of the unmatched OxKAT candidates, we manually inspected the light curves of the 2251 unmatched OxKAT candidates and cross-matched them with sources in SIMBAD and VizieR. The primary goal here was to ascertain whether these unmatched OxKAT sources were potential transients or variable sources that might not have been detected in the SDP images due to the specific characteristics of the imaging process. By cross-matching with optical surveys, we could determine if these radio sources had corresponding optical counterparts that were also variable, thus strengthening the case for their identification as true astrophysical sources rather than artefacts or noise. Of these 2251 unmatched sources, 219 candidates were identified as potential transients or variable sources, based on both their radio light curves and the presence of variable optical counterparts. Based on these findings, we calculated the common sources to determine how well SDP recovers sources detected by OxKAT. The common sources was approximately:

$$\text{Common sources (Adjusted)} = \frac{\text{Matched OxKAT and SDP Candidates}}{\text{Total OxKAT Candidates}} = \frac{4529}{6780} \approx 67\% \tag{3.1}$$

Next, we applied the filtering criteria outlined in Section 2.3 independently to both datasets, focusing on sources with η_ν above 8 and V_ν above 0.09. After filtering, 98 OxKAT sources and 63 SDP sources passed the thresholds. Of the 98 filtered OxKAT sources, 55 (approximately 57%) were also found in the filtered SDP dataset. We then manually inspected the 43 OxKAT candidates that were not found in the SDP subset, finding that 15 of these candidates are likely to be true transients or variables based on their optical counterparts and light curves, while the remaining 28 appear to be artefacts or non-significant variations. This resulted in an approximate common sources of 57% after filtering and manual inspection.

Stage	OxKAT	SDP	Matched	Unmatched OxKAT	Unmatched SDP	Potential Variables or Transients	Common sources (%)
Initial Candidate Sources	6780	5013	4529 (67%)	2251 (33.2%)	484 (9.7%)	219	~67
Filtered Candidates After Inspection	98	63	55 (57%)	43	8	15	~57

Table 3.1: Summary of significant values and relationships between OxKAT and SDP candidate sources.

Figure 3.1 shows all the sources in black, with green indicating sources that match in both datasets and red indicating sources that passed our filtering process and match in both datasets. Table 3.1 summarises these findings.

In Figure 3.2 we plot 8 of the 15 light curves of the potential transients or variables that were unmatched. To understand further the nature of the light curves for matching sources that also pass our filtering process, we plot 2 typical light curves seen in Figure 3.3 and find that the OxKAT light curves always have a much higher fluxes compared to the SDP light curves as seen in Figure 3.3. This is expected as the OxKAT images are beam corrected while the SDP images are not. We normalised the light curves to the brightest detection and observed that the trends in the OxKAT reduced images are consistent with those in the SDP images as seen in Figure 3.4. This consistency suggests that the information obtained from the SDP images closely matches that from the OxKAT reduced images. However, it is important to consider whether any candidates detected in the SDP image but not in the OxKAT are genuine transients or false positives, given the quality differences between the two sets of images.

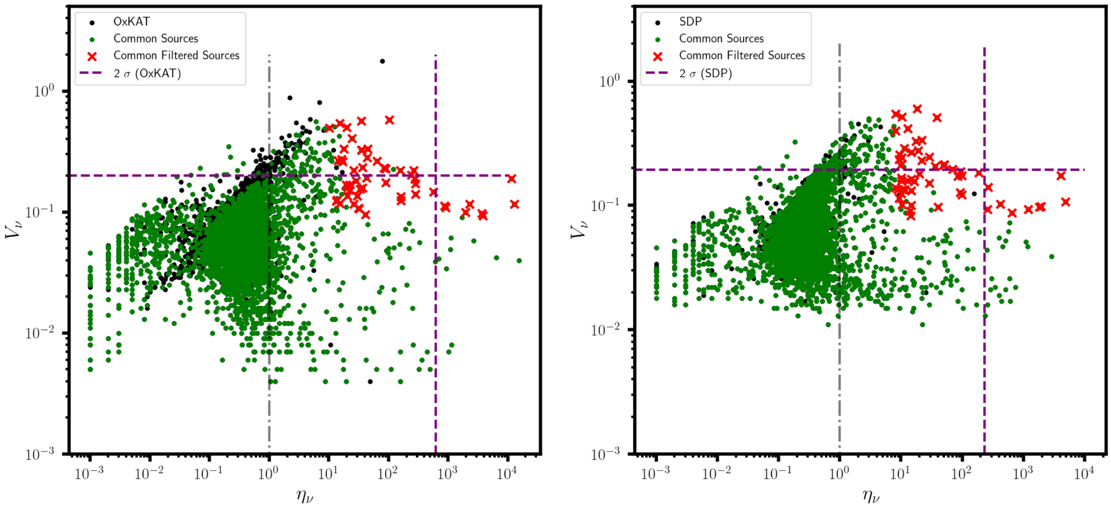

Figure 3.1: The η_ν and V_ν space of the OxKAT (on the left) and SDP (on the right) being plotted. The full TraP outputs are seen in black, while the cross matched sources are seen in green and the red makes sources are sources that passed our filtering process. The purple dashed lines marks the 2σ limits for the filtering process.

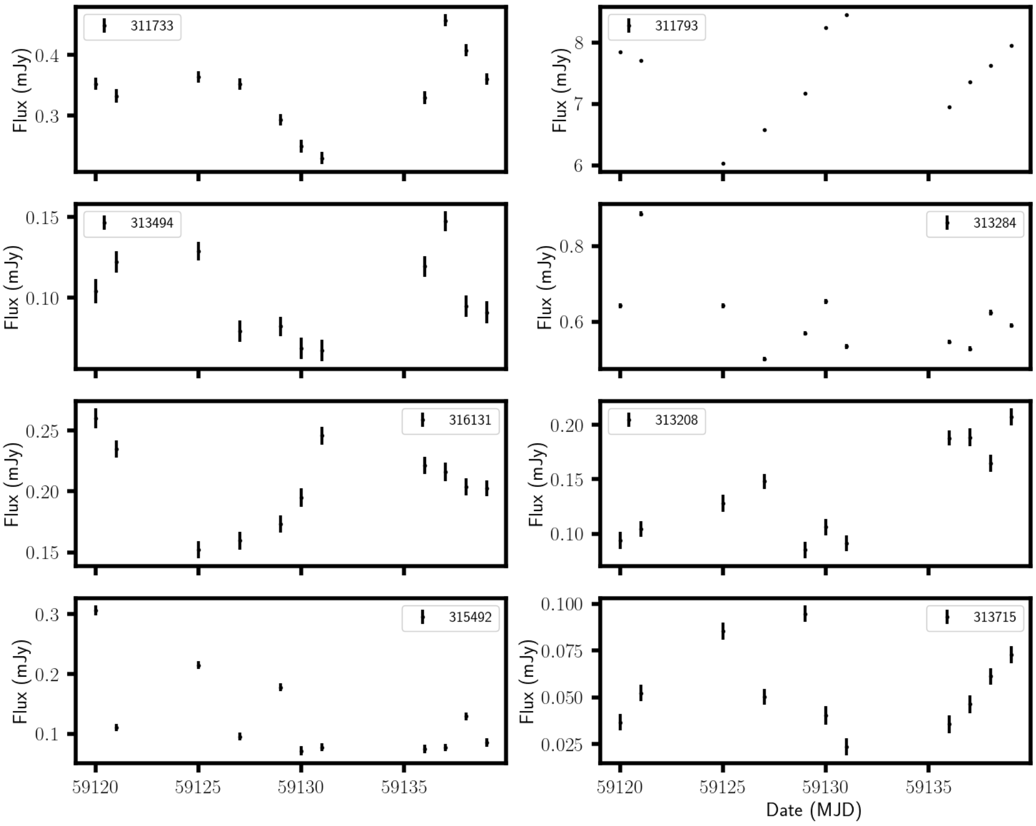

Figure 3.2: Light curves 8 sources from the OxKAT images that are seen to be variable sources, when inspecting the light curves as well as cross matching source coordinates with SIMBAD. These sources constitute a subset of the 15 unmatched sources located within our filtered region.

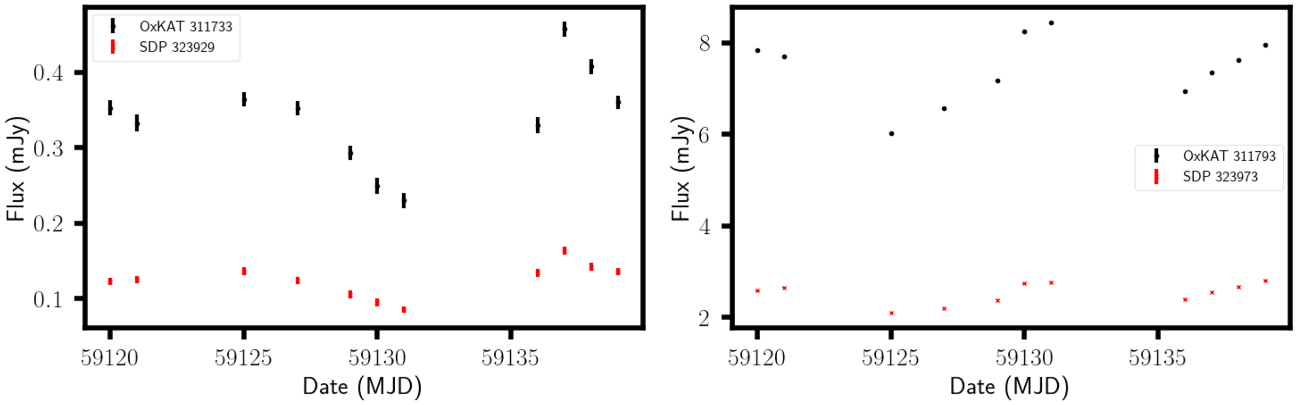

Figure 3.3: An example of two light curves of source candidates found in both SDP and OxKAT images of the same source in both.

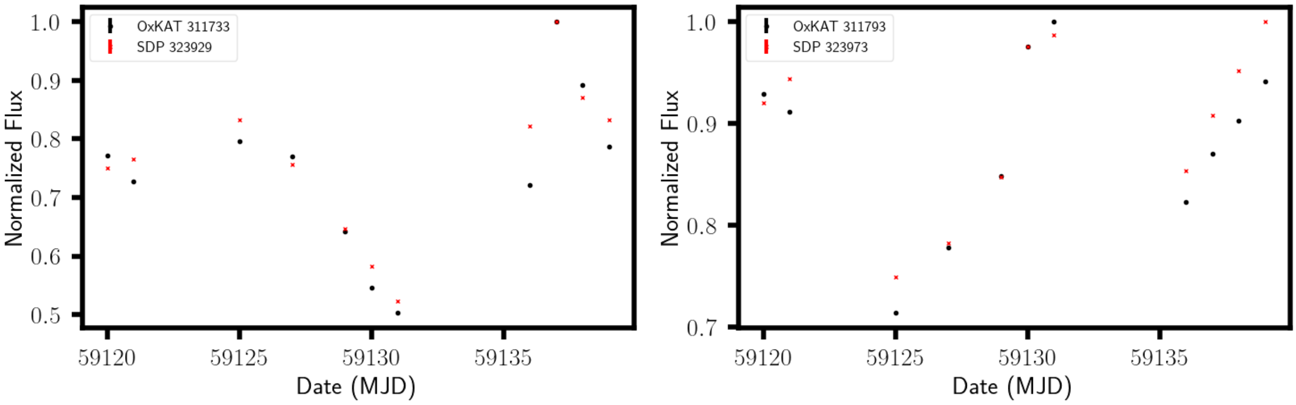

Figure 3.4: Normalised light curves are shown for two source candidates visible in both the SDP and OxKAT images. The OxKAT light curves exhibit higher flux density compared to the SDP light curves. Each curve is normalised to its peak flux, as presented in Figure 3.3.

Beam-corrected images account for the primary beam response of the telescope, which is crucial for obtaining accurate brightness measurements. The primary beam correction adjusts the observed flux densities to reflect their intrinsic values, compensating for the varying sensitivity across the field of view. Without this correction, the measured flux densities would be lower, especially towards the edges of the field, where the primary beam sensitivity drops. The large difference in flux densities, particularly in sources located towards the outer regions of the field, could be attributed to the fact that the extraction radii for both the OxKAT and SDP images (39.4 arcminutes and 39.3 arcminutes, respectively) extend beyond the half-power beamwidth of MeerKAT, which is 30.5 arcminutes. In these regions, the sensitivity of the telescope drops significantly, and primary beam corrections become more aggressive, leading to inflated flux values. This explains the factor of 3 or more difference in flux observed between the OxKAT and SDP light curves, as seen in Figure 3.3. Figure 3.5 illustrates this by comparing the flux distributions of sources in two sets of images. The red histogram represents the mean fluxes from the SDP images, while the blue histogram represents those from the OxKAT-reduced images. The primary beam correction in the OxKAT images results in higher flux densities, as seen in the blue histogram, reflecting the correction of apparent values to intrinsic ones particularly for sources beyond the half-power beamwidth.

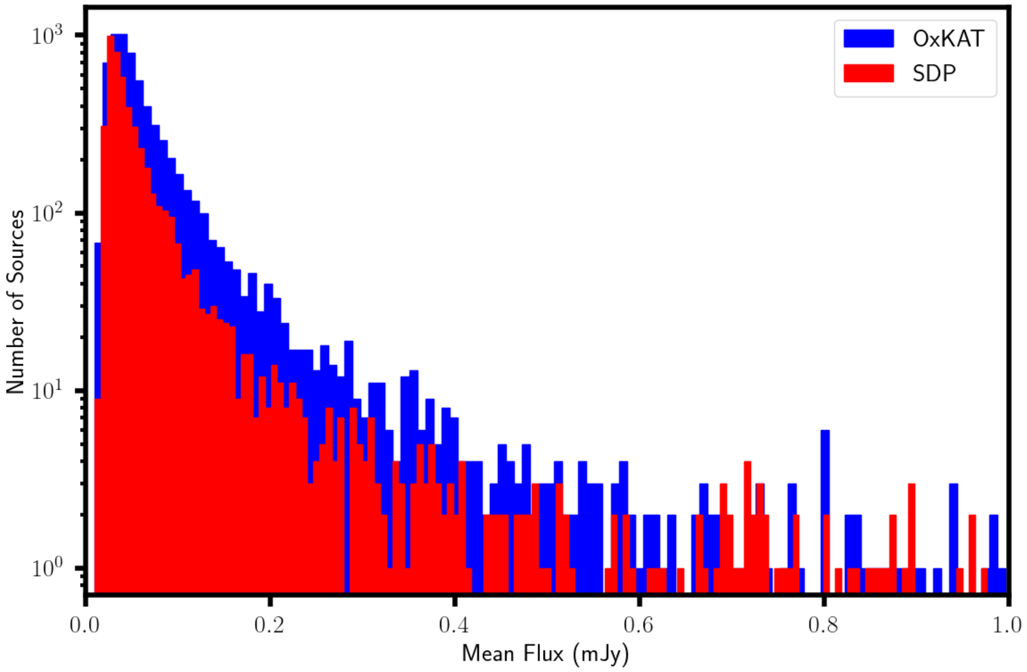

Figure 3.5: This histogram compares the flux distributions obtained from the two sets of images, the SDP and OxKAT. The OxKAT images have been beam corrected, while the SDP images remain uncorrected. Each bin in the histogram represents the number of sources within a specified flux range, with each bin width set to 0.01 mJy

3.2 LADUMA UHF-band data: Transient analysis

3.2.1 Light curve analysis

Here we show the results obtained from analysing correlated light curves. Figure 2.5 displays a number light curves with a correlation coefficient $r > 0.7$. Addressing these correlations was crucial, as sources previously identified as variable or transient candidates were found to be consistent with constant sources after correction, as shown in Figure 3.6.

Some sources exhibit potential long-term variability, warranting further study. Additionally, there was a significant $\sim 10\%$ reduction in flux. The observed $\sim 10\%$ reduction in flux suggests that the original flux measurements were likely affected by unmodeled instrumental or propagation effects, rather than an inherent inaccuracy in MeerKAT's flux calibration. It is important to note that MeerKAT's flux scale accuracy is generally better than 10%, as demonstrated by transfer calibration techniques and cross-matching with compact sources observed by the VLA, which achieve accuracies at the percent level. The $\sim 10\%$ flux discrepancy mentioned aligns with previously reported calibration errors by Rhodes et al. (2020) and MAGIC Collaboration et al. (2019). However, attributing this entirely to a fundamental calibration issue would be misleading. The offsets are more likely due to factors such as unmodeled instrumental effects or atmospheric propagation anomalies, rather than the intrinsic accuracy of MeerKAT's calibration. Using the corrected fluxes, new variability parameters η_ν and V_ν were calculated with Equations 1.10 and 1.11. The updated variability parameters plot shows that sources with high η_ν and V_ν values are more affected by the correction than those with low values. When plotted against flux density, we find that sources with flux density greater than ~ 10 mJy tend to be more affects as opposed to low flux sources. It is evident that η_ν is more affected compared to V_ν. This is expected, as η_ν measures the normalized excess variance of a light curve,

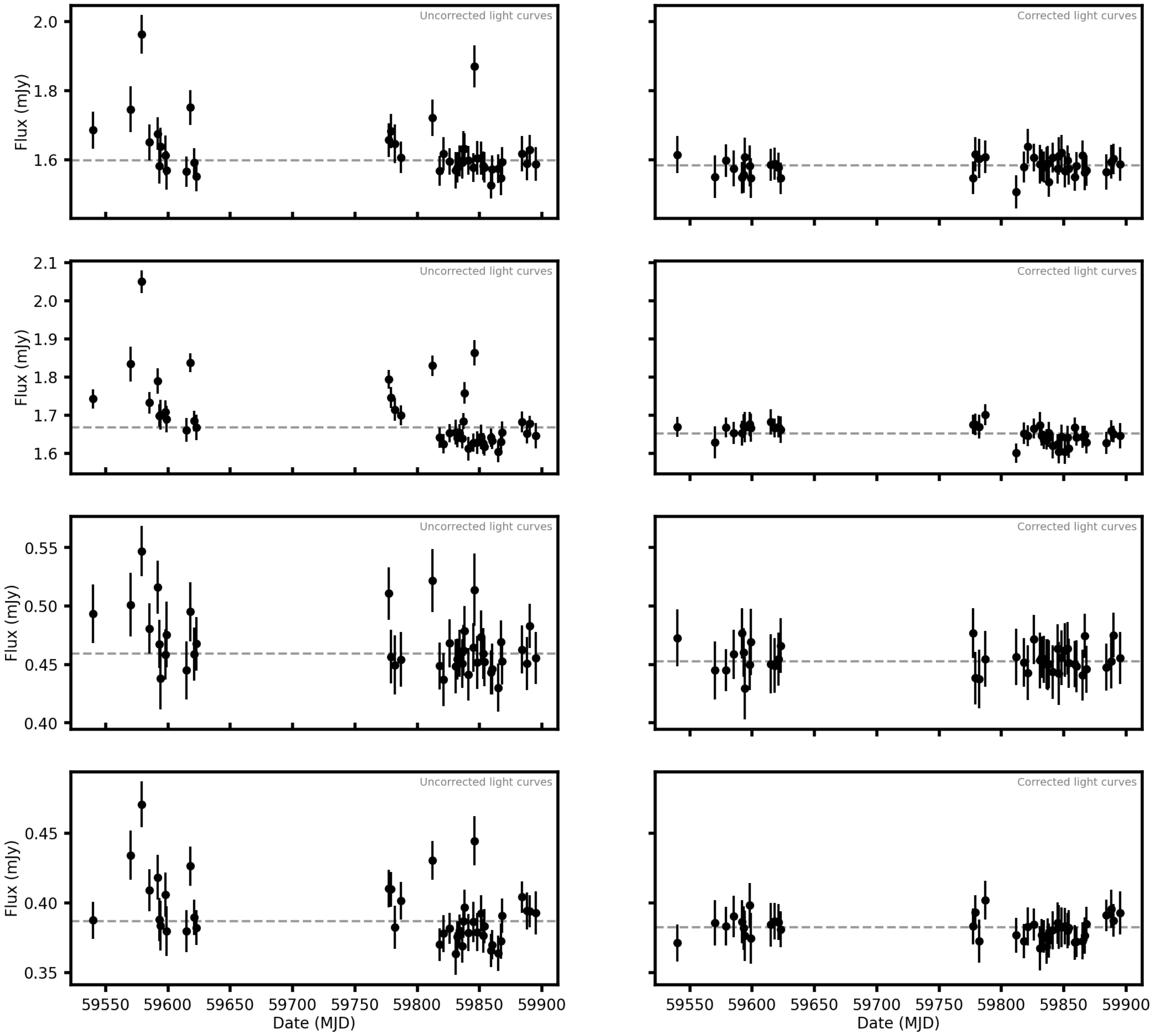

Figure 3.6: Corrected light curves for point sources with a signal-to-noise ratio greater than 2 are shown before and after correction. Each row represents the same source, with the left column showing the light curve before correction and the right column after correction. The gray dashed line indicates the median flux.

quantifying the variability in a source's flux compared to its average flux, as shown in Figure 3.7.

3.2.2 Transient candidates

In this section present a list of candidate sources identified in the transient and variable searches section of this thesis. The work done by Andersson et al. (2023) (see their Figure 4) involving citizen science has shown that transients and variables are found on wider range of η_ν and V_ν values than generally expected. The purpose of this work is not to perform an extensive search for all variables in this field but to demonstrate the use of SARAO SDP images for commensal transient searches. Eight selected candidates exhibit variable and transient behaviour in the η_ν and V_ν parameter space, as shown in Figure 3.8. Five candidates, SRC207895, SRC207950, SRC211766, SRC210683, and SRC209337 are below the filtering limits but within the new search region, indicating they are likely variable sources

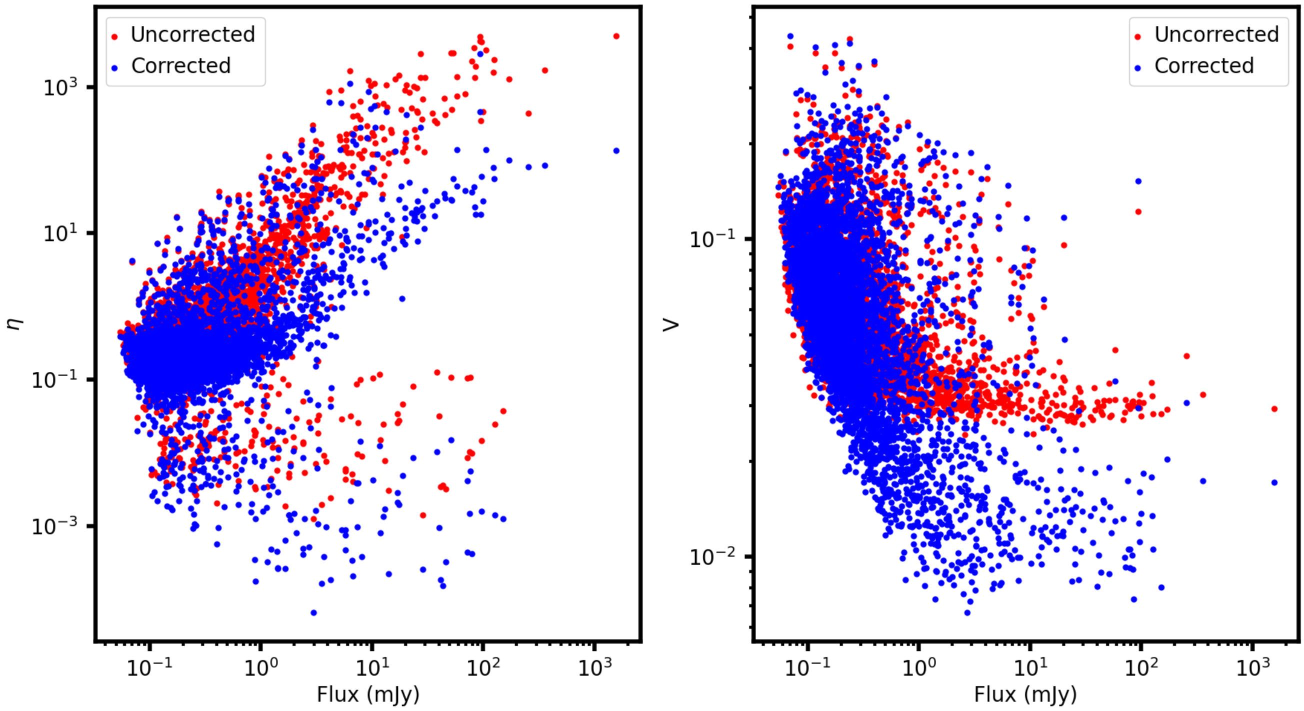

Figure 3.7: Comparison of the the variability parameters, before and after the light curve correlation correction (Correction here refers to work done on the correlated sources and removal of such sources the removal of all resolved sources as we only cared for unresolved sources) was done. This plot only shows unresolved sources.

with intrinsically low flux densities. Although SRC209991 is above the η_ν limit, it behaves similarly to the other five candidates. The remaining two sources, SRC210499 and SRC213653, are above the V_ν limit but below the η_ν limit. SRC210499 has a high η_ν value, suggesting it is a potential variable source. SRC213653, with relatively high η_ν and V_ν values, is an outlier and likely a transient source, consistent with findings by Andersson et al. (2022) and Rowlinson et al. (2022). All these sources are unresolved point sources. Table 3.2 shows the summary of the radio characteristics of the 8 selected candidates from TraP.

Source ID	RA hh:mm:ss.ss	DEC –dd:mm:ss.s	η_ν	V_ν	Flux_min (mJy)	Flux_max (mJy)
SRC211766	03:28:26.50	–28:19:20.7	50.611	0.209	1.018 ± 0.053	2.259 ± 0.043
SRC213653	03:28:49.69	–27:18:55.7	32.951	1.372	0.014 ± 0.053	1.041 ± 0.043
SRC210683	03:31:07.60	–28:31:46.7	59.020	0.191	0.844 ± 0.026	1.823 ± 0.027
SRC210499	03:31:27.10	–27:44:09.9	8.13	0.406	0.032 ± 0.018	0.275 ± 0.019
SRC209991	03:32:11.60	–27:37:26.3	886.356	0.176	3.120 ± 0.025	5.992 ± 0.025
SRC209337	03:33:03.70	–27:36:11.3	30.398	0.224	0.287 ± 0.017	0.740 ± 0.021
SRC207950	03:35:00.80	–28:55:19.6	300.845	0.183	2.180 ± 0.042	4.108 ± 0.032
SRC207895	03:35:04.80	–27:41:34.9	61.087	0.212	0.560 ± 0.029	1.414 ± 0.026

Table 3.2: Summary of the 8 selected candidates characteristics including their Source ID, RA, DEC, variability indices (η_ν and V_ν), and the minimum and maximum flux values observed. The flux values include their respective uncertainties. This table highlights the variability and flux range of each source, sorted by RA in ascending order.

We also plot a sky-radio map of the field in Figure 3.9, showing the positions of the sources in one epoch. This helps determine if the observed variability is intrinsic or due to systematics, such as sources being further from the center

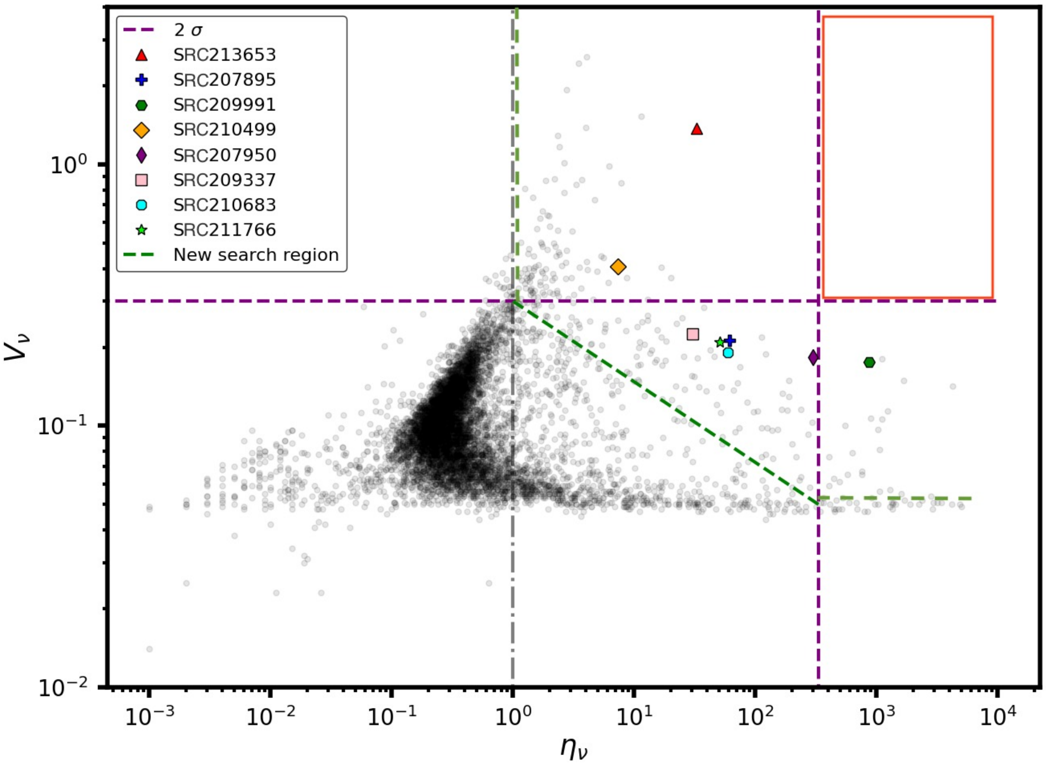

Figure 3.8: The η_ν and V_ν parameter space showing eight interesting sources exhibiting variable or transient characteristics. Filtering limits of 0.3 and 334.12, representing the 2σ limit from the mean of η_ν and V_ν, respectively, are indicated.

of the MeerKAT beam, where sensitivity drops. All but one source are reasonably close to the center, supporting the validity of their variability. SRC213653, farther from the beam center, still exhibits true variability based on its light curve (Figure 4.2) and radio image cutout (Figure 4.3). The same shapes and colors from Figure 3.8 are used for source identification on Figure 3.9.

We examine the candidate sources in detail by analysing their light curves (Figure 3.10) and inspecting the 60 arc-second cutout images of their radio emissions. These cutout images, shown in Appendix A, are created using a python script, with the source of interest at the center. The images are arranged chronologically to align with the light curves, facilitating simultaneous analysis. The light curves for each source are plotted and presented in Figure 3.10.

3.3 LADUMA UHF-band data: Source classification

3.3.1 Multi-wavelength counterparts

We present the multi-wavelength counterparts of our interesting candidate sources as described in Section 2.4. We searched for additional radio measurements in various surveys, including ATLAS at a frequency range of 0.7-1.5 GHz (Norris et al. 2006), NVSS at a frequency of 1.4 GHz (Condon et al. 1998) VLASS at a frequency range of 2-4 GHz

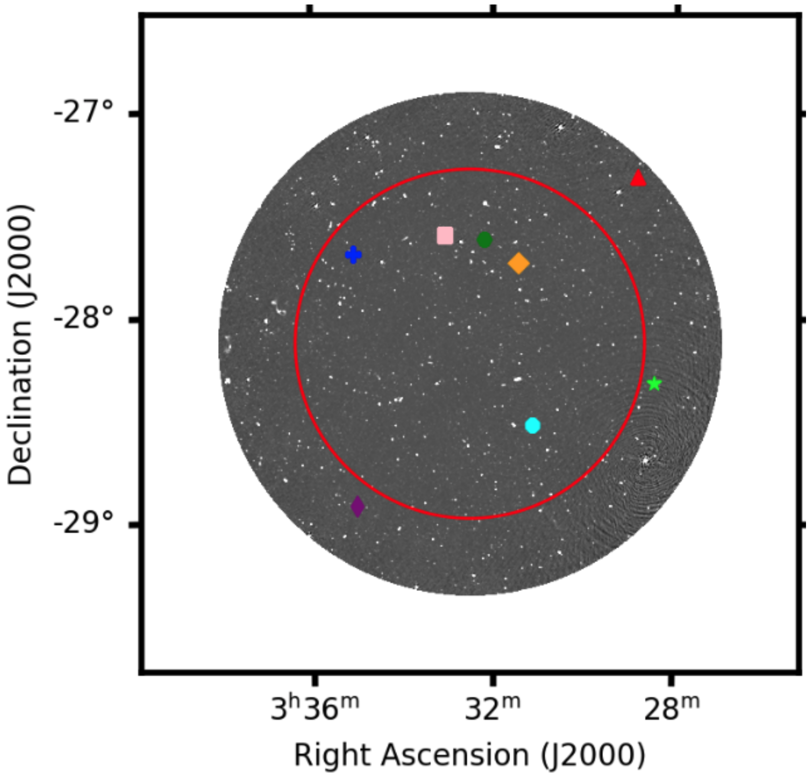

Figure 3.9: Radio sky map overlaid with candidate sources positions. The same shapes and colours used in Figure 3.8 legend are also used here for indicative purposes. SRC213653 is closer to the beam edge.

(Lacy et al. 2020) and RACS at a frequency range of 0.7-1.5 (Hale et al. 2021). It should be noted that the VLASS peak brightness measurements are at significantly higher frequencies (2-4 GHz) compared to the MeerKAT UHF band (0.58-1.015 GHz). This frequency difference can result in variability in observed flux densities due to spectral index effects, which should be considered when comparing measurements from these surveys. Additionally, we provide the classification of these sources using tools developed by Stewart et al. (2018). Classification is performed by plotting the radio and optical fluxes of the sources and comparing them to the plot introduced by Stewart et al. (2018) (Figure 3.11). Stewart et al. (2018) investigated various astronomical objects including X-ray binaries, optical and radio quasars, stars, CVs, radio pulsars, GRBs, and supernovae, by analyzing their fluxes in r and V band magnitudes. We use the g and r magnitudes from the Dark Energy Survey (DES DR3) to plot our sources against their corresponding radio fluxes and determine which population they belong to.

3.3.2 SRC207895

SRC207895 is located at RA 03:35:4.8 and DEC −27:41:34.9. The radio light curve shown in Figure 3.10 shows clear variability between a range of 0.56 − 1.41 mJy, with a peak flux of 1.414 ± 0.026 mJy. The light curve includes multiple detections and aligns with the radio image cutout in Figure A.3. ATLAS reported a peak flux of 0.73 mJy with 20 percent uncertainties for ATCDFS J033504.75–274135.9 S662. Additionally, VLASS detected a source, VLASS1QLCIR J033504.77–274134.2, with a peak flux of 1.399 ± 0.131 mJy. No objects were found in NVSS and RACS surveys for this source.

ATCDFS J033504.75-274135.9 S662, is a known AGN (Norris et al. 2006). It is found 1.13 arcseconds away from SRC207895, making it the most probable association for the radio emission from SRC207895. Optical observa-

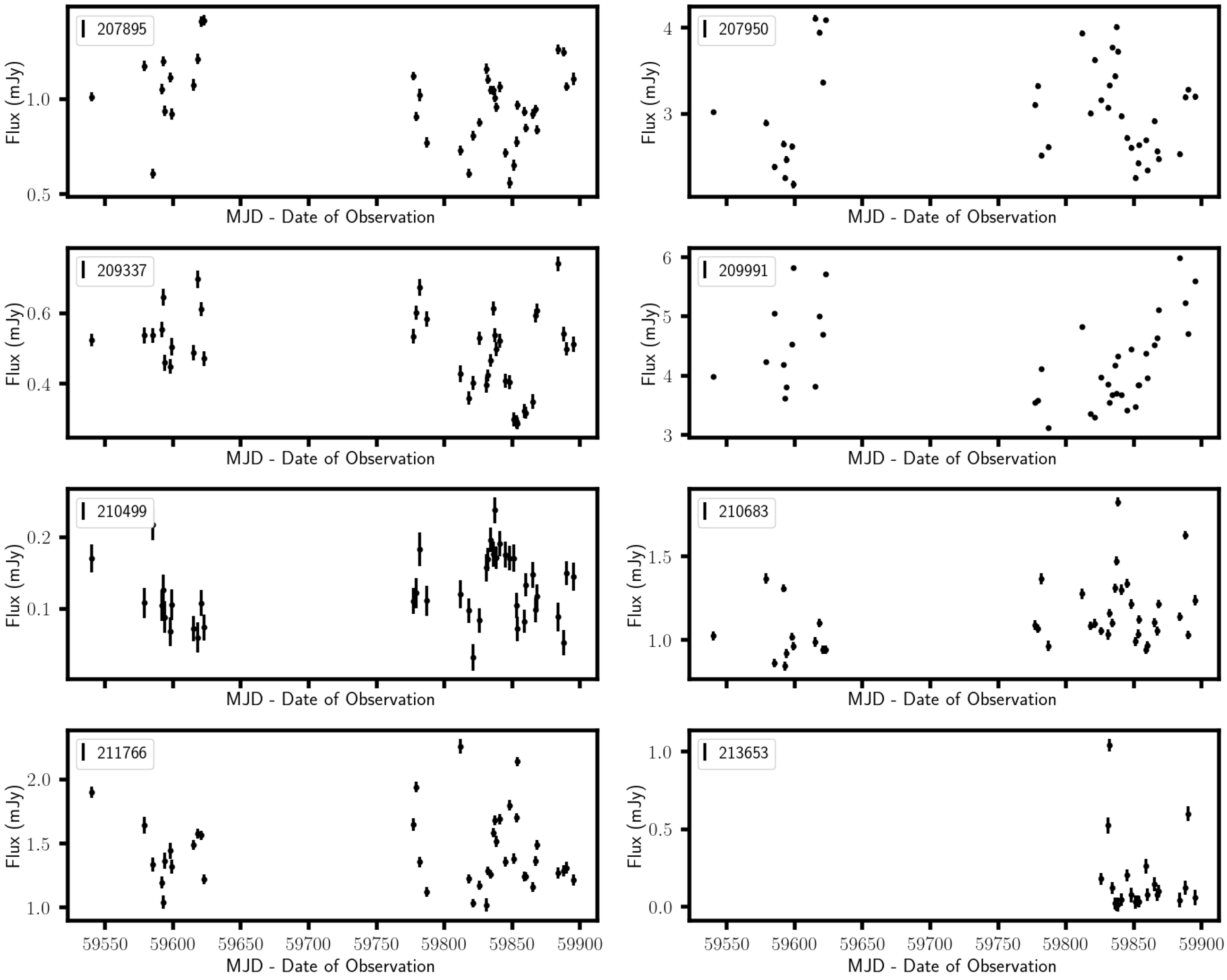

Figure 3.10: Light curves from TraP of the eight candidate sources. The flux is plotted in mJy along with the observation date in MJD. The brightest source, SRC209991, reaches a flux of 5.992 ± 0.025 mJy, and the faintest source, SRC210499, has a maximum flux of 0.275 ± 0.019 mJy.

tions from Pan-STARRS provided i and z magnitudes with an optical flux of 0.0272 mJy (Chambers et al. 2016). Measurements from DES (Norris et al. 2006) show magnitudes in the g, r, and i bands as shown in Table 3.4

SRC207895 exceeds the FIRST detection limit and lies between the SDSS limits (Figure 3.11). It is positioned where optically-selected quasars are abundant and GRBs are sparse. The constant ratios (grey dashed diagonal lines) suggest consistency with an AGN. Therefore, we classify SRC207895 as an AGN, consistent with previous classifications of its counterpart ATCDFS J033504.75-274135.9 S662 (Norris et al. 2006).

3.3.3 SRC207950

SRC207950 is located at RA 03:35:00.8 and DEC −28:55:19.6. The radio light curve shown in Figure 3.10 shows clear variability between a range of 2.18 - 4.10 mJy, with a peak flux of 4.108 ± 0.032 mJy. The light curve includes multiple detections and aligns with the radio image cutout in Figure A.3. ATLAS reported a flux density of 3.16 mJy

Source ID	MeerKAT Flux range (mJy) 0.816 GHz	ATLAS Peak flux (mJy) 0.7-1.5 GHz	NVSS Peak flux (mJy) 1.4 GHz	VLASS Peak flux (mJy) 2-4 GHz	RACS Peak flux (mJy) 0.7-1.5 GHz
SRC207895	0.560 - 1.414	ATCDFS J033504.75-274135.9 0.73±0.2	No object found	VLASS1QLCIR J033504.77-274134.2 1.399±0.131	No object found
SRC207950	2.180 - 4.108	ATCDFS J033500.80-285519.6 3.16±0.2	NVSS 033501-285528 3.0±0.5	VLASS1QLCIR J033500.80-285518.9 2.180±0.109	RACS_0345-31A_5785 3.001±0.279
SRC211766	1.018 - 2.259	ATCDFS J032826.50-281920.5 0.93±0.2	No object found	VLASS1QLCIR J032826.48-281920.7 0.894±0.002	No object found
SRC210683	0.844 - 1.823	ATCDFS J033107.60-283146.4 1.26 ±0.2	NVSS 033106-283138 2.3±0.5	VLASS1QLCIR J033107.61-283146.2 4.746±0.109	No object found
SRC209337	0.287- 0.740	ATCDFS J033303.74-273610.9 0.28±0.2	No object found	No object found	No object found
SRC209991	3.120 - 5.992	ATCDFS J033211.65-273726.3 3.78 ± 0.2	NVSS J033211.3-273727 4.50 ± 0.5	VLASS1QLCIR J033211.64-273725.8 10.817 ± 0.122	RACS_0337-25A_5118 3.524 ± 0.241
SRC210499	0.032 - 0.275	ATCDFS J033127.51-274440.1 0.15 ± 0.2	No object found	No object found	No object found
SRC213653	0.014 - 1.041	No object found	No object found	No object found	No object found

Table 3.3: Comparison of flux measurements across various radio surveys for the 8 selected candidates. The table lists the flux range observed by MeerKAT at 0.816 GHz, and peak flux values from the ATLAS survey (0.7-1.5 GHz), NVSS survey (1.4 GHz), VLASS survey (2-4 GHz), and RACS survey (0.7-1.5 GHz) where available. The uncertainties for each measurement are also provided.

with 20 percent uncertainties for ATCDFS J033500.80–285519.6 (S659). NVSS also reported a flux measurement of 3.0 ± 0.5 mJy, consistent with MeerKAT's measurements. Additionally, VLASS detected a source, VLASS1QLCIR J033500.80-285518.9, located 0.7 arcseconds away, with a reported peak flux of 2.180 ± 0.109 mJy.

In the optical band, DES reports g, r, and i magnitudes (Table 3.4). ATCDFS J033500.80–285519.6 (S659) is a known AGN (Norris et al. 2006). This source is located 0.02 arcseconds away from SRC207950, falling well within the MeerKAT's 2σ positional uncertainty. No measurements were found in the GAIA catalog. No objects were found in the Pan-STARRS catalog for this source. No X-ray counterparts were found for SRC207950. In the infrared, a source J033500.89-285519.3, located 1.27 arcseconds away, falls within the 2σ positional uncertainty and is associated with our source.

SRC207950, our second brightest source, resides above the FIRST detection limit but below the 95 percent completeness limit (Figure 3.11). It occupies a region sparsely populated by radio pulsars. The diagonal lines on the radio-optical ratio plot suggest consistency with a quasar/AGN. Despite its radio brightness, SRC207950 is faint in the optical, residing below the 95 percent completeness limit. SRC207950 was originally classified as an AGN, as

Source ID	MeerKAT Classification	PanSTARRS Peak flux (mJy)	DES			X-ray	Infrared Wise
			g	*r*	*i*		
SRC207895	AGN	PSO J053.7699-27.6930 0.0272 ±0.0008	23.155 ±0.071	22.007 ±0.032	21.080 ±0.026	No object found	J033504.78-274134.7
SRC207950	Further Investigation	No object found	24.496 ±0.199	24.122 ±0.180	23.212 ±0.148	No object found	J033500.89-285519.3
SRC211766	AGN	PSO J052.110-28.3224 0.2758±0.0018	19.740 ±0.011	18.291 ± 0.004	17.793 ± 0.005	No object found	J032826.51-281920.6
SRC210683	AGN	PSO J052.7817-28.5297 no measurents	26.151 ± 0.870	24.044 ± 0.157	22.646±0.084	4XMM J033107.6-283145 4.418e-14±0.906e-14 mW/m^2	J033107.62-283146.6
SRC209337	Quasar	PSO J053.2656-27.603 0.0849 ± 0.0024	20.578 ± 0.008	20.162 ± 0.007	19.740 ± 0.001	4XMM J033303.7-273610 3.218e-15±1.020e-15 mW/m^2	J033303.73-273611.2
SRC209991	Quasar	PSO J053.048-26.264 0.812 ± 0.001	18.980 ± 0.002	18.797 ± 0.002	18.615 ± 0.003	LSXPS J033211.8-273724 7.9 (± 0.9) x 10^{-3} ct	J033211.66-273726.3
SRC210499	Further Investigation	PSO J052.8627-27.7363 0.0131 ± 0.0004	23.400 ± 0.053	23.322± 0.064	22.922 ± 0.080	No object found	J033126.13-274356.7
SRC213653	Low Mass Star	No object found	15.582±0.001	15.271±0.001	14.229±0.001	MMSL2 J032848.9-271903	J032849.02-271900.4

Table 3.4: The table the MeerKAT classification, PanSTARRS peak flux, DES magnitudes in g, r, and i bands, X-ray counterpart information, and infrared counterpart from the Wise catalog for the 8 selected candidates

detailed by Norris et al. (2006), who included it in the ATLAS survey. This survey identified active galactic nuclei (AGN) based on multi-wavelength data, using several discriminants such as radio-IR correlations, spectral indices, and morphology. In particular, ATLAS identified objects whose radio emission was stronger than that expected from star-forming galaxies, suggesting AGN activity. ATCDFS J033500.80–285519.6, associated with SRC207950, likely met these criteria, given its high radio flux and faint optical emission, a hallmark of AGN behaviour. The source also fell into the category of 'buried AGN,' where optical properties might resemble star-forming galaxies, but radio emission is dominated by AGN. Further investigation is needed to classify SRC207950 as either an AGN or a pulsar, despite its previous classification as an AGN.

3.3.4 SRC211766

SRC211766 is located at RA 03:28:26.5 and DEC −28:19:20.7. The radio light curve shown in Figure 3.10 shows clear variability between a range of 1.02 - 2.26 mJy, with a peak flux of 2.259 ± 0.043 mJy. SRC211766 is the third brightest candidate. The light curve starts with a high flux, drops to its lowest during the first season (in this context, 'season' refers to a specific period during which MeerKAT observes distinct regions of the sky within the LADUMA field), and then rapidly increases in the second season, reaching its peak before decreasing in the last two epochs (Figure 3.10). The radio cutout images in Figure A.8 confirm these observations. ATLAS reports a source located 0.318 arcseconds from MeerKAT's position, with a peak flux of 0.93 mJy and an integrated flux of 1.2 mJy, with 20 percent uncertainties (Norris et al. 2006) at 1.4 GHz. Additionally, VLASS coverage reports a peak flux of 0.894 mJy for the associated source VLASS1QLCIR J032826.48–281920.7. No NVSS coverage was found for SRC211766.

A known AGN, 2MASS J03282657–2819205, was found 0.96 arcseconds from MeerKAT's position of SRC211766, falling within the 2σ positional uncertainty. Additionally, the source coincides with the Pan-STARRS source PSO J052.110-28.3224, with an optical flux of 0.2758 ± 0.0018 mJy (Flewelling 2018). No GAIA counterpart was identified. DES reports g, i, and r magnitudes (Table 3.4). No X-ray counterparts were found. Near-infrared counterparts were identified in both WISE and 2MASS.

SRC211766 lies within SDSS limits, above the FIRST detection limits, and in a region populated by optical quasars, X-rays, stellar events, and supernovae (Figure 3.11). Constant ratios along diagonal dashed gray lines suggest SRC211766 is likely an AGN. We classify it accordingly, consistent with the associated optical source 2MASS J03282657–2819205 being an AGN.

3.3.5 SRC210683

SRC210683, located at RA 03:31:07.6 and DEC –28:31:46.7, exhibits variability in its radio emissions, with a flux range of 0.84 - 1.82 mJy. The peak flux is 1.823 ± 0.027 mJy, with the light curve showing distinct variations (Figure 3.10) and confirmed by the radio image cutouts in Figure A.6. ATLAS reports a peak flux of 1.26 mJy (Norris et al. 2006), while VLASS measures a peak flux of 4.904 ± 0.207 mJy (Bruzewski et al. 2021). NVSS observations record a flux of 2.3 ± 0.5 mJy.

SRC210683 is associated with a known AGN ATCDFS J033107.60–283146.4 is confirmed, located within 0.32 arcseconds of MeerKAT's position. Pan-STARRS also identifies its alignment with PSO J052.7817-28.5297. DES reports optical measurements (Table 3.4). In the X-ray band, 4XMM J033107.6-283145 exhibits a flux of 4.418e-14 ± 0.906e-14 mW/m^2 (Webb et al. 2020), and the infrared counterpart J033107.62-283146.6 is documented (Cutri et al. 2012).

SRC210683 is positioned within SDSS limits and above the FIRST detection limit and resides in a region populated by optical quasars, X-ray binaries, and supernovae (Figure 3.11). Consistent ratios support its classification as an AGN, aligning with prior classifications (Norris et al. 2006).

3.3.6 SRC209337

SRC209337 is located at RA 03:33:03.7 and DEC –27:36:11.3. The radio light curve in Figure 3.10 shows clear radio variability with a peak flux of 0.740 ± 0.021 mJy, within a flux range of 0.287 - 0.740 mJy (Figure 3.10) across all 43 epochs as seen in A.4. ATLAS reports a peak flux of 0.28±0.2 mJy within the frequency range of 0.7 - 1.5 GHz, while no VLASS or NVSS associations were identified.

A known quasar, ATCDFS9 J033303.73–273611.4, is positioned 0.48 arcseconds from SRC209337, falling within the 2σ positional uncertainty. Pan-STARRS source PSO J053.2656-27.6031 registers an optical flux of 0.0849 ± 0.0024 mJy (Flewelling 2018). DES provides measurements in g, r, and i bands (Abbott et al. 2022). X-ray observations from 4XMM-DR9 record a mean flux of 3.218e-15 ± 1.020e-15 mW/m^2 (Webb et al. 2020). The source is cataloged in GAIA DR3 with a g magnitude of 20.958 ± 0.012 (Gaia Collaboration et al. 2020), consistent with DES measurements.

SRC209337 is positioned below the FIRST detection limit and resides in an area rich in GRBs, with a notable presence of optical quasars (Figure 3.11). Its classification as a quasar aligns with previous identifications by Tie et al. (2017).

3.3.7 SRC209991

SRC209991 is located at RA 03:32:11.6 and DEC −27:37:26.3. The radio light curve shown in Figure 3.10 shows clear variability between a range of 3.12 - 5.99 mJy. SRC209991 is identified as the brightest candidate of the 8, reaching a peak flux of 5.992 ± 0.025 mJy. The light curve, which includes 43 detections, aligns with the radio image cutout in Appendix A.7. Other radio surveys such as ATLAS reports a peak flux of 3.78 mJy with 20 percent uncertainties. NVSS J033211.3-273727 reports a slightly higher peak flux than MeerKAT's measurements. A VLASS source, VLASS1QLCIR J033211.64-273725.8, has a peak flux of 10.817 ± 0.122 mJy. RACS reports peak measurements of 3.001±0.279 mJy.

We identify the Quasar ATCDFS9 J033211.65–273726.3, located 0.71 arc seconds away. Falling within MeerKAT's 2σ positional uncertainty, we associate SRC209991's radio emissions with this quasar. SRC209991 also coincides with the Pan-STARRS source PSO J053.048–26.264, exhibiting an optical flux of 0.812 ± 0.001 mJy. GAIA source 5060509521040997376 confirms this as a quasar, with g measurements of 18.7209 ± 0.003 mas/y. DES measurements align with GAIA, particularly the g magnitude of 18.9971 ± 0.0018. The X-ray counterpart LSXPS J033211.8-273724 shows a mean count rate of 7.9 (±0.9)x10^{-3} ct s^{-1}. Infrared associations are found in WISE source J033211.66–273726.3.

SRC209991 falls within the optical quasars region, above the FIRST detection limit, and within the SDSS limits, see Figure 3.11. The constant ratios position the source within the optical quasars region. Therefore, we classify SRC209991 as a quasar, consistent with the previous classification of its counterpart ATCDFS9 J033211.65–273726.3.

3.3.8 SRC210499

SRC210499 is located RA 03:31:27.1 DEC –27:44:09.9. The light curve of SRC210499 shows clear radio variability, within a flux range of 0.03 - 0.28 mJy (Figure 3.10) and this is supported by the radio image cutout in Figure A.5. ATLAS reports the nearest source, ATCDFS J033127.51–274440.1, with a peak flux of 0.15 mJy and an integrated flux of 0.14 mJy, with 20 percent uncertainties. No NVSS or VLASS associations were identified within the 2σ positional uncertainty.

SRC210499 aligns with the known quasar J033127.-0-274410, located 0.53 arcseconds away. The associated Pan-STARRS source PSO J052.8627-27.7363 exhibits an optical flux of 0.0131±0.0004 mJy. DES provides Sloan filter magnitudes in g, r, i bands (Table 3.4). WISE source J033126.13-274356.7 is also associated.

SRC210499 is positioned below the FIRST detection limit and significantly fainter than the 95 percent completeness limit, SRC210499 resides among GRBs and optical quasars (Figure 3.11). Its classification warrants further investigation, despite its association with the quasar J033127.0-274410.

3.3.9 SRC213653

SRC213653 is located at 03:28:49.69 –27:18:55.71. The light curve of SRC213653 shows clear radio variability, within a flux range of 0.014 - 1.041 mJy (see Figure 4.2) and this is further supported by the radio image cutout in Figure 4.3. There are no other radio measurements from the searched survey for this source.

SRC210499 aligns with a known low mass proper star LP888-63, located 0.107 arc seconds away. DES provides Sloan filter magnitudes in g, r, i, bands seen in Table 3.4. There is no PanSTARRS object associated with this source. There nearest X-ray detected source is MMSL2 J032848.9-271903. WISE also reported a detection at this location, J032849.02-271900.4.

SRC210499, our most interesting source, resides above the FIRST detection limit but below the 95 percent completeness limit and towards the right of the SDSS saturation limit (see Figure 3.11). It occupies a region sparsely populated by stellar objects. The diagonal lines on the radio-optical ratio plot suggest consistency with a star

The multi-wavelength counterparts and source classification of SRC213653 is seen in Chapter 4, where a well detailed study of the source is presented.

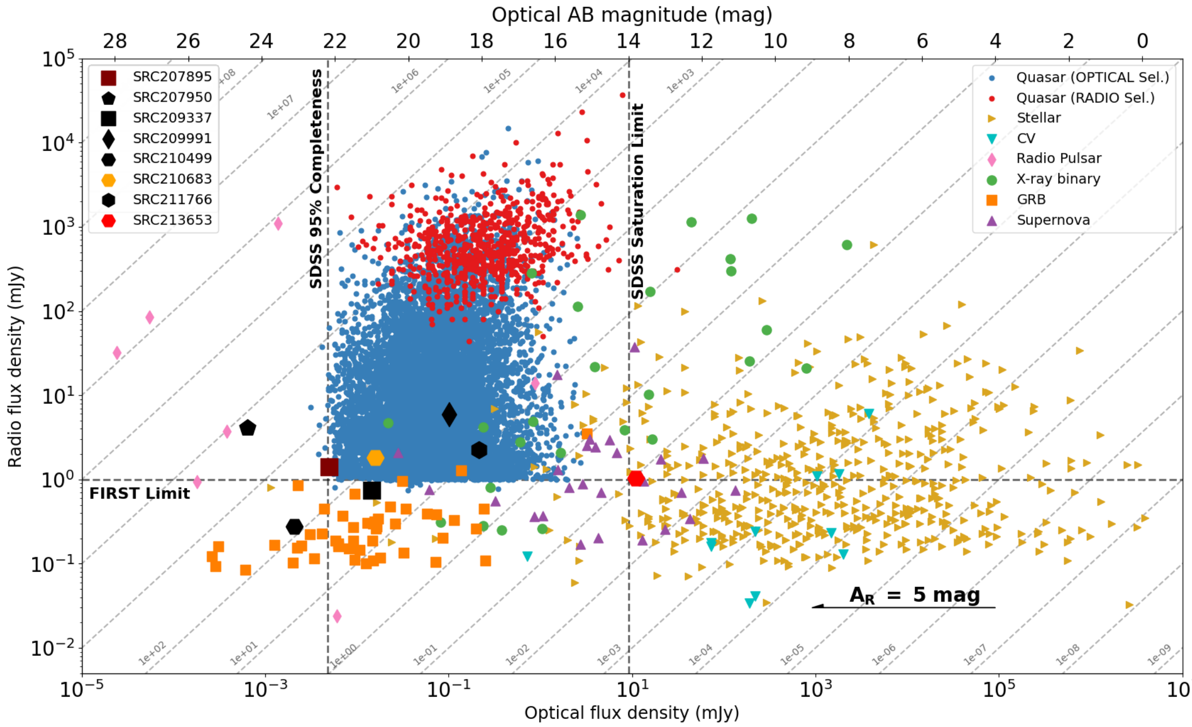

Figure 3.11: Relationship between radio and optical flux between known different variable sources and transients, adapted from Stewart et al. (2018). We plot our 8 interesting candidate sources seen on the Figure and referenced on the top left of the plot, each with a different shape. We use this plot to further classify the each source we found based on their location on the plot.

3.4 Variability Investigation

We investigate variability in our sources using the methodology outlined in Section 2.4. This analysis yields the modulation index (V_{RISS}), representing predicted variability, and the associated variability time scale. Our focus is to distinguish between intrinsic and extrinsic variability, especially given that most sources are classified as Active Galactic Nuclei (AGNs). Previous studies, like Angelakis et al. (2012), suggest that AGNs' low-frequency variability is primarily extrinsic, attributed to Refractive Interstellar Scintillation (RISS) Rickett (1990). Table 3.5 displays results obtained using the code by Hancock et al. (2019). We compare V_ν with predicted V_{RISS} and corresponding variability time scales at 0.816 GHz. If V_{RISS} significantly exceeds V_ν, it suggests RISS could substantially contribute to observed variability. Conversely, if V_ν dominates, other factors may influence variability. Short time scales indicate faster RISS-induced variations. Our analysis reveals that SRC207895, SRC209337, SRC211766, SRC207950, SRC209991, SRC210499, SRC210683 show significantly larger V_{RISS} values, indicating RISS's influence. Short time scales align with RISS-induced variations. Except for SRC213653, which exhibits comparable V_{RISS} and V_ν, suggesting intrinsic factors other than RISS may dominate variability. The associated time scale is consistent with intrinsic variations.

Source ID	V_ν	V_{RISS}	Time scale (year)
SRC207895	0.21	0.34±0.01	0.06±0.004
SRC209337	0.22	0.35±0.01	0.05±0.004
SRC211766	0.21	0.47±0.05	0.02±0.007
SRC207950	0.18	0.38±0.04	0.06±0.02
SRC209991	0.18	0.40±0.01	0.04±0.005
SRC210499	0.41	0.47±0.05	0.02±0.007
SRC210683	0.19	0.47±0.05	0.02±0.007
SRC213653	1.37	0.35±0.01	0.05±0.002

Table 3.5: The variability parameters and assessments of Refractive Interstellar Scintillation (RISS) for observed radio sources at a frequency of 0.816 GHz. The sources are categorized based on the comparison between the observed Variability parameter (V_ν) and the predicted RISS variability parameter (V_{RISS}), along with the associated variability time scale.

Chapter 4

Discovering the radio counterpart to a low mass star LP 888-63

This chapter details the analysis of our most interesting source. We begin with examining its key characteristics such as its radio variability. We explore the optical photometry data, discussing significant findings and correlation of other observations. We then investigate possible counterpart associations using multi-wavelength data.

4.1 SRC213653

SRC213653 stands out as a outlier in Figure 3.8. Prior to the systematic correction applied to the light curve, it exhibited values of η_ν and V_ν at 32.951 and 1.372 respectively. After correction, the V_ν value shifted minimally to 1.371, with no changes in η_ν. The peak flux of this source is measured at 1.041 ± 0.043 mJy (see Figure 4.2). TraP detected the source 13 times across all epochs, as seen in the light curve (see Figure 4.1), supported by manual inspection of images (refer to Section 2.3.3) seen in the radio image cut-outs depicted in Figure 4.3, highlighting flux changes from epoch to epoch. To handle non-detections, we used a python script that represents data points below a 3σ threshold as upper limits, with σ denoting the local noise (RMS) for each epoch. Figure 4.1 shows the complete light curve of SRC213653 obtained from the TraP source monitoring function, with a peak flux of 0.912 ± 0.040 mJy. This is lower than the peak flux from blind searches (1.041 ± 0.043 mJy) shown in Figure 4.2. This discrepancy arises because the source monitoring function does not update the location epoch-to-epoch during TraP searches, leading to flux underestimation (A. Andersson, private communication). Figure 4.2 shows a zoomed-in light curve from the TraP blind search running catalog during the second season of LADUMA observations. The source was detected 10 times in this season. Other radio surveys have not detected this source; no measurements are reported from other surveys, making the MeerKAT detection the first radio detection of the source.

The source is located at 03:28:49.69 –27:18:55.71, derived as the weighted mean of the 13 detection epochs using the Python Blob Detector and Source Finder (PyBDSF; Mohan & Rafferty (2015)). Cross-matching this position with the GAIA database yields Gaia EDR3 5060587895604134400 and Gaia EDR3 5060587895604134912. These two sources are associated with two sources found in the SIMBAD database; LAWD 14 and LP 888–63, approximately 12.72 and 18.88 arc seconds away from the radio emission, respectively. According to GAIA DR3 (Gaia

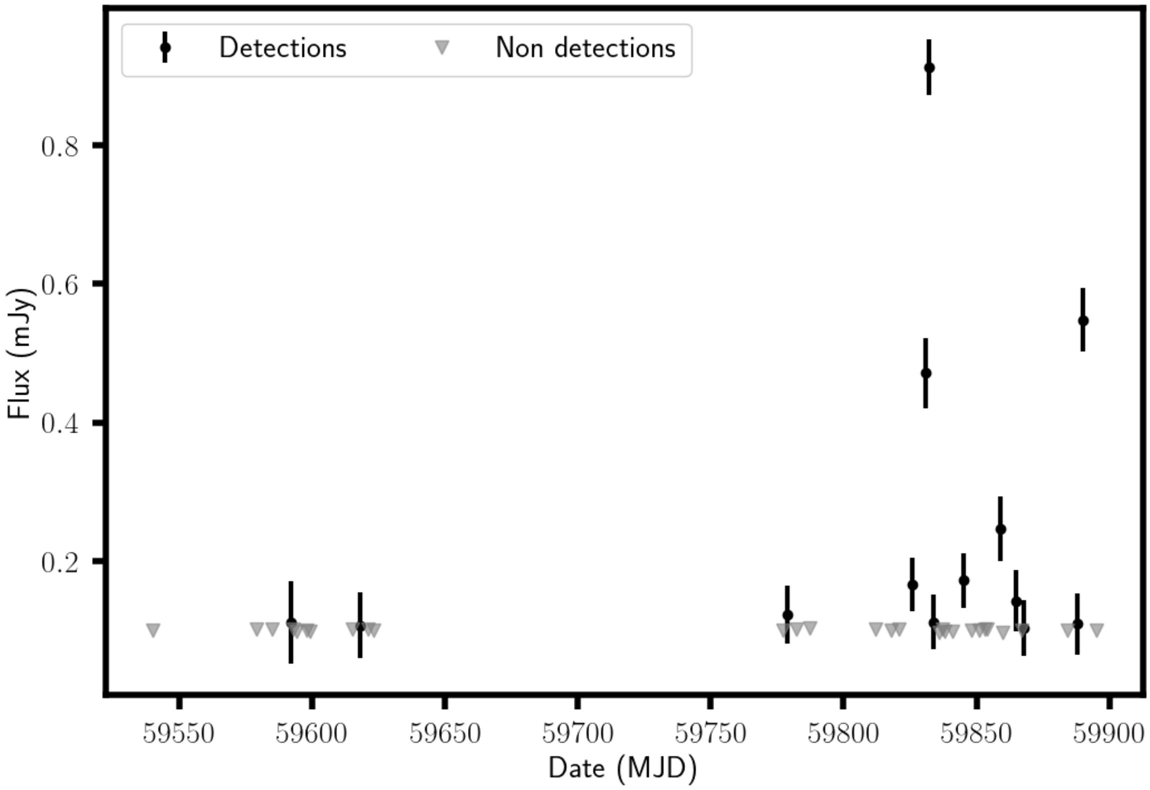

Figure 4.1: The radio light curve of candidate source SRC213653 from TraP source monitoring. The source is detected 13 times across all 41 epochs. Shown here are also the non detections plotted as upper limits, being the measurement below 3σ limit with σ being the local RMS in that epoch

Collaboration et al. 2021), LAWD 14's position is at 03:28:48.798 –27:19:00.096, with uncertainties of 0.28 and 0.39 mas, respectively. LAWD 14 exhibits a high proper motion of (721.338 ± 0.017) yr^{-1} in RA and (376.046 ± 0.025) mas yr^{-1} in DEC, totaling 813.473 mas yr^{-1}. Similarly, LP 888–63's position is at 03:28:48.444 –27:19:04.603, with uncertainties of 0.39 mas and 0.56 mas, respectively. LP 888–63 displays a high proper motion of (733.085 ± 0.024) mas yr^{-1} in RA and (387.658 ± 0.035) mas yr^{-1} in DEC, totaling 829.272 mas yr^{-1}. Accounting for their high proper motions, LAWD 14's position adjusts to 03:28:50.09 -27:18:51.57, 6.05 arc-seconds away from the radio emission, exceeding the 2σ positional uncertainty of 1.2 arc-seconds (Andersson et al. 2022), ruling out its association with the radio events. Conversely, LP 888–63's adjusted position is at 03:28:49.69 –27:18:55.81, within 0.107 arc seconds of the radio emission and thus within the 2σ positional uncertainty (Andersson et al. 2022). Therefore, we associate LP 888–63 with the radio events from SRC213653. LP 888–63's absolute parallax measurement is π = 43.410 ± 0.039 mas (Gaia Collaboration et al. 2021), indicating its proximity to the Sun at (23.030 ±0.020) pc, consistent with measurements in Stassun et al. (2019). No Pan-STARRS-associated source is found at this position, while an infrared-associated source is identified in WISE J032849.02-271900.4.

4.1.1 Optical Photometry

LP 888–63 has a significant survey coverage in the photometric sky, with catalogued measurements in various datasets such as the All WISE data release (Cutri et al. 2021), the Two-Micron All-Sky Survey (Cutri et al. 2003), Luyten

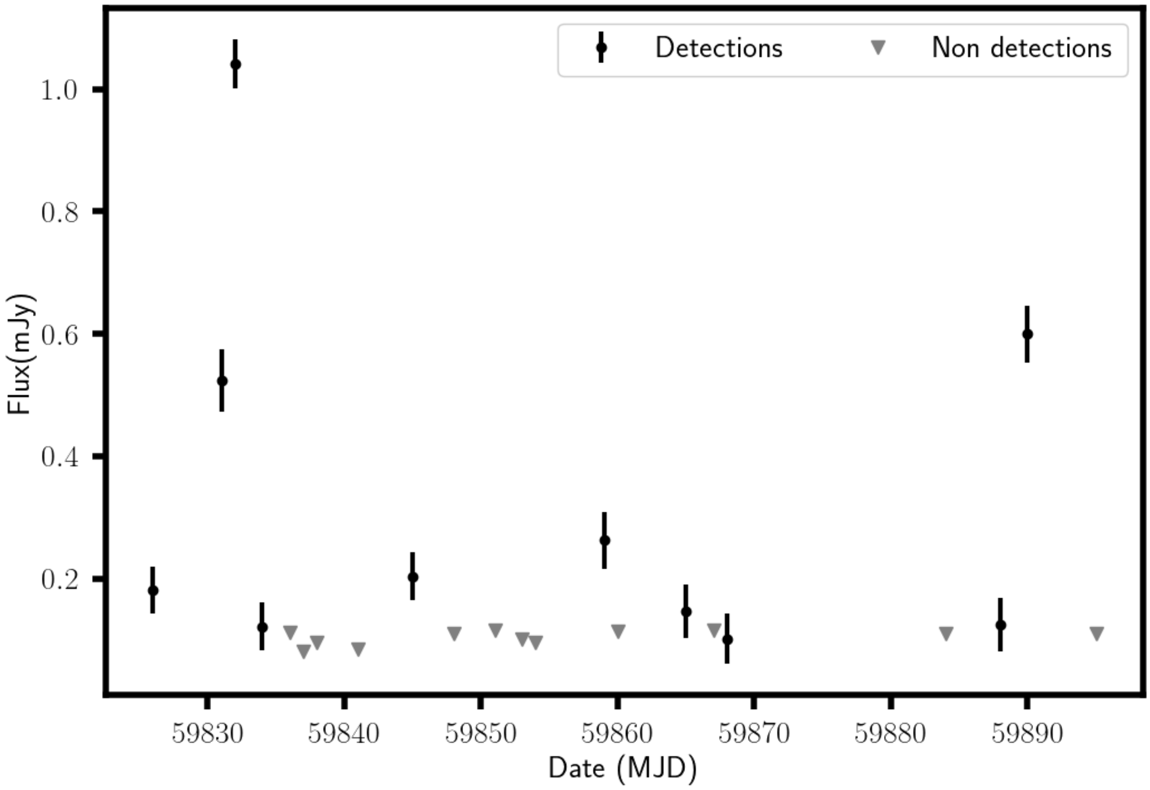

Figure 4.2: Zoom in radio light curve of candidate source SRC213653 from TraP during the second season of the LADUMA observations. The source is seen to reach peak flux of 1.041 ± 0.043 mJy during the 10 detection. Shown here are also the non detections plotted as upper limits, being the measurement below 3σ limit with σ being the local RMS in that epoch.

Half-Second (Luyten 1979a), New Luyten Two-Tenths (Luyten 1979b), and the Catalogue and Bibliography of UV Cet stars (Gershberg et al. 1999). It is characterised as a Low mass eruptive star (Schneider et al. 2019) and a high proper motion star (Schneider et al. 2016). LP 888–63, also known as L 587-77 B, is identified as an M3.5 companion to a high proper motion white dwarf binary system WD 0326-273, forming a triple system binary with LP 888–63 as the outer companion. Observations indicate a separation of approximately 7 arc-seconds (Nelemans et al. 2005) between the components, reinforcing LP 888–63's role as the primary source of radio activity. Additional observations from TESS, MeerLICHT, and ASAS-SN confirm the presence of flaring behaviour.

Band	**Magnitude**	**Spectral Type**	**Reference**
B	15.6		SIMBAD
V	13.80 ± 0.031	M3	(Luyten 1979b);(Bidelman 1985)
G	12.43 ± 0.0027		(Gaia Collaboration et al. 2020)
J	9.59 ± 0.026		(Cutri et al. 2003)
H	9.003 ± 0.022		(Cutri et al. 2003)
K	8.771 ± 0.021		(Cutri et al. 2003)

Table 4.1: Magnitudes and spectral types for different bands of the Low mass star LP 888–63 .

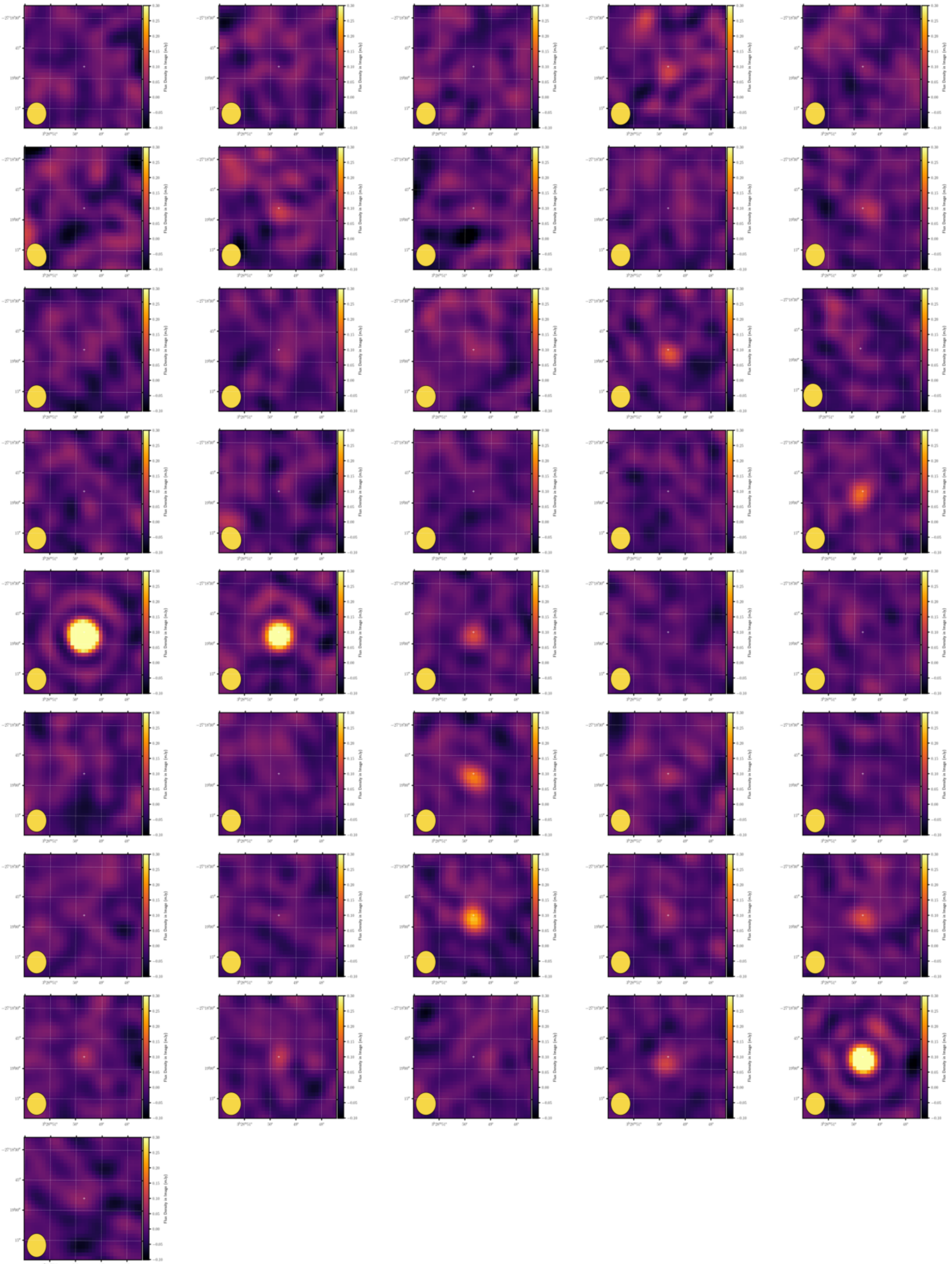

Figure 4.3: The radio image cut-out of SRC213653 from the 41 LADUMA observations The images are plotted chronologically from the top left to the right. In all the images the synthesised beam is found on the bottom left corner of each image. All the images are scaled to the same flux density range of (0.1 - 0.3) mJy on a linear scale. The source can be seen varying in flux from epoch to epoch.

4.1.1.1 TESS

The source is observed by TESS as TIC 144538915 in both sector 4 and 31. Clear flares are seen in sector 31 and not in sector 4 (The term "sector" refers to a specific region of the sky that the satellite observes during a given time period. Each sector represents a different region of the sky, and over its mission, TESS aims to cover nearly the entire sky, allowing it to detect exoplanets across a wide area). The full light curve is shown at top part of Figure 4.4. We perform a Lomb-Scargle periodogram (Lomb 1976, Scargle 1982) on the the light curve with the aim to determine the periodicity of the star and we get a period of P = 5.780 ± 0.507 days in sector 31 and P = 6.076 ± 0.133 days in sector 4. We perform bootstrap analysis to obtain the uncertainties on the period (Ivezić et al. 2014, VanderPlas 2018). Assuming a 63.3 percent confidence interval the values are in agreement as the uncertainties overlap with each other. This is consistent with the value found in sector 4 where a period of P = 6.176 ± 0.535 days is recorded for this source with TESS two minutes cadence (Fetherolf et al. 2023). Folding the light curve of sector 31 shows a quasi-sinusoidal periodicity trend as seen in the bottom plot of Figure 4.4. The source is estimated to have a mass of 0.297±0.020 $M_{\odot}$, radius of 0.317±0.010 $R_{\odot}$ and lastly an effective temperature of 3297.0±157.0 K in The TESS Input Catalog and Candidate Target list (Stassun et al. 2019). With this effective temperature of this, it supports the findings by Nelemans et al. (2005) and Tamazian et al. (2014) where the source is catalogued as a UV Ceti star being an M3.5 type. According to Rajpurohit et al. (2013) the effective temperature of $\sim$ 3200 K is in agreement with an M3.5 type star. According to Bidelman (1985) as also seen in Table 4.1 they classify the star as a M3 which is still in agreement with the spectral type and the source being a mid-M type. Making use of the listed recorded by Stassun et al. (2019) and our calculated period from the TESS sector 31 light curve, and assuming that the sources rotates as a rigid body we use equation 4.1 and propagate the uncertainties to calculate the the rotational velocity of the source to be 2.77±0.12 km/s. This is within what most systems or dwarfs known to have values of $\sim$ 2 km^{-1}, as seen in Gizis et al. (2017).

$$v_t = \frac{2\pi R}{P} \tag{4.1}$$

4.1.1.2 ASAS-SN

There are over 1489 epochs observed by ASAS-SN for LP 888–63. From the aperture photometry we find that the source shows minimal optical flares (i.e., very few or none except for a single notable instance, see Figure 4.5) between a range 12.50 - 16.25 in the g-band magnitude as seen in Figure 4.5 during the time of the MeerKAT observations of SRC213653, reaching magnitude of 14.45. We do not find any simultaneous observation between MeerKAT and the ASAS-SN light curve.

4.1.2 Optical Spectroscopy

The associated optical counterpart LP 888–63 was observed in a fortunate observational confusion according to Nelemans et al. (2005) during the SPY project by European Southern Observatory (ESO ESO-VLT-U2). The observations of the target started 2000-07-12 09:57:31 and ended at 2000-07-12 10:02:31, at effective exposure time of 300s at a total exposure time of 300s using the VLT-UVES high resolution spectrograph [1]. With the spectrum

---

[1] `http://archive.eso.org/dataset/ADP.2020-09-11T05:49:55.279` (ESO Archive)

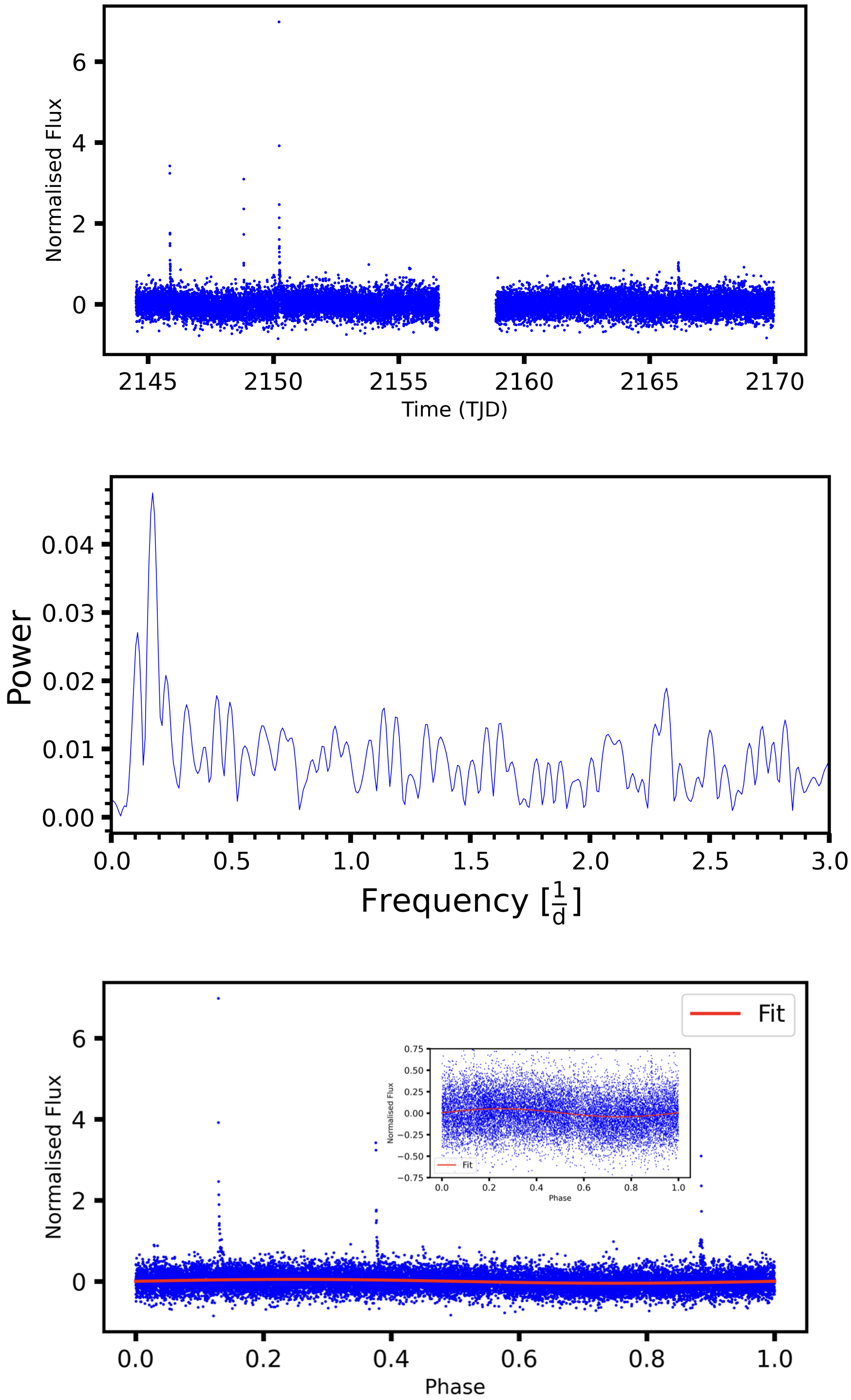

Figure 4.4: **Top** TESS full light curve of LP 888–63 showing clear flares in sector 31. Normalised Flux plotted with time. **Middle** Lomb-Scargle periodogram with best frequency of 0.184 days^{-1} and thus period of P = 5.780 ± 0.507 days. **Bottom** we show the folded light curve with a fit and a zoomed version (insert) showing a quasi-sinusoidal behaviour.

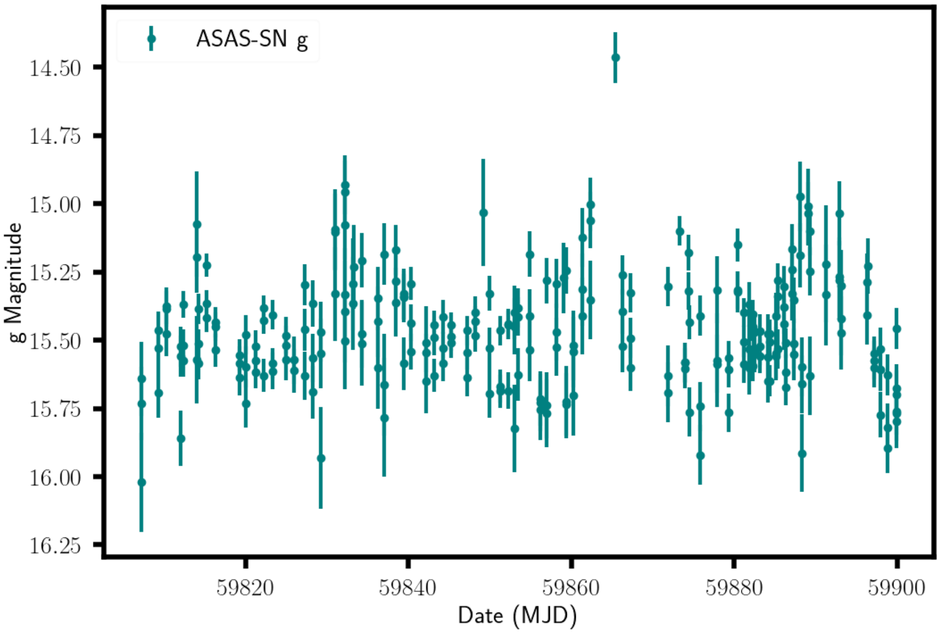

Figure 4.5: ASAS-SN light curve of LP 888–63, with the g magnitude plotted against the time in MJD. The source exhibits constant behaviour with a sinusoidal trend and minimal optical flares reaching magnitude of 14.45 in g band.

available, we can investigate the spectral type of the star and magnetic activity of the of the star. The spectra seen in Figure 4.6 shows two clear emission lines, Hβ at $\sim$ 4861 Å and Hα at $\sim$ 6560 Å. We then calculate the equivalent widths (EW) of the Hα emission line integrated between the Hα continuum region 6558.8 Å and 6466.8 Å detailed by Newton et al. (2017). We find the calculated EW for the Hα to be -1.74 Å, indicating that LP 888–63 is a magnetically active star, as seen in Newton et al. (2017) where stars with EW < -1 Å are considered to be magnetically active.

4.2 MeerLICHT

There is rich coverage of LP 888–63 with MeerLICHT in all the MeerLICHT filters. We show the full MeerLICHT light curve of the source in Figure 4.7. The source is seen to be brighter in the redder wavelengths than in the bluer wavelengths, as would be expected for an M3.5 star. To understand more about how the source evolves and behaves in colour, we plot the colour-magnitude diagrams of the full MeerLICHT light curve for the $(u-q)$ vs u magnitude, $(u-q)$ vs q magnitude, and $(u-q)$ vs time (see Figure 4.8). We calculate the absolute magnitudes of the filters u and q by making use of the distance obtained above of (23.030 ± 0.020) pc and apply it to Equation 4.2

$$m - M = 5\log(\pi^{-1}) + 5 \tag{4.2}$$

where m denotes the apparent magnitude from MeerLICHT, M being the absolute magnitude and π being the the parallax of the source as measured by GAIA.

We see the source being predominantly red when it is in a quiescent state and becoming blue when it flares, as seen

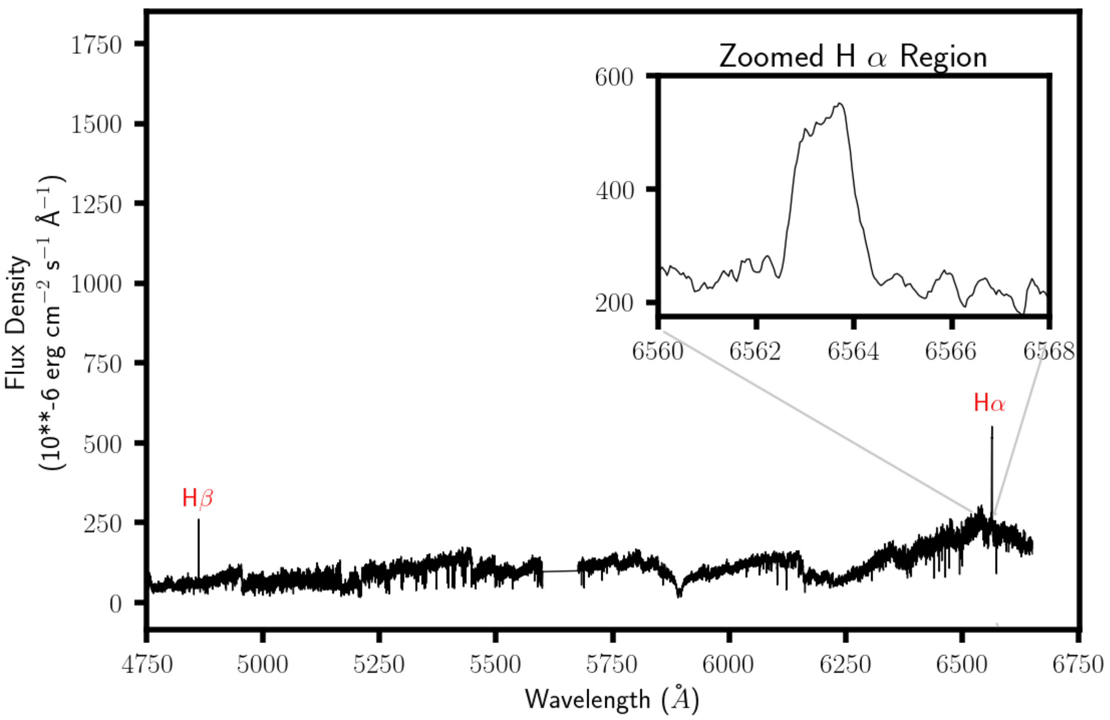

Figure 4.6: Spectrum of LP 888–63 (L 587–77 B) from the ESO archive. The spectra shows two clear emission lines, Hα and Hβ. We also show a zoomed view of the Hα emission line

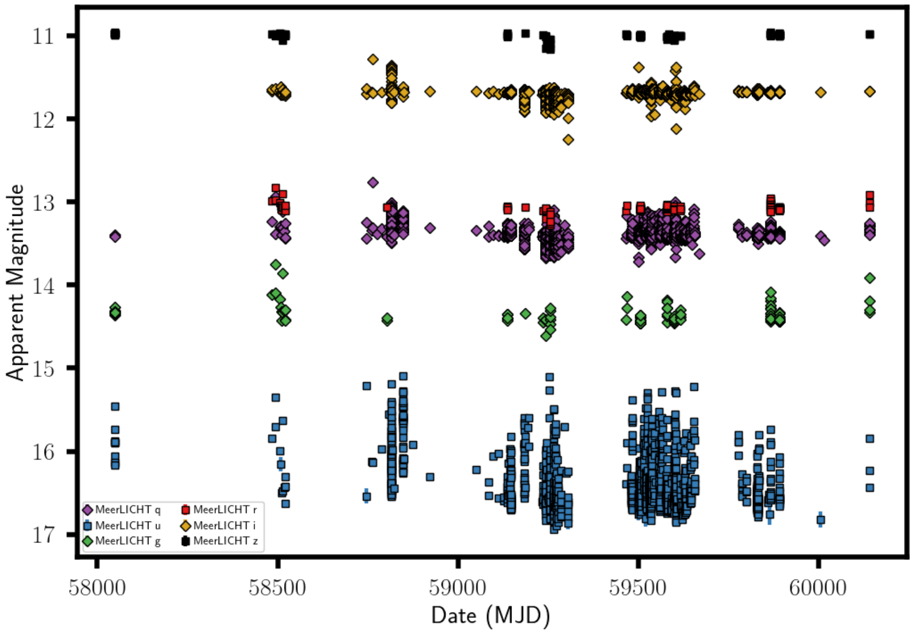

Figure 4.7: Full MeerLICHT light curve of LP 888–63, observed in all MeerLICHT filters. Showing much activity in the u band filter than in any other filters.

from both the $(u-q)$ vs u and $(u-q)$ vs q magnitude plots (see Figure 4.8). This behaviour indicates increased emission in the UV or blue part of the spectrum. We observe a downward trend in the plot, with a negative slope, indicating a decrease in brightness in the u band as the $(u-q)$ colour index increases. Lastly, the brightness of the source in the u band ranges from $M_u = 16.8$ to $M_u = 15.2$ magnitudes. This range indicates significant variability in the star's brightness during the observed period. This is the typical variability range in the ultraviolet for M dwarfs, which aligns with the star being previously catalogued as a UV Ceti (Rajpurohit et al. 2013) and also agrees with the work on variability in the ultraviolet for M dwarfs by Hawley et al. (2003).

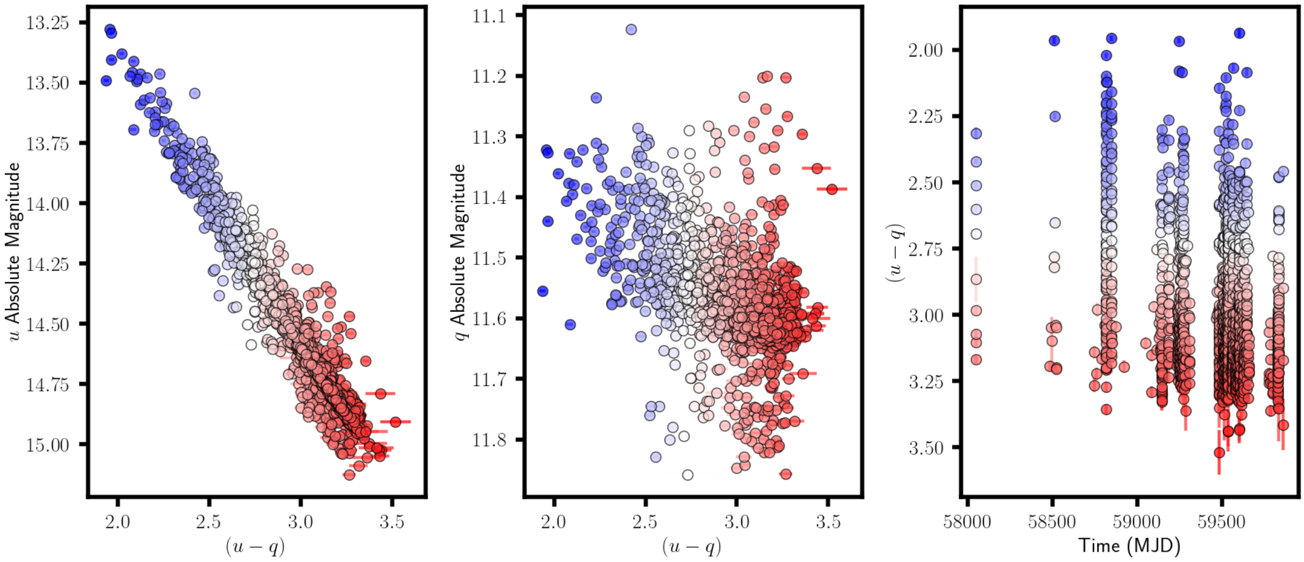

Figure 4.8: Colour magnitude diagram of source LP 888–63 across all MeerLICHT observations of the source shown on the first and second plot from the lift. The fist plot from the left shows the colour magnitude diagram of u-q vs u band while the middle plot is of u-q vs q. The last plot from the left is the colour evolution of the source.

We find simultaneous colours $(r-i) = 1.37 \pm 0.13$ and $(i-z) = 0.67 \pm 0.23$ mag, with these values being in line with what one would expect for an M3 star as seen in West et al. (2005). This is seen in the zoomed single flare on the MeerLICHT light curve seen in Figure 4.9.

4.2.1 Flare temperature and luminosity

Assuming a blackbody, we can further calculate the star's effective temperature and the effective temperature of the flare. From these temperatures, we derive the luminosity and consequently estimate the radiating area by employing Equation 4.3. We conduct a cross-matching between known GAIA stars observed with MeerLICHT to establish the colour relation and, consequently, the effective temperature. A similar relation was derived in Ballesteros (2012), where they established Equation 4.4.

$$L = 4\pi\sigma R^2 T^4 \tag{4.3}$$

We formulate analogous equations for the MeerLICHT colour indices $(u-q)$ and $(q-i)$ in Equations 4.5, 4.6, 4.7, and 4.8.

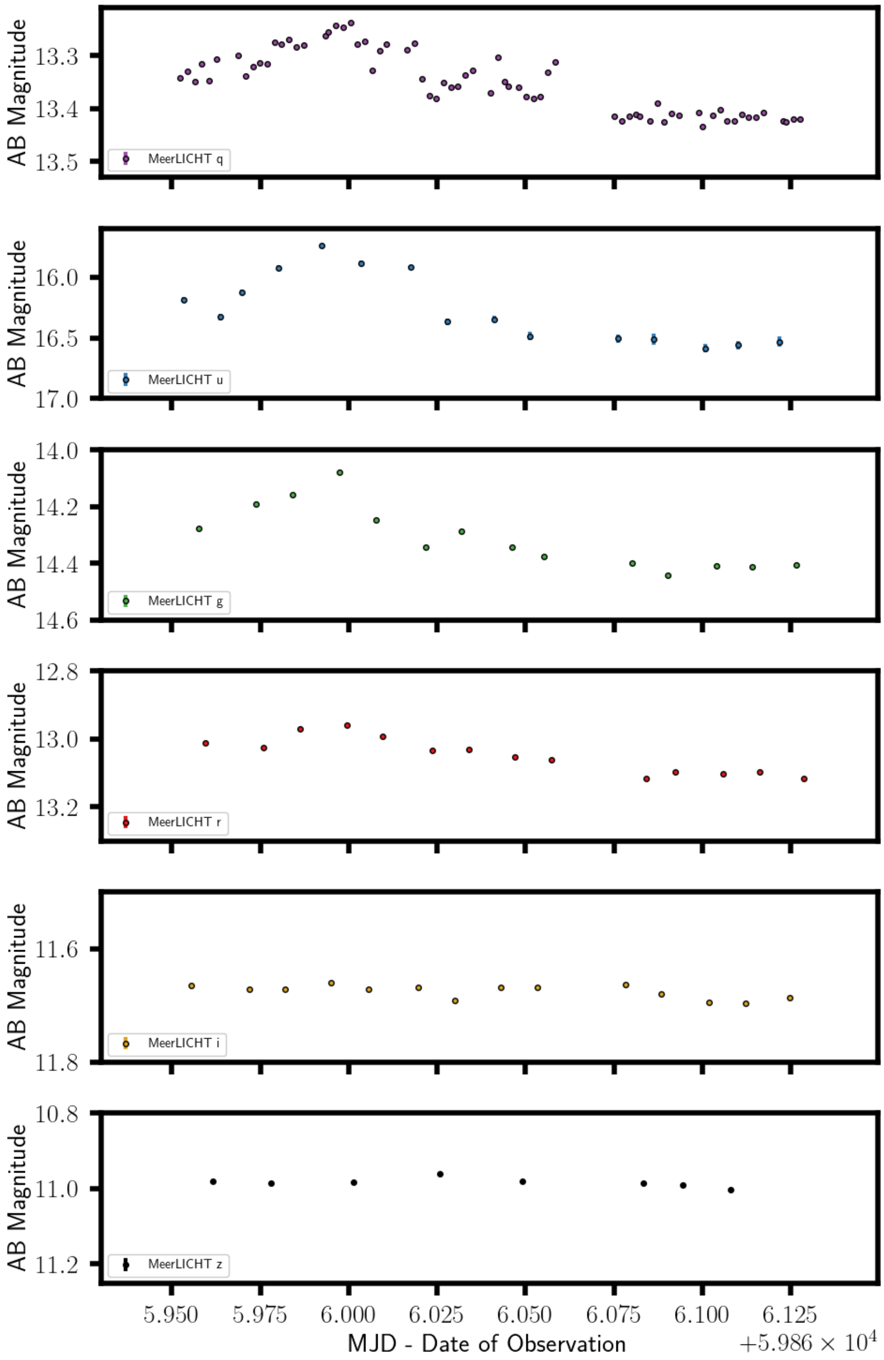

Figure 4.9: Zoomed in MeerLICHT light curve on a single flare event. See flares in the q,u,r with indication of simultaneous colours $(r-i) = 1.37 \pm 0.13$ and $(i-z) = 0.67 \pm 0.23$ mag

$$T = 4600\left((0.92(B-V))^{-1} + 1.7 + (0.92(B-V))^{-1} + 0.62\right) \tag{4.4}$$

$$\text{for } (u-q){>}\ 0.2 : T = 6750\left((u-q) + 0.75\right)^{-1} + 2500 \tag{4.5}$$

$$\text{for } (u-q){<}\ 0.2 : T = 9000\left((u-q) + 1.00\right)^{-2} + 2500 \tag{4.6}$$

$$\text{for } (q-i) > \text{-0.2} : T = 90000\left((q-i)+2.60\right)^{-3} + 2250 \tag{4.7}$$

$$\text{for } (q-i) < \text{-0.2} : T = 6750\left((q-i)+1.15\right)^{-3} + 2250 \tag{4.8}$$

For a more detailed discussion on how these equations were obtained, please refer to the work by Sumari Barocci-Faul (Master's thesis in preparation). Using these equations, we can calculate the temperature of the star during quiescence and the temperature during the flare.

To calculate the temperature of the flare, we initially estimate the quiescent state of the star and subtract from the total brightness of the star to isolate only the flare. This process is carried out using a python script, and a Gaussian is fitted to the u, q, and i filters, as illustrated in Figure 4.11. This presents the measurements displayed in Table 4.2. We obtain these estimates by converting quiescent state values into their respective luminosities for each filter using $M = -2.5\log\left(\frac{L}{L_\odot}\right)$. The reason behind this approach is that magnitudes cannot be subtracted directly; therefore, we choose to perform the operation in terms of luminosity. All magnitudes in the respective filters were transformed into luminosities, and the operation (e.g., $L_{\text{u star}}$ - $L_{\text{u quiescent}}$) was applied. Once we removed the quiescent state and were left with only the flare, we converted back to colour indices, $(u-q)_{\text{flare}}$ and used Equation 4.6. This allows us to plot the temperature of the flare against the colour indices, as illustrated in Figure 4.10. In Figure 4.10, it is worth noting that he higher quiescent temperature compared to the literature value of T=3900 K for M dwarfs is not surprising. The $(u-q)$ colour index is not a good measure for determining the continuum slope of the Spectral Energy Distribution (SED) in late M-type stars (West et al. 2005).

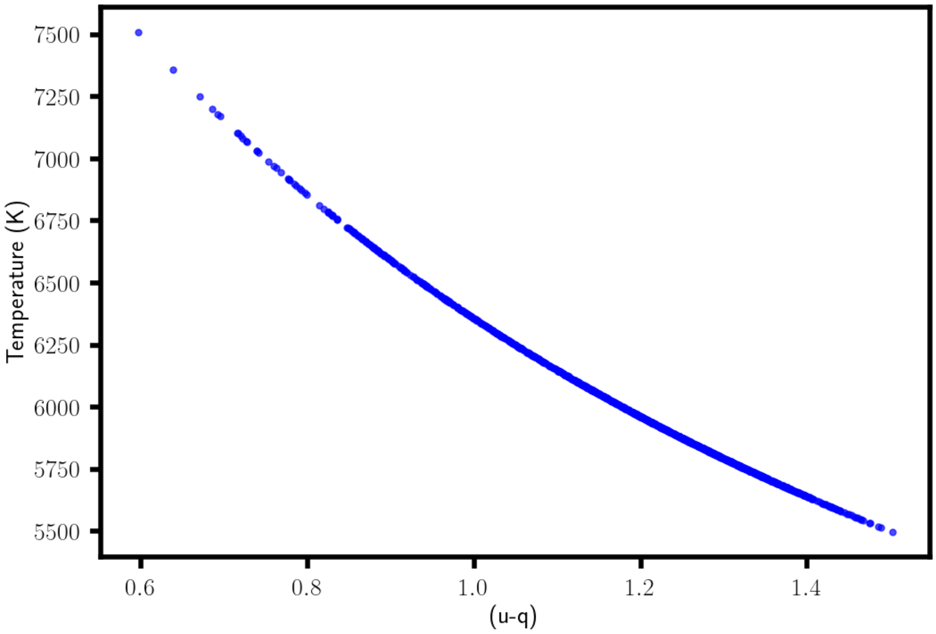

Figure 4.10: Showing the effective temperature of the flare, seen to peak at corresponding colour index of $(u-q)_{\text{flare}}$ $\sim$ 0.59 and reaching a temperature of approximately 7500 K.

The peak temperature is identified at $(u-q)_{\text{flare}} \sim 0.59$, corresponding to a temperature of approximately 7500K (also evident in Figure 4.10). This value is within the range of what would be expected for a M-dwarf star to have as also seen in Kowalski et al. (2015). It is worth stating that this is just the estimated temperature. The equations used to obtain this temperature are still in development and thus there are no uncertainties being quoted as of yet.

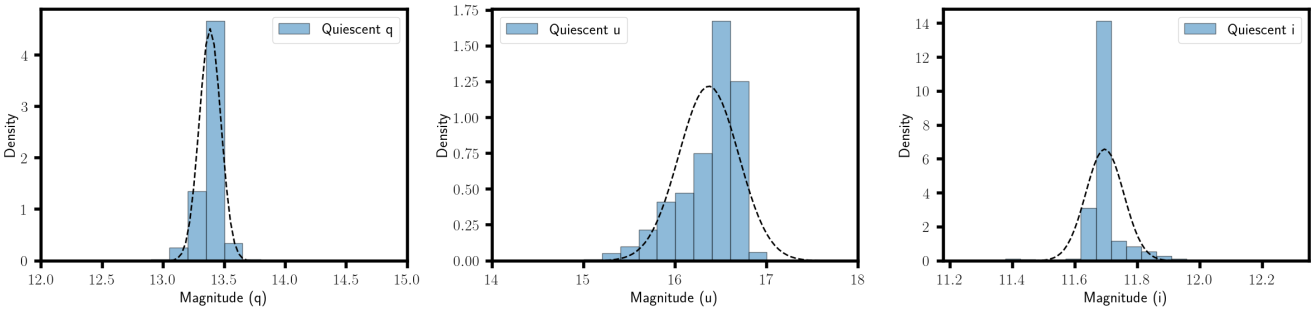

Figure 4.11: Observed absolute magnitude of the u,q and i filters being fitted with with a Gaussian to estimate the quiescent state of the star in the respective filterers.

Filter	Absolute magnitude	Quiescent Gaussian fit	Quiescent Luminosity (erg s^{-1})
u	14.56	mean: 16.37 std: 0.33	9.268e+28
q	11.57	mean: 13.38 std: 0.09	1.455e+30
i	9.89	mean: 11.70 std: 0.06	6.839e+30

Table 4.2: Output measurements from the Gaussian fit of the u,q,i filters.

It is worth noting that we typically observe stars through specific filters or wavelengths. However, stars emit energy across a broad spectrum, from radio waves to gamma rays (Carroll & Ostlie 2017). The observed flux is just a fraction of the total energy emitted by the star. The Bolometric correction (BC) helps in estimating the total energy output by correcting for this incomplete observation. To obtain the bolometric corrections, we model a blackbody for a number of known effective temperatures of stars, as seen in Figure 4.12 using the following equation,

$$B(\lambda, T) = \frac{2hc^2}{\lambda^5} \frac{1}{e^{\frac{hc}{\lambda kT}} - 1} \tag{4.9}$$

where $B(\lambda, T)$ represents the spectral radiance of a black body at temperature T and wavelength λ. Here, h denotes Planck's constant, c stands for the speed of light and k represents the Boltzmann constant. Next, integrating under the curve give the total intensity that is being emitted by the star and we further integrate in the specific MeerLICHT u,q,i filter bands to find how much intensity is being observed from each, as also shown in Figure 4.12.

It is worth mentioning that taking the integral of Equation 4.9 over all wavelength is not possible. We chose reasonable limits and integrate from 100 nm to 3500 nm. Taking the ratio of the total intensity and the intensity from a specific band gives how much intensity is being emitted by the specific band. We plot the effective temperatures against the found ratios as seen in Figure 4.13, and then the log of that to obtain the bolometric correction factors shown in Figure 4.14, We see similar approach in finding the bolometric correction factors on work by Condon et al. (1998) and Kowalski et al. (2010). We can then read off the corresponding bolometric correction factor for any star with a known effective temperature observed with the MeerLICHT telescope. Taking estimated effective temperature of LP 888–63 as reported in Stassun et al. (2019) of 3297±157 K, we can read the corresponding bolometric correction factor from Figure 4.14 to be –1.82, –0.76 and –0.85 mag in u, q and i respectively.

We make use of $BC = M_{\rm bol} - M_{\rm Absolute}$ to find the bolometric absolute magnitude $M_{\rm bol}$ which can be seen in Table 4.3. After which we find the bolometric luminosity of the flare, $L_{\rm flare}$ by using $M_{\rm bol} = -2.5 \log \left(\frac{L_{\rm flare}}{L_{\odot}} \right)$ and taking

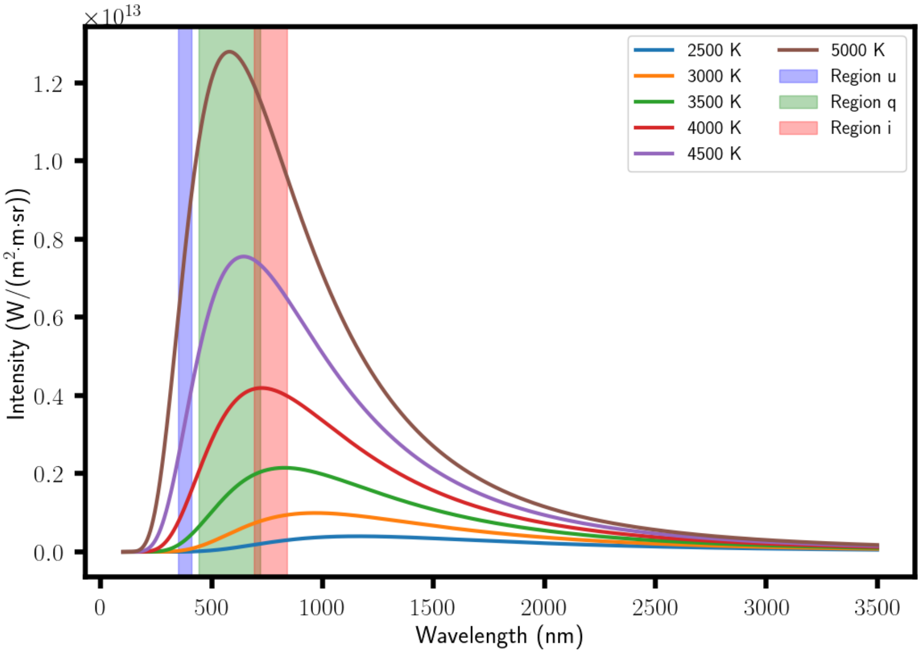

Figure 4.12: A Blackbody model of the several temperatures for known stars is shown. We further show the MeerLICHT u, q, i filter regions.

the difference between the luminosity in u and $u, quiescent$ as $(L_{\rm u}\text{-}L_{\rm u,quiescent})_{\rm flare}$ using the bolometric absolute magnitudes, and find this to be $\sim 2.33{\times}10^{30}$ erg s^{-1}. We then find the estimates area of the flare to be $\sim 1.30{\times}10^{15}$ m^2 using Equation 4.3. Making use of the estimated radius of LP 888–63 of 0.317±0.010 $R_\odot$ by Stassun et al. (2019), we find the surface area of the star assuming a perfect sphere to be $\sim 6.08{\times}10^{17}$ m^2. We can compare the two areas by taking the ratio of the area of the flare to the area of the star and find this is $\sim$ 0.21 percent of the area of the star. This indicates that the flaring region is relatively small compared to the size of the entire star, suggesting that the flare originates from a localised region on the star's surface.

Band	BC mag	$M_{\rm bol}$	$M_{\rm absolute}$	$L_{\rm bol}$ (erg s^{-1})
u	–1.82	12.74	14.56	$2.42{\times}10^{30}$
q	–0.76	10.81	11.57	$1.43{\times}10^{31}$
i	–0.85	9.04	9.89	$7.29{\times}10^{31}$

Table 4.3: We show the bolometric measurements of LP 888–63 using MeerLICHT filter bands. Calculated bolometric luminosity $L_{\rm bol}$ for each filter is shown. Using these we find the luminosity of the flare $(L_{\rm u}\text{-}L_{\rm u,quiescent})_{\rm flare}$ to be $\sim 2.33{\times}10^{30}$ erg s^{-1}

In the search for simultaneous observations between the radio flares in Figure A.1, we made a plot to search for simultaneous observations between the radio flares and optical flares and we found none. This is further supported in Figure 4.15, where we plot the MeerLICHT most active band flux with the MeerKAT flux and still find no simultaneous observations within 0.5 days

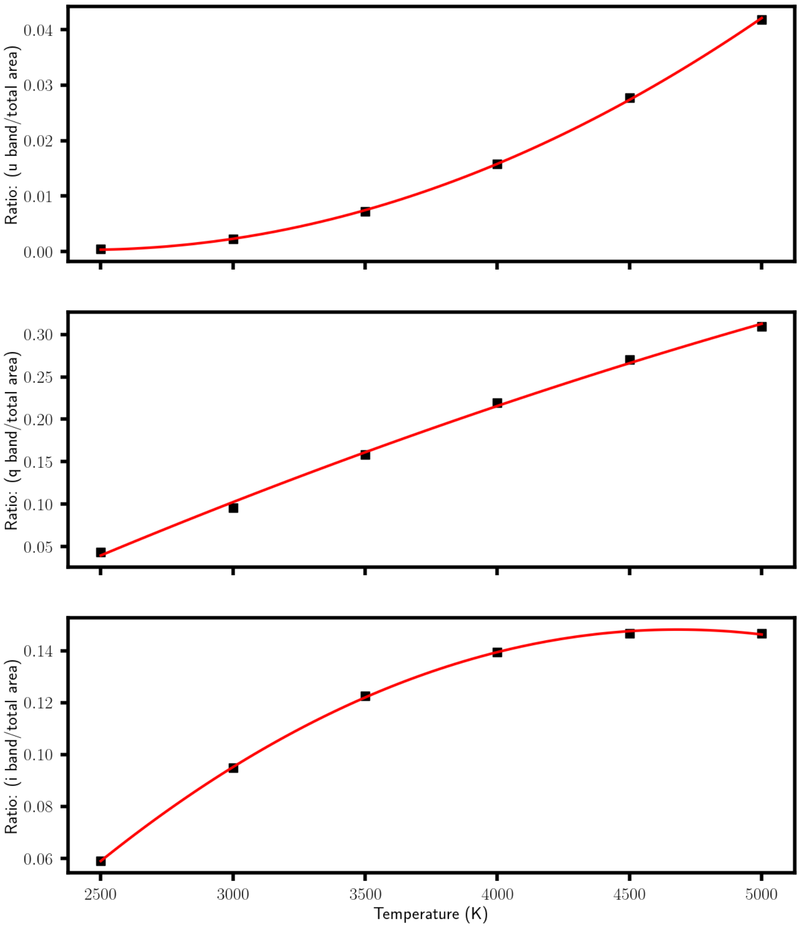

Figure 4.13: Showing intensity ratios from each of the MeerLICHT bands at a specific temperature. The temperatures used here correspond to these used to model the Blackbody in Figure 4.12.

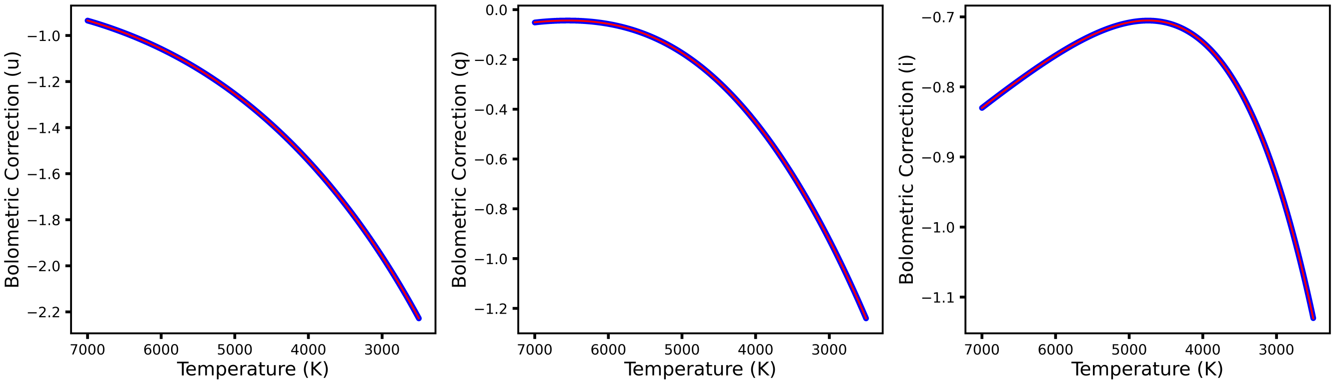

Figure 4.14: The relationship between the bolometric correction and temperature for MeerLICHT u,q,i filter bands.

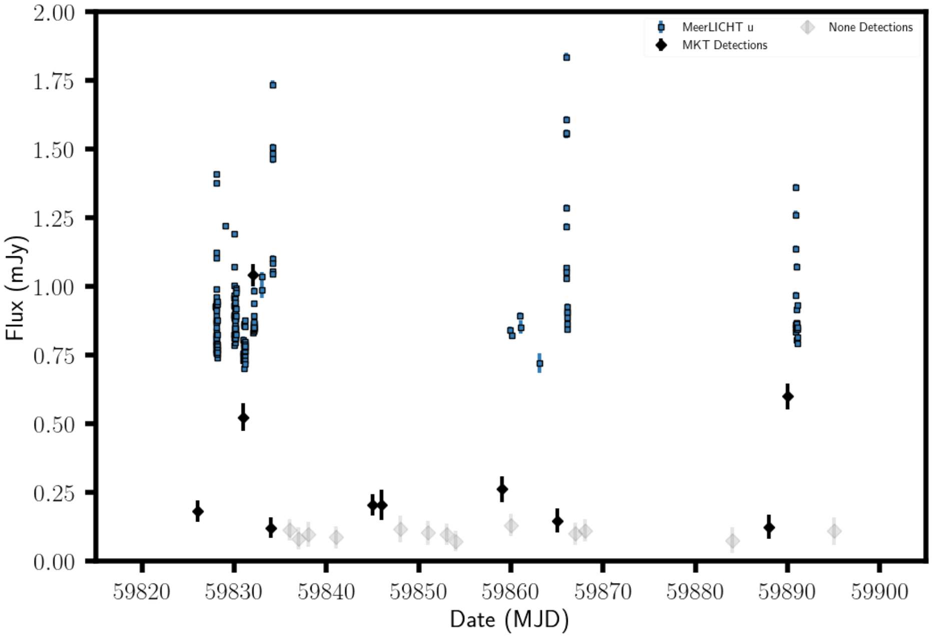

Figure 4.15: Light curve of the MeerLICHT and MeerKAT coupling in most active MeerLICHT u band filter. There is no simultaneous flare observations found between the Radio and the Optical observations.

4.3 X-ray Observations

The nearest X-ray ~~observation~~ detection to LP 888–63 is XMMSL2 J032848.9–271903 found to be at 6.31 arc seconds away from LP 888–63 (Salvato et al. 2018). XMMSL2 J032848.9–271903 lies within the 90 percent confidence interval to the GAIA association position. It it further flagged to have a match probability of 90.47 percent to LP 888–63 and flagged as a flare star by Freund et al. (2018). With this being said we can confidently associate the X-ray source to LP 888–63. XMMSL2 J032848.9–271903 is reported to have a flux limit of 1.4×10^{-12}erg s^{-1} cm^{-2} which corresponds to a luminosity of 8.86×10^{28}erg s^{-1} Hz^{-1}. To understand further the relationship with the radio and X-ray band of our source, we turn to the study by Benz et al. (1994), where they show a relationship between quiescent X-ray and radio luminosities of a number of different stars, like M dwarfs, K-dwarfs and RS CVn binaries. Such a relationship aids towards understanding and explain the connection that exits between inducing of radio emissions (by non-thermal, high energy electrons) and production of thermal X-rays (by the predominate coronal plasma). Because the X-ray emission measurement quoted above were not taken at the same time as the quiescent radio emission we plot only the quiescent radio limit against the above quoted X-ray measurement and thus declare that the position of the source seen in Figure 4.16 are just an estimate and not the definite position. We take the quiescent radio limit flux of SRC213653 to be 3× the lowest local RMS noise level across the 41 MeerKAT images as also seen in Andersson et al. (2022). The value we find as seen in Table 2.1 to be 12 μJy, this is equivalent to a luminosity of 2.27×10^{13}erg s^{-1} Hz^{-1} and when it is at its brightest it has luminosity of 6.59×10^{14}erg s^{-1} Hz^{-1} an other of magnitude above the quiescent state.

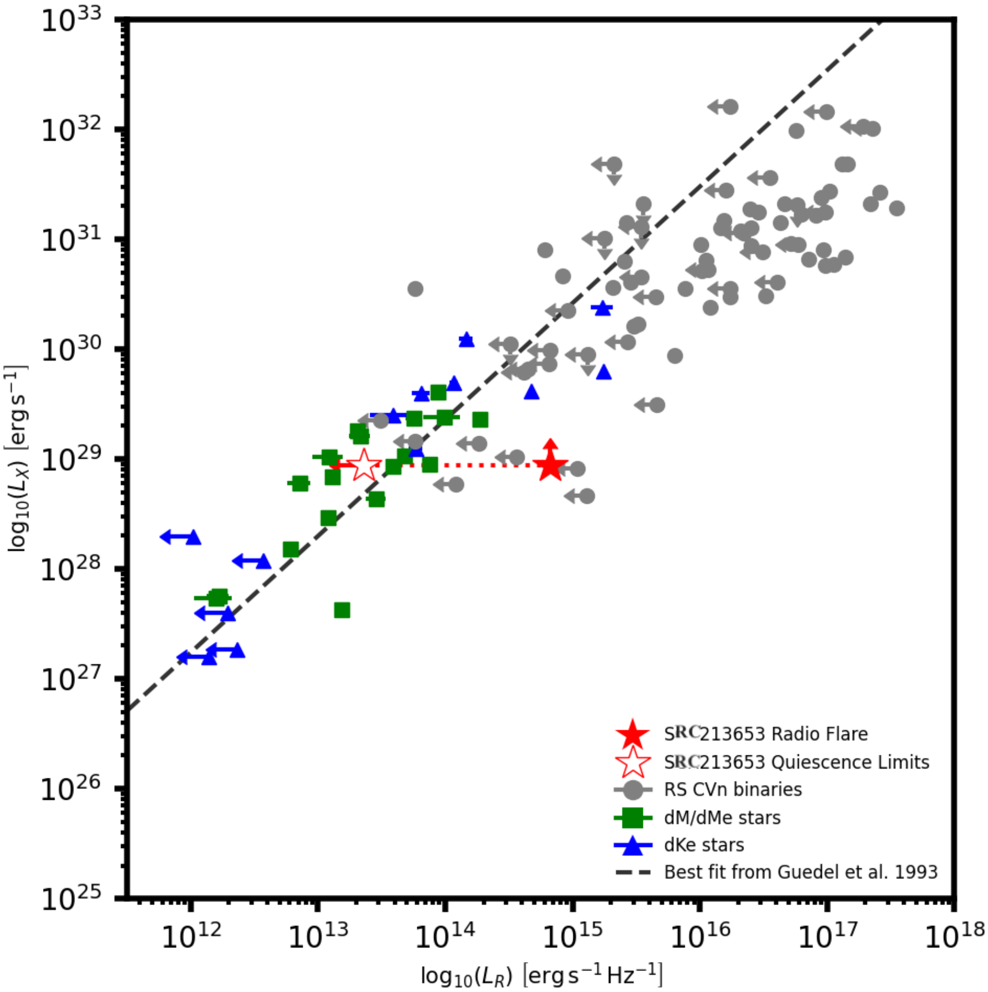

Figure 4.16: Benz et al. (1994) radio and X-ray luminosities plot of active stars. The x-axis shows the radio luminosities while the y-axis shows the X-ray luminosities. We find other active stars, such as RC CVn binaries, DM/DMe stars and dKe stars. Plotted here is limits on quiescent emission and the radio flare is also plotted seen to reach luminosity of 6.59×10^{14}erg s^{-1} Hz^{-1}. Plot updated from `https://github.com/AstroLaura/GuedelPlot`.

Chapter 5

Discussion and Conclusions

5.1 SDP Validation

I have validated the use of SDP images by comparing the number of sources that are retained in both sets of images. The SDP images recover ~ 67 percent of the sources that are present in the OxKAT images. This implies that using the SDP images only for commensal transient searches, we will only be missing out on ~ 33 percent of the candidates. A closer examination of the 43 sources that were not matched in the SDP images (See Table 3.1) marked in red in Figure 3.1 revealed that 15 of them exhibited variable or transient behavior. Their light curves, shown in Figure 3.2, indicate variability. Upon cross-matching these sources using their coordinates, we identified them as known AGN and Quasars. The remaining 28 unmatched sources in the OxKAT images were identified as extended sources rather than point sources. This difference can be attributed to the fact that the OxKAT images have been primary beam corrected, which results in more accurate flux measurements. In contrast, the fluxes in the SDP images are likely underestimated because these images have not undergone primary beam correction. This is illustrated in Figures 3.5 and 3.4, where the fluxes from the SDP images are consistently lower than those from the OxKAT images.The lower noise levels in the OxKAT images can likely be attributed to the use of direction-dependent (DDE) corrections, which are particularly necessary for the LADUMA field due to the presence of a strong confusing source. This allows for the detection of fainter sources, as shown in Table 2.3. In Figure 3.5, a greater number of sources from the OxKAT images are visible at lower flux levels compared to the SDP images. The reason for usages of SDP images is speed. With the SDP images being delivered within $\sim$ hours of observations then we could search for transients on that timescale.

5.2 Transient and Variable Hunt

We perform a commensal analysis and search for radio transients and variables in the MeerKAT's images in the LADUMA field. This analysis identified 8 interesting sources among which a new radio transient was seen to be coincident with a low mass proper motion star, LP 888–63. We ran all the images that had passed our filtering process detailed in section 2.1.1 into TraP, where we used the default parameters such as the detection threshold of 8σ and an analysis threshold of 3σ with a search radius of 2303 pixels, slightly above half of the image size. TraP returns a total of 7299 sources that could be potential transients or variables. We further performed filtering steps on these sources as detailed in section 2.3 based on η_ν and V_ν with the aim of identifying sources that are seen to have high values in both η_ν and V_ν, with only 290 passing the filtering steps. However, it is worth noting that this approach is biased towards sources that vary epoch to epoch, which could lead to losing potentially interesting sources that do not have high η_ν and V_ν values, as also seen in Andersson et al. (2023) where they perfrom the transient searches on the entire TraP output and do away with the η_ν and V_ν filtering. The V_ν parameter is essential as we use it to compare with the modulation index predicted by RISS when investigating the variability of the sources.

After the source filtering, we find 8 interesting sources: two are found above the V_ν limit and below η_ν, one lives below the V_ν limit and below η_ν limit, and lastly, the remaining five live below both the η_ν and V_ν limits (see Figure 3.8), however, above the new search region detailed in section 2.3. We follow the work by Driessen et al. (2022) on correlated light curves, performed light curve analyses, and corrected the light curves that were correlated to each other (see Figure 2.5 and 3.6). We performed multi-wavelength source association on all 8 sources, where we used the sources' locations and searched in the optical, radio, X-ray, and infrared bands. We found that all sources had potential optical and infrared source counterparts; some did not have any X-ray counterparts. Since all sources have optical counterparts, we made use of the radio fluxes and r magnitudes from DES to further plot these sources on the optical-radio plot by Stewart et al. (2018) to further understand the nature of the sources and classify them based on where they live on this plot (see Figure 3.11).

We find that all but one of the 8 sources are seen to live in the regions where most AGN and quasars are found (looking at the constant locations), and thus conclude the sources to be consistent with AGN and quasars.4 of the sources live well above the FIRST limit and well within the SDSS limits. This is consistent with work by Thyagarajan et al. (2011) where they found $\sim$ 87 percent of the sources using the FIRST limit survey being consistent with known and unknown AGN and quasars. We further use the model detailed in Hancock et al. (2019) and calculate the modulation index at the location of each source to investigate the variability of the sources, thus to understand if the sources exhibit intrinsic variability or if variability is being affected by RISS. We find from table 3.5 (results from Hancock et al. (2019) code on our sources) that all the sources, except SRC213653, are seen to have an observed V_ν parameter lower than the predicted V_{RISS}, suggesting that the variability of the 7 sources is due to RISS and thus not intrinsic. This is consistent with sources studied by Driessen et al. (2022).

We use the radio-optical plot, the light curves, and the RISS values from table 3.5 and find that the 7 sources are in agreement with sources being affected by refractive scintillation of AGN, and thus, we classify sources like SRC207895 as an AGN. Our classification of this source is in agreement with the associated optical source TCDFS J033504.75-274135.9 being an AGN. See Table 3.4 for all classifications of our sources. It is worth noting that information like polarization measurements of these sources could aid in the solidification of our classification, information we currently do not possess. Thus, using the radio-optical plot, light curves, and RISS values is sufficient information to classify the sources, as classified above.

5.3 SRC213653

The new radio transient, SRC213653 is seen to coincide with a low mass proper motion star LP 888-63 that is a companion to a white dwarf binary system. LP 888-63 is within the 2σ positional uncertainty from the radio emission at 0.107 parsec, while the while it is 23 parsec away from the sun. In radio, SRC213643 reaches a peak flux brightness of 1.041 ± 0.043 mJy after which it is seen to decrease and reaches it's lowest radio flux for the next observations before it peaks again and reaches it's second brightness as seen in Figure 4.2. Both the light curve of the source and the radio image cutouts seen in Figure 4.3 are in agreement with each other. We make use of the observed peak radio flux f_v, the distance d to the source in parsec and the observing frequency v in GHz, L the length scale and R_{jup} being the radius of Jupiter to calculate the brightness temperature T_b and thus understand the emission mechanism.

$$T_b = 2 \times 10^9 \left(\frac{f_v}{\mathrm{mJy}}\right) \left(\frac{v}{\mathrm{GHz}}\right)^{-2} \left(\frac{d}{\mathrm{pc}}\right)^2 \left(\frac{L}{R_{\mathrm{jup}}}\right)^{-2} \mathrm{K} \tag{5.1}$$

Following similar approach by Andersson et al. (2022) we use Equation 5.1 to calculate the brightness temperature where we take L the length scale to be 2 stellar radii (in our case we have radius of $\sim 0.317 \pm 0.010\ R_\odot$ (Paegert et al. 2021) to be the estimate size of the M dwarf corana as seen in Benz et al. (1994). This gives a temperature brightness of 4.17×10^{10}K which is below the limit for incoherent emission mechanism of $\sim10^{12}$K meaning the type emission we see could be incoherent or coherent emission. The calculation of the Hα EW places the star in the population of magnetically active stars, this along with the estimated position of the LP 888-63 on the Benz et al. (1994) seen in Figure 4.16 suggest the observed emission is due to gyrosynchrotron emission. It is worth noting that to further help constrain the type of emission observed, application of the methods by (Fijma et al. 2024) on short timescale variability hunt could aid towards understanding the type of emissions. Further information such as polarization could help explain coherent emission, this, however, this is information we do not have.

The optical photometry study of LP 888-63 indicates that the start is a bright red mid M-dwarf. The TESS light curve of LP 888-63 (see Figure 4.4) shows clear optical flares with a relative modulation amplitude of $\sim$ 0.047. We perform a periodogram on the light curve (see Figure 4.4) and find a photometric period of 5.780±0.507 days. In order to see whether the photometric period observed is the rotational period of the star, we compared the calculated tangential velocity with to the rotational velocity from the broadening spectral line. We can estimate $v$sin from the widths of the spectral lines, we do this without accounting for the stars inclination i, we make use of $v\sin(i) = \Delta\lambda c/\lambda = \mathrm{FWHM}_{\mathrm{H}\alpha} c/2\lambda_{\mathrm{H}\alpha}$ just like in Andersson et al. (2022) and find $v\sin \sim 40$ km/s. This is different from the tangential value calculated of ~ 2.77 km/s, this is likely explained by the fact that LP 888-63 is a companion to the White dwarf binary system studied by Nelemans et al. (2005) and thus the discrepancies between the two velocities. If we assume that the photometric period is due to the rotation of the star, this aids towards the magnetic activity of the start as well as the star spots observed to come in and out of view as the star rotates. Looking at the zoomed in Figure of the folded TESS light curve (see Figure 4.4) we find a quasi-sinusoidal behaviour, being in agreement with the flares seen on on Figure 4.4 occurring when the star is brighter.

According to the ASAS-SN light curve in Figure 4.5, there are no clear optical flares clear seen during the ThunderKAT observations of LP 888-6. This is,however, in inconsistency with what we see in the MeerLICHT light curve during the ThunderKAT observations. Clear flares are seen in the u, q and i band and the source being highly active in the u band, as expected since the source has been previously classified as a UV-Ceti flare star (Tamazian et al. 2014). In both the ASAS-SN and MeerLICHT light curves, there are no simultaneous radio-optical flares observations. Though the MeerLICHT telescope was designed and designated to follow in with MeerKAT observations, for this source we unfortunately do not find any flare simultaneity between the two. With the dense and rich coverage of the source from MeerLICHT, we are then able to further study the source in the optically, understanding the colour evolution during flaring and when in quiescent. During flaring, the M-dwarf is seen to to become more blue, changing the colour from when it is in quiescent as seen in Figure 4.8, this is consistent with what would be expected for such systems as also seen in Davenport et al. (2012).

Assuming the star to be a perfect black body emission, we calculate the effective temperature of the flare using the equations Section 4.1 (developed by Sumari Barocci-Faul (Master's thesis in preparation)) and thus the radiating area from the star during flaring. The found effective flare temperature of 7500 K (see Figure 4.10), is $\sim$ 3 times the effective temperature of the M-dwarf when in quiescent, this is also seen in Maas et al. (2022). Modeling the black body for the effective temperature of the star seen in Figure 4.12, allows us to further calculate the bolometric correction for MeerLICHT filters (seen Figure 4.14) and thus find the bolometic magnitude for u, q, and i. From this the luminosity of the flare is found to be $\sim 2.33{\times}10^{30}$ erg s^{-1}. This is consistent with high-energy flares, seen to be on the order of of 10^{30} erg s^{-1} (Tofflemire et al. 2012) and are often associated with more significant magnetic disturbances on the star and accompanied by other forms of electromagnetic radiation, such as X-rays and ultraviolet emission (Tofflemire et al. 2012). When the surface area of the star is compared to the area of the flare, it is revealed that only $\sim$ 0.21 percent of the star is seen be the flaring region. Suggesting that the flare originates from a localized region on the star's surface (Ilin et al. 2022). In Figure 3.11, SRC213653 lies well within the region most stellar sources are found. This is consistent even with the diagonal lines, thus making it trivial to classify the source as a star and this is in line with what the source has already been classified as in literature.

5.4 Conclusion and future work

5.4.1 Conclusion

The goal of this thesis was to firstly validate the usage of SDP images in the commensal search for radio variables and transients and thus further search for these sources in the LADUMA field. Our validation of using SDP images for commensal transient hunt demonstrates a robust number of recovered sources of $\sim$67 percent of sources when compared to OxKAT images. This suggest that relying solely on SDP images for transient detection would result in missing out on $\sim$33 percent of potential candidates. The number of common sources recovered in both OxKAT and SDP images, still supports the effectiveness of SDP images in the commensal search for radio variables and transients. Despite the presence of unmatched sources, most of which are extended and resolved sources rather than point sources in the OxKAT images, the reliability and consistency of SDP data remain evident. This discrepancy is evident in the comparison of flux levels between SDP and OxKAT images, with SDP fluxes consistently lower. The higher detection rate by TraP in OxKAT images may be attributed to reduced noise levels, likely a result of DDE corrections and primary beam correction, which facilitate the identification of fainter sources. This observation is further supported by the prevalence of fainter sources in the lower flux range of OxKAT images compared to SDP images. Thus, while OxKAT images offer advantages in sensitivity, the use of SDP images remains a reliable approach for commensal transient searches.

We made use of 41 SDP images from LADUMA which were observed in the UHF band for the commensal transient searches. Our analysis revealed eight interesting sources, among which a new radio transient coincided with a low mass proper motion star, LP 888-63. Employing TraP with default parameters, we identified a total of 7299 potential transients or variables, subsequently subjecting them to filtering steps based on η_ν and V_ν criteria, were only 290 sources passed. However, it is imperative to acknowledge that this filtering approach may introduce bias towards sources exhibiting from epoch-to-epoch variability, potentially overlooking other interesting sources, as observed in previous studies. We then performed light curve analyses along with multi-wavelength source association. All sources exhibited potential optical and infrared counterparts, with some lacking X-ray counterparts. Using radio fluxes and optical magnitudes, we plotted these sources on an optical-radio plot, revealing their consistency with AGNs and quasars, consistent with previous findings. Furthermore, we employed a model to calculate the modulation index, which we used to conclude that the observed variability in the sources is likely influenced by refractive interstellar scintillation rather than intrinsic variability, consistent with previous literature. Based on the combined analysis of radio-optical plots, light curves, and RISS values, we confidently classified these sources, though the inclusion of polarization measurements could enhance the robustness of these classifications, an aspect we are currently lacking in our study. Thus, our methodology, of using radio-optical plots, light curves, and RISS values, suffices for the classification of these sources.

The new radio transient, SRC213653, reveals its coincidental alignment with the low mass proper motion star LP 888–63, which is part of a white dwarf binary system. The radio emission is observed within a 2σ positional uncertainty, while LP 888-63 is situated 23 parsecs away from the Sun. The radio light curve of SCR213643 shows a peak flux brightness of 1.041 ± 0.043 mJy. We then used the observed peak radio flux, distance to the source, and observing frequency, we estimate the brightness temperature of 4.17×10^{10}K, indicating possible incoherent mechanisms. Additionally, optical photometry of LP 888–63 suggests it to be a bright red mid M-dwarf, showing clear optical flares with a relative modulation amplitude of ~ 0.047 from TESS. The periodogram analysis suggests a photometric period of 5.780 ± 0.507 days, possibly related to the star's rotation, indicating magnetic activity and star spots. The optical and radio light curves show distinct flaring events, with no simultaneous observations from both MeerLICHT and ASAS-SN, suggesting disparate emission mechanisms. Further analysis of optical flares using MeerLICHT reveals blue coloration during flaring, consistent with similar systems. We estimated the effective temperature during flaring of 7500 K with luminosity $\sim 2.33\times10^{30}$ erg s^{-1} of shows significant energy output and localized flare origins. Optical-radio plot positioning confirms SRC213653 as a stellar source, aligning with prior classifications. Overall, our findings shed light on the complex emission processes and magnetic activity of LP 888-63, providing insights into its stellar nature and behaviour. These results contribute to our understanding of stellar activity and emission mechanisms, particularly in binary star systems.

5.4.2 Future work

Building upon the findings presented in this work, the identification and characterisation of radio transients and variables present exciting opportunities for further investigation. Future work could focus on leveraging the SARAO SDP image for real-time transient detections, to enhance our ability to rapidly identify and respond to astronomical events. We propose developing and refining the existing filtering algorithms to improve the detection efficiency of interesting sources while reducing false positives. Expanding multi-wavelength studies to include additional bands beyond optical, radio, X-ray, and infrared, such as gamma-ray observations, for a more comprehensive understanding of the sources. Amongst others, we propose implementing machine learning techniques for automated source classification, facilitating the rapid analysis of large datasets and enabling real-time transient detection thus the usage of SDP images for transient searches will be ideal for this work. We also propose a continued long-term monitoring of SRC213653 radio and optical emissions to capture rare or unusual flaring events and study their impact on the star's atmosphere and surrounding environment, this could also reveal the intended MeerKAT-MeerLICHT coupling for simultaneous observations. We plan to further work on the effective temperature equations to incorporate the associated uncertainties and thus the quoted effective temperature using the MeerLICHT data of SRC213653 remain estimates.

Bibliography

Abbott T. M. C., et al., 2022, VizieR Online Data Catalog, p. II/371

Andersson A., et al., 2022, MNRAS, 513, 3482

Andersson A., et al., 2023, MNRAS, 523, 2219

Angelakis E., et al., 2012, Journal of Physics: Conference Series, 372, 012007

Angelakis E., et al., 2019, A&A, 626, A60

Ballesteros F. J., 2012, EPL (Europhysics Letters), 97, 34008

Benz A. O., et al., 1994, A&A, 285, 621

Bidelman W. P., 1985, ApJS, 59, 197

Bloemen S., et al., 2016, in Hall H. J., Gilmozzi R., Marshall H. K., eds, Vol. 9906, Ground-based and Airborne Telescopes VI. SPIE, p. 990664, doi:10.1117/12.2232522, `https://doi.org/10.1117/12.2232522`

Blyth S., et al., 2016, in MeerKAT Science: On the Pathway to the SKA. p. 4, doi:10.22323/1.277.0004

Bochanski J. J., et al., 2007, AJ, 133, 531

Bochanski J. J., et al., 2010, AJ, 139, 2679

Bonnarel F., et al., 2000, A&AS, 143, 33

Bower G. C., et al., 2018, The Astrophysical Journal Supplement Series, 237, 1

Braun R., et al., 2019, arXiv e-prints, p. arXiv:1912.12699

Bright J. S., et al., 2020, Nature Astronomy, 4, 697

Bruzewski S., et al., 2021, ApJ, 914, 42

Burgasser A. J., et al., 2005, ApJ, 626, 486

CHIME/FRB Collaboration et al., 2018, ApJ, 863, 48

Caleb M., et al., 2022, Nature Astronomy, 6, 828–836

Camilo F., et al., 2018, ApJ, 856, 180

Carroll B. W., Ostlie D. A., 2017, An introduction to modern astrophysics, Second Edition

Chambers K. C., et al., 2016, arXiv e-prints, p. arXiv:1612.05560

Chastain S. I., et al., 2023, Monthly Notices of the Royal Astronomical Society, 526, 1888–1903

Comrie A., et al., 2021, CARTA: The Cube Analysis and Rendering Tool for Astronomy, doi:10.5281/zenodo.4905459

Condon J. J., Ransom S. M., 2016, Essential Radio Astronomy

Condon J. J., et al., 1998, AJ, 115, 1693

Cordes J. M., Chatterjee S., 2019, ARA&A, 57, 417

Cordes J. M., Lazio T. J. W., 2002, arXiv e-prints, pp astro–ph/0207156

Cordes J. M., et al., 2019, Annual Review of Astronomy and Astrophysics, 57, 417

Cram L. E., Mullan D. J., 1979, ApJ, 234, 579

Crosley M. K., Osten R. A., 2018, ApJ, 856, 39

Cutri R. M., et al., 2003, VizieR Online Data Catalog, p. II/246

Cutri R. M., et al., 2012, Explanatory Supplement to the WISE All-Sky Data Release Products, Explanatory Supplement to the WISE All-Sky Data Release Products

Cutri R. M., et al., 2021, VizieR Online Data Catalog, p. II/328

Davenport J. R. A., et al., 2012, ApJ, 748, 58

Drake A. J., et al., 2009, ApJ, 696, 870

Driessen L. N., et al., 2022, MNRAS, 512, 5037

Driessen L. N., et al., 2024, arXiv e-prints, p. arXiv:2404.07418

Dulk G. A., 1985, ARA&A, 23, 169

Fender R. P., Bell M. E., 2011, Bulletin of the Astronomical Society of India, 39, 315

Fender R., et al., 2015, in Advancing Astrophysics with the Square Kilometre Array (AASKA14). p. 51 (`arXiv:1507.00729`), doi:10.22323/1.215.0051

Fender R., et al., 2016, in MeerKAT Science: On the Pathway to the SKA. p. 13 (`arXiv:1711.04132`), doi:10.22323/1.277.0013

Fetherolf T., et al., 2023, ApJS, 268, 4

Fijma S., et al., 2024, MNRAS, 528, 6985

Flewelling H., 2018, in American Astronomical Society Meeting Abstracts #231. p. 436.01

Fomalont E., et al., 1999, Synthesis Imaging in Radio Astronomy II: A Collection of Lectures from the Sixth NRAO/NMIMT Synthesis Imaging Summer School Held at Socorro, New Mexico, USA, 17-23 June, 1998, page 301. Astronomical Society of the Pacific conference series, Astronomical Society of the Pacific, `https://books.google.co.za/books?id=e23vAAAAMAAJ`

Freund S., et al., 2018, A&A, 614, A125

Gaia Collaboration et al., 2020, VizieR Online Data Catalog, p. I/350

Gaia Collaboration et al., 2021, A&A, 650, C3

Gershberg R. E., et al., 1999, Acta Astronomica, 139, 555

Gizis J. E., et al., 2017, ApJ, 845, 33

Gourdji K., et al., 2022, MNRAS, 509, 5018

Hale C. L., et al., 2021, , 38, e058

Hallinan G., et al., 2007, ApJ, 663, L25

Hancock P. J., et al., 2019, arXiv e-prints, p. arXiv:1907.08395

Hawley S. L., et al., 2003, ApJ, 597, 535

Healy J., et al., 2021, A&A, 654, A173

Henry T. J., et al., 2006, AJ, 132, 2360

Heywood I., 2020, oxkat: Semi-automated imaging of MeerKAT observations, Astrophysics Source Code Library, record ascl:2009.003

Hurley-Walker N., et al., 2022, Nature, 601, 526

Ilin E., et al., 2022, Astronomische Nachrichten, 343, e10111

Irwin J. A., 2021, Astrophysics - Decoding the Cosmos, Second Edition

Ivezić Ž., et al., 2014, Statistics, Data Mining, and Machine Learning in Astronomy: A Practical Python Guide for the Analysis of Survey Data, doi:10.1515/9781400848911.

Jankowski F., et al., 2022, in Ruiz J. E., Pierfedereci F., Teuben P., eds, Astronomical Society of the Pacific Conference Series Vol. 532, Astronomical Society of the Pacific Conference Series. p. 273 (`arXiv:2012.05173`), doi:10.48550/arXiv.2012.05173

Jonas J. L., et al., 2016, Proceedings of the International Astronomical Union, 11, 3

Kenyon J. S., Smirnov O. M., 2018, Monthly Notices of the Royal Astronomical Society, 479, 5167

Kochanek C. S., et al., 2017, PASP, 129, 104502

Kowalski A. F., et al., 2010, ApJ, 714, L98

Kowalski A. F., et al., 2015, Sol. Phys., 290, 3487

Lacy M., et al., 2020, Publications of the Astronomical Society of the Pacific, 132, 035001

Lomb N. R., 1976, Ap&SS, 39, 447

Longair M. S., 2011, High Energy Astrophysics

Lorimer D. R., et al., 2012, Handbook of Pulsar Astronomy

Luyten W. J., 1979a, LHS catalogue. A catalogue of stars with proper motions exceeding 0"5 annually

Luyten W. J., 1979b, NLTT catalogue. Volume_I. +90__to_+30_. Volume._II. +30__to_0_.

MAGIC Collaboration et al., 2019, Nature, 575, 459

Maas A. J., et al., 2022, A&A, 668, A111

Macquart J. P., et al., 2020, Nature, 581, 391

Mauch T., et al., 2020a, ApJ

Mauch T., et al., 2020b, ApJ, 888, 61

McMullin J. P., Waters B., Schiebel D., Young W., 2007, Astronomy & Astrophysics, 491

Melrose D. B., 1980, Plasma astrohysics. Nonthermal processes in diffuse magnetized plasmas - Vol.1: The emission, absorption and transfer of waves in plasmas; Vol.2: Astrophysical applications

Melrose D. B., 1992, Philosophical Transactions of the Royal Society of London Series A, 341, 105

Melrose D. B., 2017, Reviews of Modern Plasma Physics, 1, 5

Mohan N., Rafferty D., 2015, Astrophysics Source Code Library,

Mooley K. P., et al., 2016, ApJ, 818, 105

Nelemans G., et al., 2005, A&A, 440, 1087

Newton E. R., et al., 2017, ApJ, 834, 85

Nindos A., 2020, Frontiers in Astronomy and Space Sciences, 7, 57

Norris R. P., et al., 2006, AJ, 132, 2409

Ochsenbein F., et al., 2000, A&AS, 143, 23

Offringa A. R., et al., 2014, Astronomy & Astrophysics, 554, A23

Paegert M., et al., 2021, arXiv e-prints, p. arXiv:2108.04778

Petroff E., Hessels J., Lorimer D., 2019, Astronomy and Astrophysics Review, 27, 4

Pietka M., et al., 2015a, MNRAS, 446, 3687

Pietka M., et al., 2015b, Monthly Notices of the Royal Astronomical Society, 446, 3687

Rajpurohit A. S., et al., 2013, A&A, 556, A15

Reid I. N., et al., 2002, The Astronomical Journal, 124, 2721

Rhodes L., et al., 2020, MNRAS, 496, 3326

Ricker G. R., et al., 2015, Journal of Astronomical Telescopes, Instruments, and Systems, 1, 014003

Rickett B. J., 1990, ARA&A, 28, 561

Rowlinson A., et al., 2019, Astronomy and Computing, 27, 111

Rowlinson A., et al., 2022, MNRAS, 517, 2894

Rybicki G. B., Lightman A. P., 1986, Radiative Processes in Astrophysics

Salvato M., et al., 2018, MNRAS, 473, 4937

Scargle J. D., 1982, ApJ, 263, 835

Schneider A. C., et al., 2016, ApJ, 817, 112

Schneider A. C., et al., 2019, AJ, 157, 234

Serra P., et al., 2016, in MeerKAT Science: On the Pathway to the SKA. p. 8 (`arXiv:1709.01289`), doi:10.22323/1.277.0008

Starling R. L. C., et al., 2020, MNRAS, 494, 5787

Stassun K. G., et al., 2019, AJ, 158, 138

Stewart A. J., et al., 2018, MNRAS, 479, 2481

Swart G. P., et al., 2020, in Angeli G. Z., Dierickx P., eds, Society of Photo-Optical Instrumentation Engineers (SPIE) Conference Series Vol. 11450, Modeling, Systems Engineering, and Project Management for Astronomy IX. p. 114502T, doi:10.1117/12.2563278

Swinbank J. D., et al., 2015, Astronomy & Astrophysics, 567, A41

Tamazian V. S., et al., 2014, Acta Astronomica, 64, 359

Tan J., et al., 2020, in Kong L., Huang T., Zhu Y., Yu S., eds, , Big Data in Astronomy: Scientific Data Processing for Advanced Radio Telescopes. pp 3–28, doi:10.1016/B978-0-12-819084-5.00014-6

Tasse C., et al., 2018, A&A, 611, A87

Thompson A. R., et al., 1980, ApJS, 44, 151

Thompson A. R., et al., 2017, Interferometry and Synthesis in Radio Astronomy, 3rd Edition, doi:10.1007/978-3-319-44431-4.

Thyagarajan N., et al., 2011, ApJ, 742, 49

Tie S. S., et al., 2017, AJ, 153, 107

Tofflemire B. M., et al., 2012, AJ, 143, 12

Treumann R. A., 2006, A&A Rev., 13, 229

Trifonov T., et al., 2018, A&A, 609, A117

VanderPlas J. T., 2018, ApJS, 236, 16

Vreeswijk P., et al., 2021, BlackBOX: BlackGEM and MeerLICHT image reduction software, Astrophysics Source Code Library, record ascl:2105.011

Walker M. A., 1998, MNRAS, 294, 307

Webb N. A., et al., 2020, A&A, 641, A136

Wenger M., et al., 2000, A&AS, 143, 9

West A. A., et al., 2005, arXiv e-prints, pp astro–ph/0504673

West A. A., et al., 2008, AJ, 135, 785

White S. M., et al., 2024, arXiv e-prints, p. arXiv:2405.01755

Willes A. J., et al., 2004, MNRAS, 348, 285

Xue M., et al., 2019, Publications of the Astronomical Society of Australia, 36, e025

de Blok W. J. G., et al., 2016, in MeerKAT Science: On the Pathway to the SKA. p. 7 (`arXiv:1709.08458`), doi:10.22323/1.277.0007

de Ruiter I., et al., 2021, MNRAS, 508, 2412

van den Eijnden J., et al., 2020, The Astronomer's Telegram, 13716, 1

van den Eijnden J., et al., 2022, MNRAS, 516, 2641

Appendix A

Additional Plots

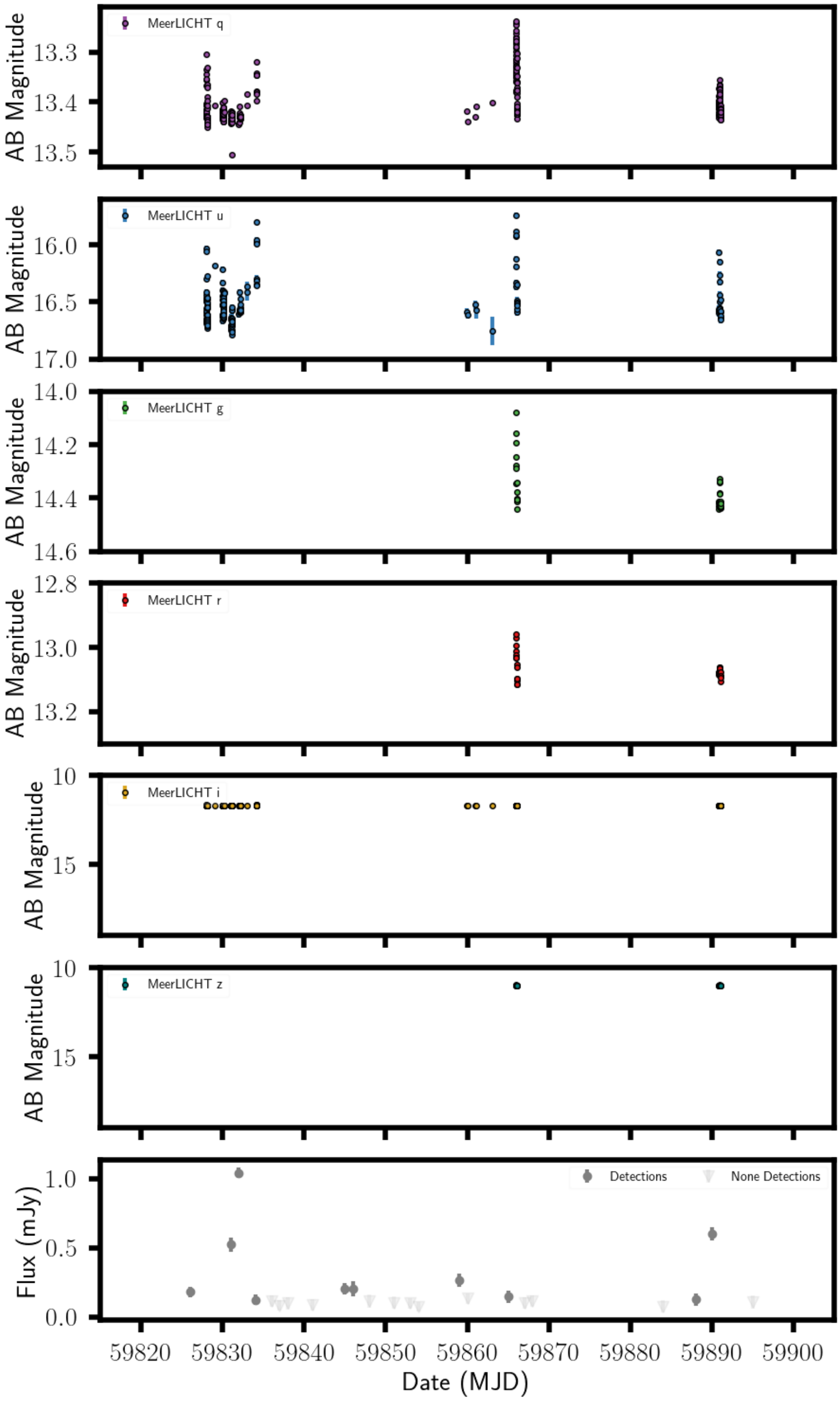

Figure A.1: MeerKAT and MeerLICHT light curve during the ThunderKAT observation

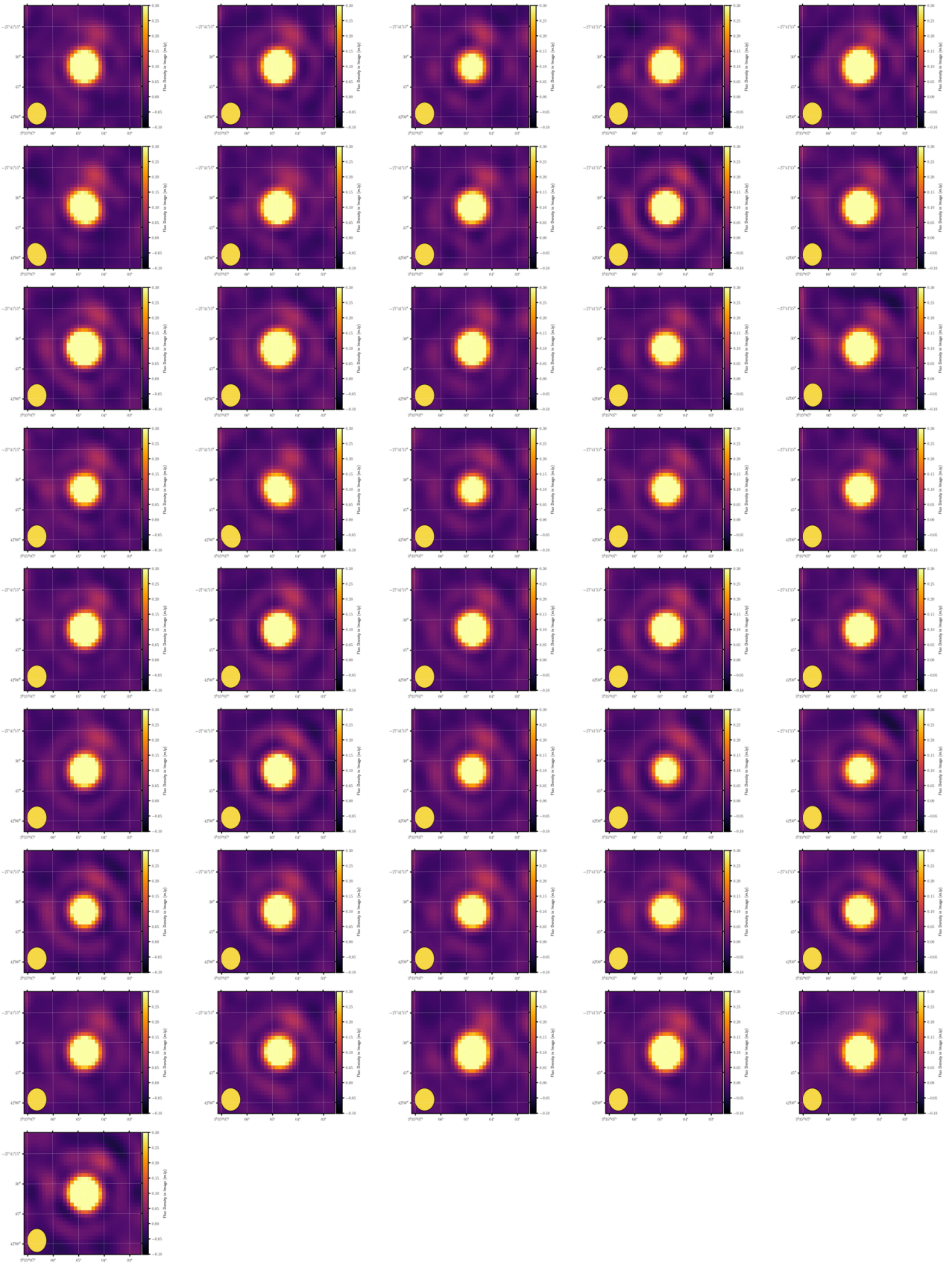

Figure A.2: The radio image cut-out of SCR207895 from the 41 ThunderKAT observations The images are plotted chronologically from the top left to the right. In all the images the synthesised beam is found on the bottom left corner of each image. All the images are scaled to the same flux density range of (0.1 - 0.3) mJy on a linear scale. The source can be seen varying in flux from epoch to epoch.

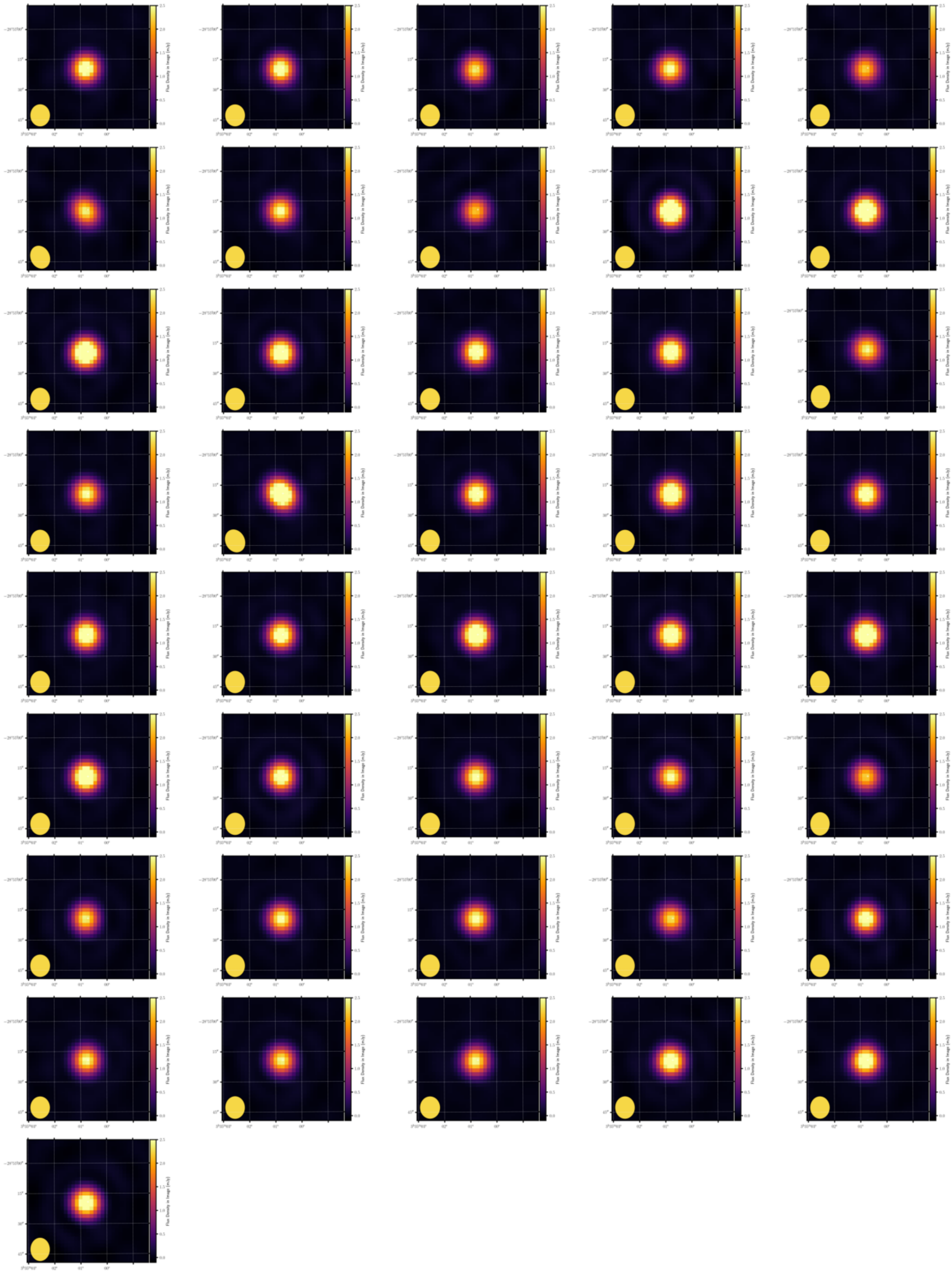

Figure A.3: The radio image cut-out of SCR 209750 from the 41 ThunderKAT observations The images are plotted chronologically from the top left to the right. In all the images the synthesised beam is found on the bottom left corner of each image. All the images are scaled to the same flux density range of (0.0 - 2.5) mJy on a linear scale. The source can be seen varying in flux from epoch to epoch.

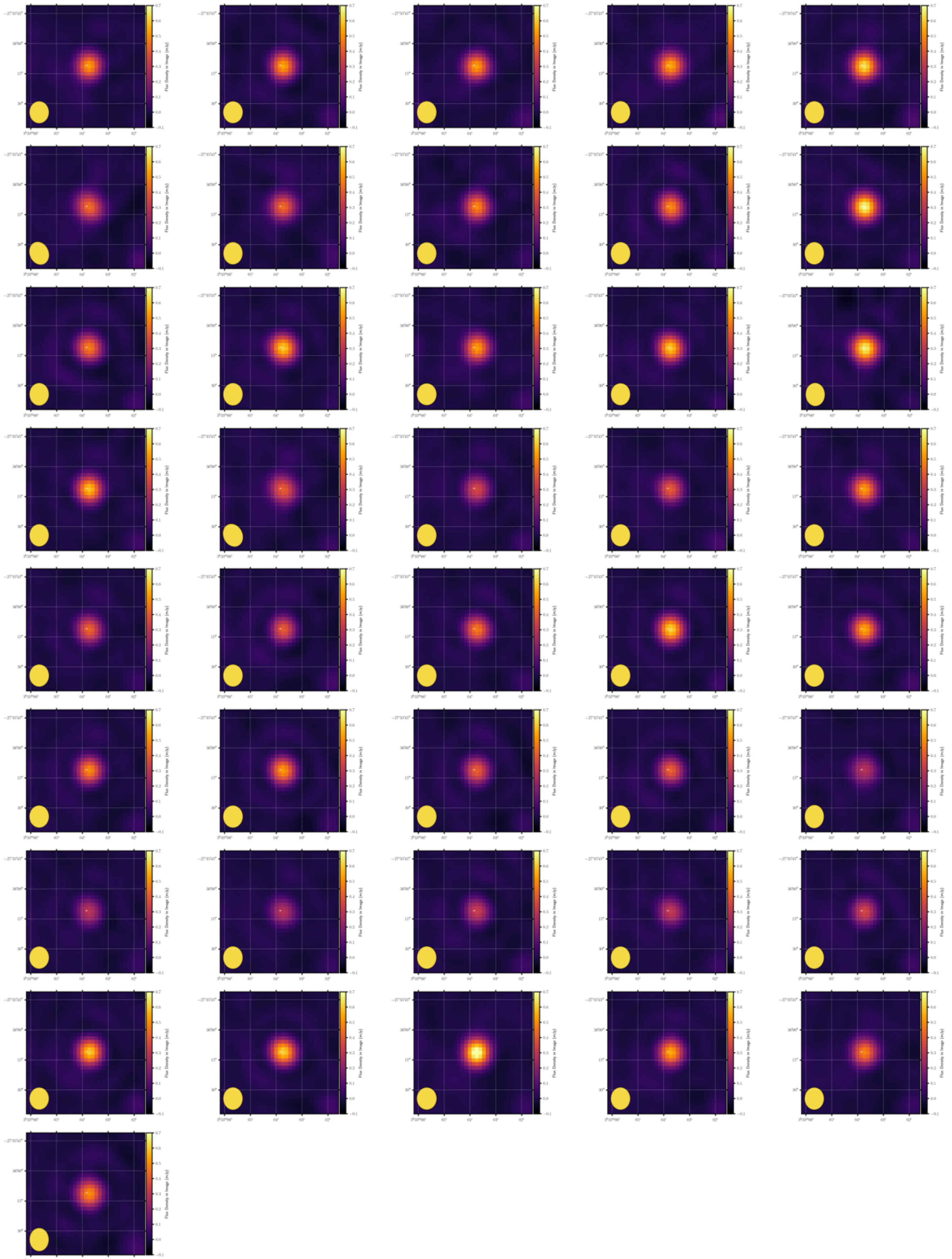

Figure A.4: The radio image cut-out of SCR 209337 from the 41 ThunderKAT observations The images are plotted chronologically from the top left to the right. In all the images the synthesised beam is found on the bottom left corner of each image. All the images are scaled to the same flux density range of (0.0 - 0.7) mJy on a linear scale. The source can be seen varying in flux from epoch to epoch.

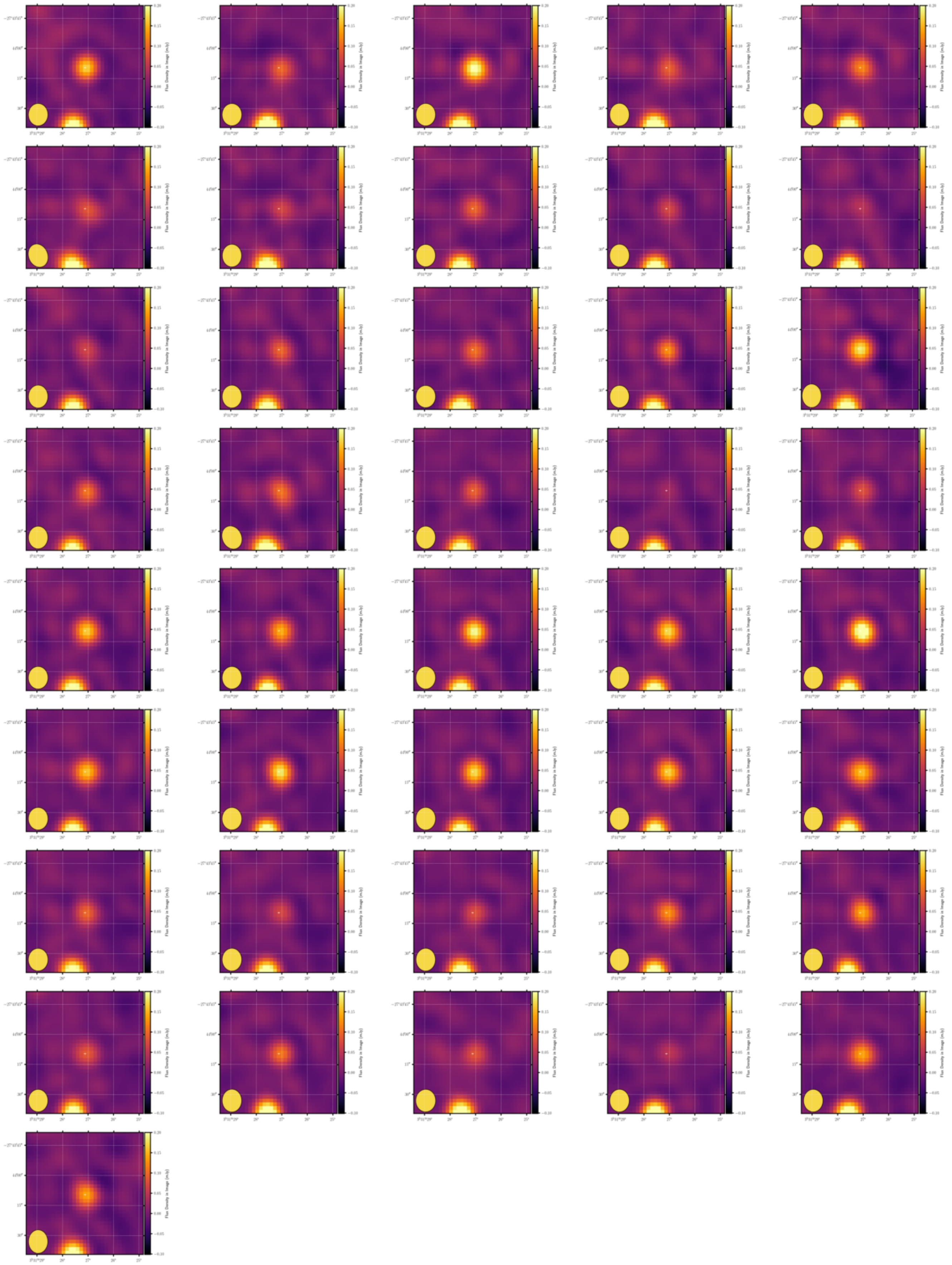

Figure A.5: The radio image cut-out of SCR 210499 from the 41 ThunderKAT observations The images are plotted chronologically from the top left to the right. In all the images the synthesised beam is found on the bottom left corner of each image. All the images are scaled to the same flux density range of (0.1 - 0.2) mJy on a linear scale. The source can be seen varying in flux from epoch to epoch.

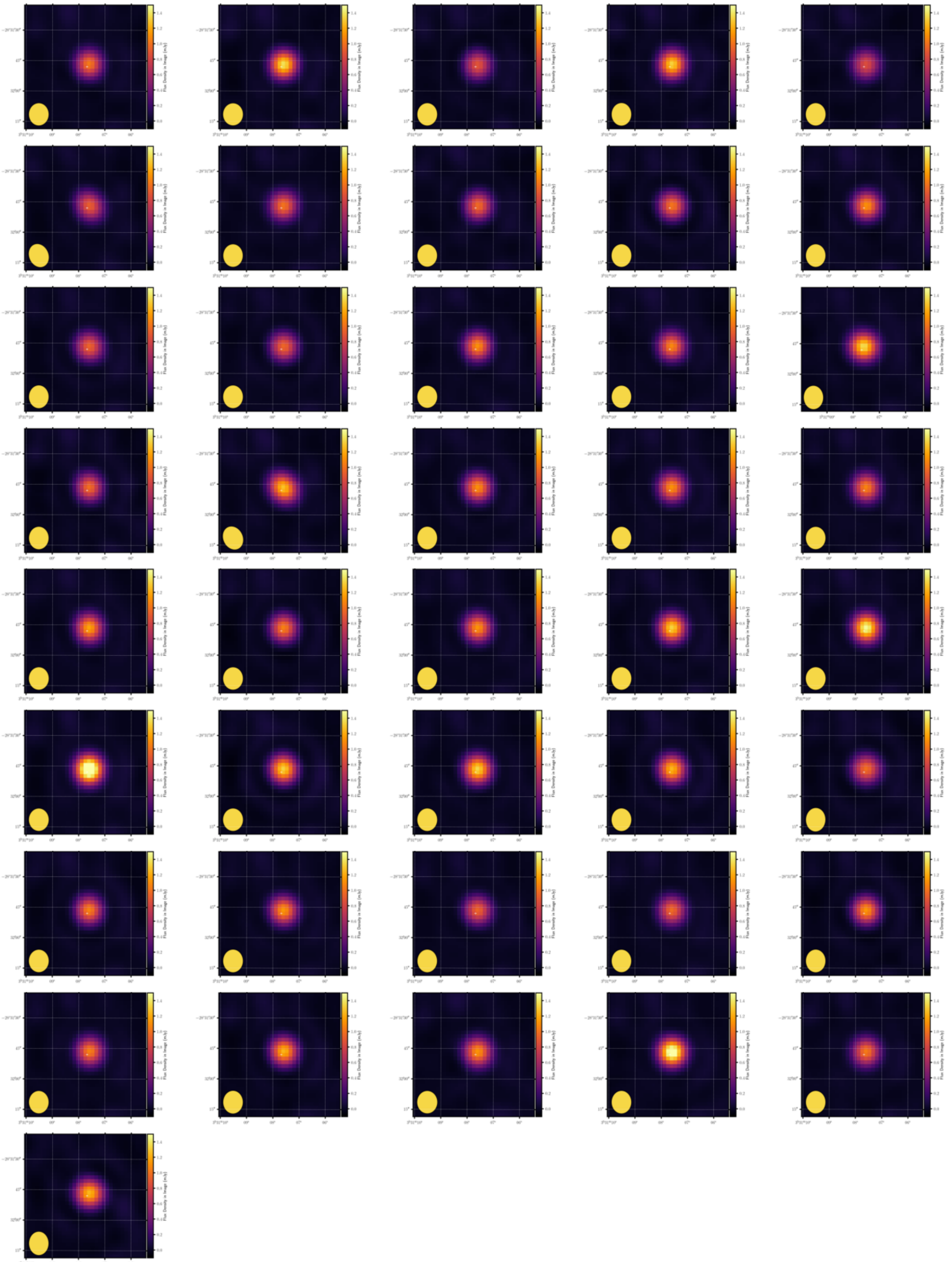

Figure A.6: The radio image cut-out of SCR 210683 from the 41 ThunderKAT observations The images are plotted chronologically from the top left to the right. In all the images the synthesised beam is found on the bottom left corner of each image. All the images are scaled to the same flux density range of (0.0 - 1.4) mJy on a linear scale. The source can be seen varying in flux from epoch to epoch.

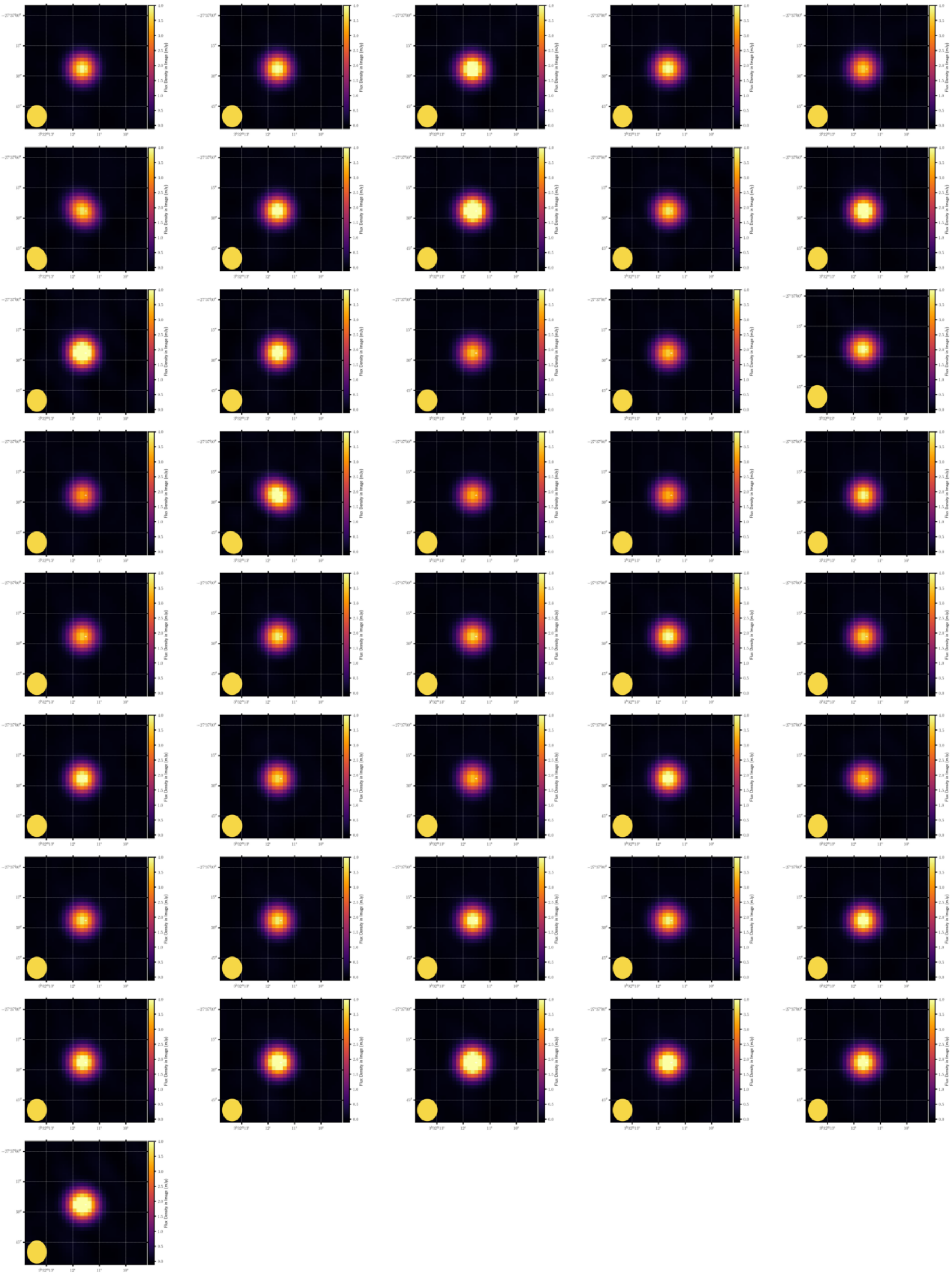

Figure A.7: The radio image cut-out of SCR 209991 from the 41 ThunderKAT observations The images are plotted chronologically from the top left to the right. In all the images the synthesised beam is found on the bottom left corner of each image. All the images are scaled to the same flux density range of (0.0 - 4) mJy on a linear scale. The source can be seen varying in flux from epoch to epoch.

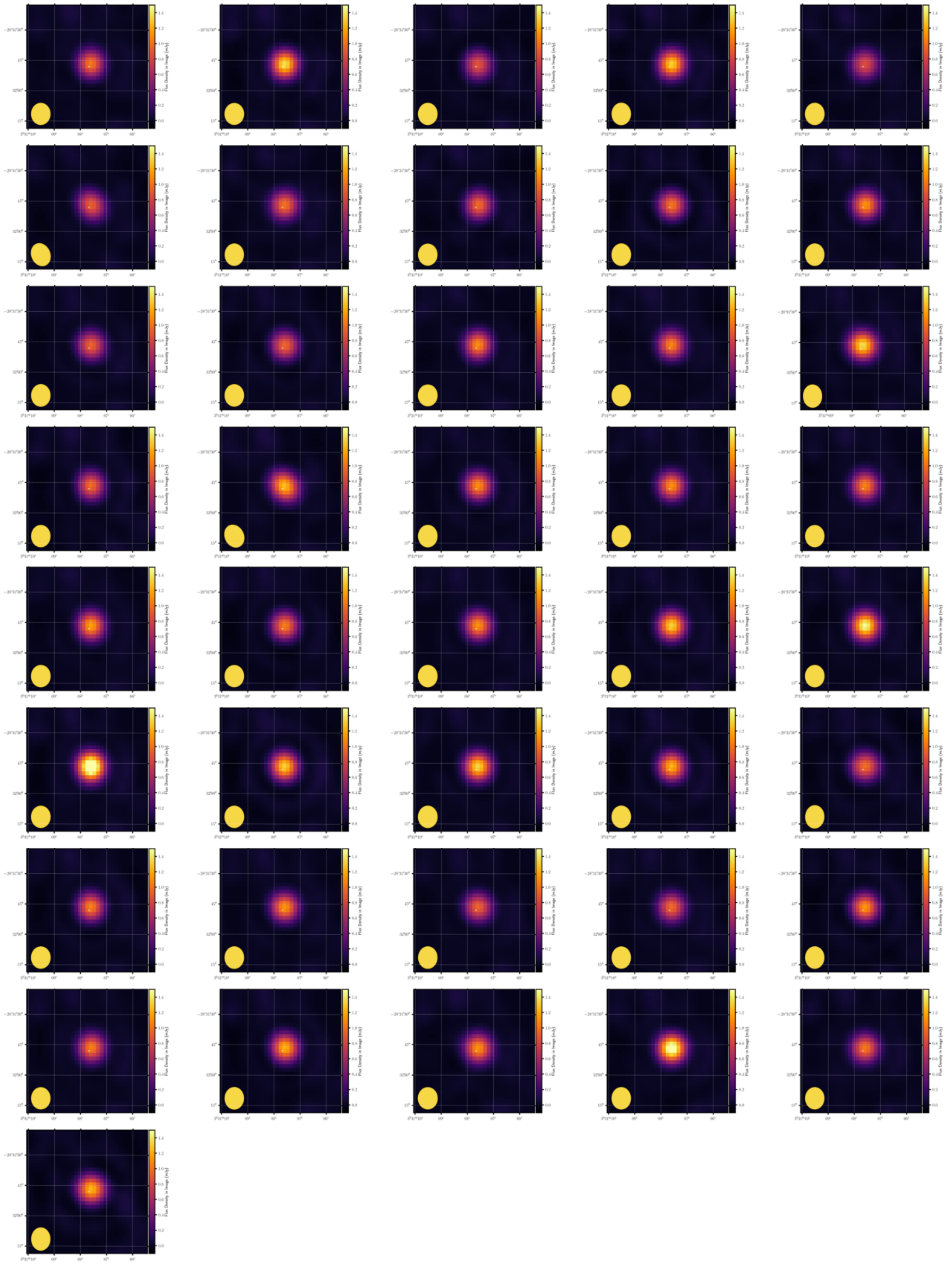

Figure A.8: The radio image cut-out of SCR 211766 from the 41 ThunderKAT observations The images are plotted chronologically from the top left to the right. In all the images the synthesised beam is found on the bottom left corner of each image. All the images are scaled to the same flux density range of (0.0 - 1.4) mJy on a linear scale. The source can be seen varying in flux from epoch to epoch.